Modelling Large Membrane-Like Structures in the Ocean Environment

An Application of Isogeometric Analysis on Fluid-Structure Interaction

H.M. Verhelst

TU Delft

Modelling Large Membrane-Like Structures in the Ocean Environment

An Application of Isogeometric Analysis on Fluid-Structure Interaction

Hugo Verhelst

H.M.Verhelst@student.tudelft.nl

Master Student Applied Mathematics
Master Student Marine Technology

February 5, 2019

Supervisors:
Prof. Dr. Ir. M.L. Kaminski
Dr. Ir. F.J. Vermolen
Dr. M. Möller
Dr. Ir. J.H. den Besten

Image from https://commons.wikimedia.org/wiki/File:Backlit_green_poinsettia_leaf.jpg

Contents

1 | Introduction

The attention for climate change has increased over the past decenium. As a consequence, worldwide political debate more and more changes towards renewable energies, letting the fossil fuels behind. The Paris agreement [2] - ratified by 180 states and signed by 197 states - states that the increase in global average temperature should be below 2°C above pre-industrial levels and persuading efforts to limit the increase to 1.5°C above pre-industrial levels. As a result, the submitted of the contribution of the European Union to the agreement states that the Greenhouse Gas (GHG) emissions should be cutted by 40% in 2030 and with long-term goal 80-95% before 2050, all compared to the year 1990 [3].

This work is a contribution to the development of an offshore solar energy platform. Before going into details on the specific goals and the outline of the thesis, which are given in section 1.3 and section 1.4, respectively, an introduction to offshore energy solutions is given in section 1.1. Although this thesis is not a motivation for offshore solar energy, the following section illustrates a *quick and dirty* line of reasoning for offshore solar energy as an alternative to offshore wind and wave energy.

1.1 Offshore Solar Energy: A Motivation

In the run for cleaner energies, Western European countries such as Germany, Denmark and the Netherlands massively increased their offshore wind-energy production up 88% of the total installed capacity in 2016 (14,384 MW) offshore. These wind turbines are all located in shallow waters with depths around 20m [4, 5]. For water increasing water depths ($> 50m$[1]), floating wind turbines form an alternatieve for large support structures of bottom-founded turbines. However, floating turbines are less developed compared to the bottom-founded wind turbines and future work needs to be done on mooring system design and testing [6].

An alternative to floating wind turbines is wave energy. The principle of wave energy basically is to extract the energy that is contained in a sea wave and transform it to electrical energy. Compared to wind energy, wave energy has the advantage that the energy production is constant over time as waves are usually more constant than wind speeds. Most wave energy converters discussed in literature operate in shallow waters [7, 8] but the potential in deep waters (i.e. along the Scandinavian coast [9] or the Brazilian coast [10]) allows for wave farms in the order of hundreds of megawatts up to tenths of gigawatts. Kalogeri et al.[11] investigates a combined wind and wave energy farm which is optimised for a constant energy output from these two variable energy resources. This work is a great example for multi-space utilisation of offshore space which improves constant power output. Furthermore, Kalogeri et al. shows that along the coast of North-Western Europe, the potential for wind and/or wave energy is the highest (see figure 1.1) and that mainly the wave energy potential decreases for waters where the fetch length is low (i.e. the Medditeranean area). For further details to their study, the reader is directed to their work [11]

Another offshore energy resource, which is also used onshore, is solar energy. Like wave energy and

[1] Gao et al.[6] mention that it is not very clear at which depth floating turbines are more cost-effective than bottom-founded wind turbines.

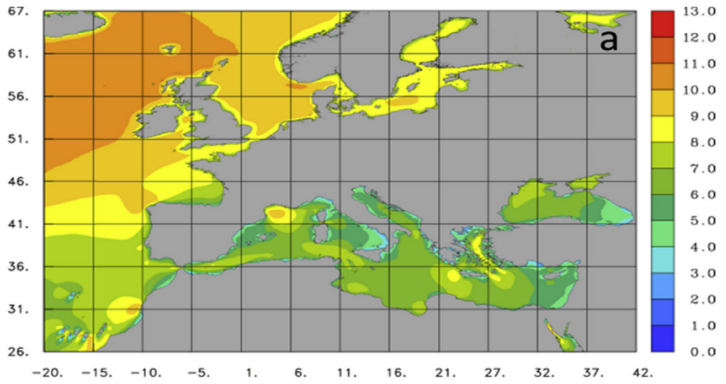

(a) Wind energy

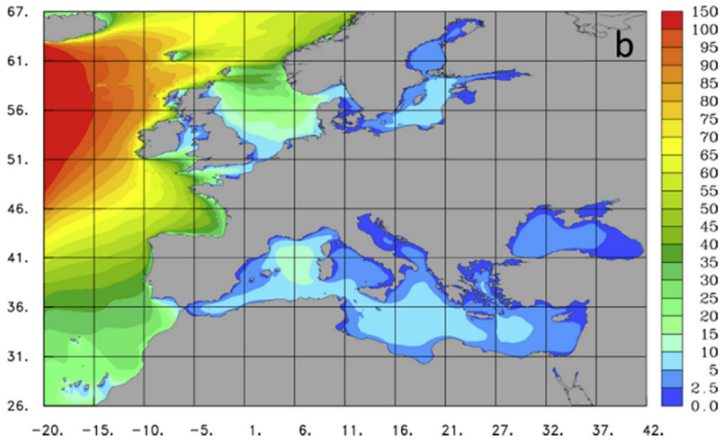

(b) Wave energy

Figure 1.1: Spatial distribution of mean wind and wave energy potential (W/m^2) along the European coast. Adopted from [11]

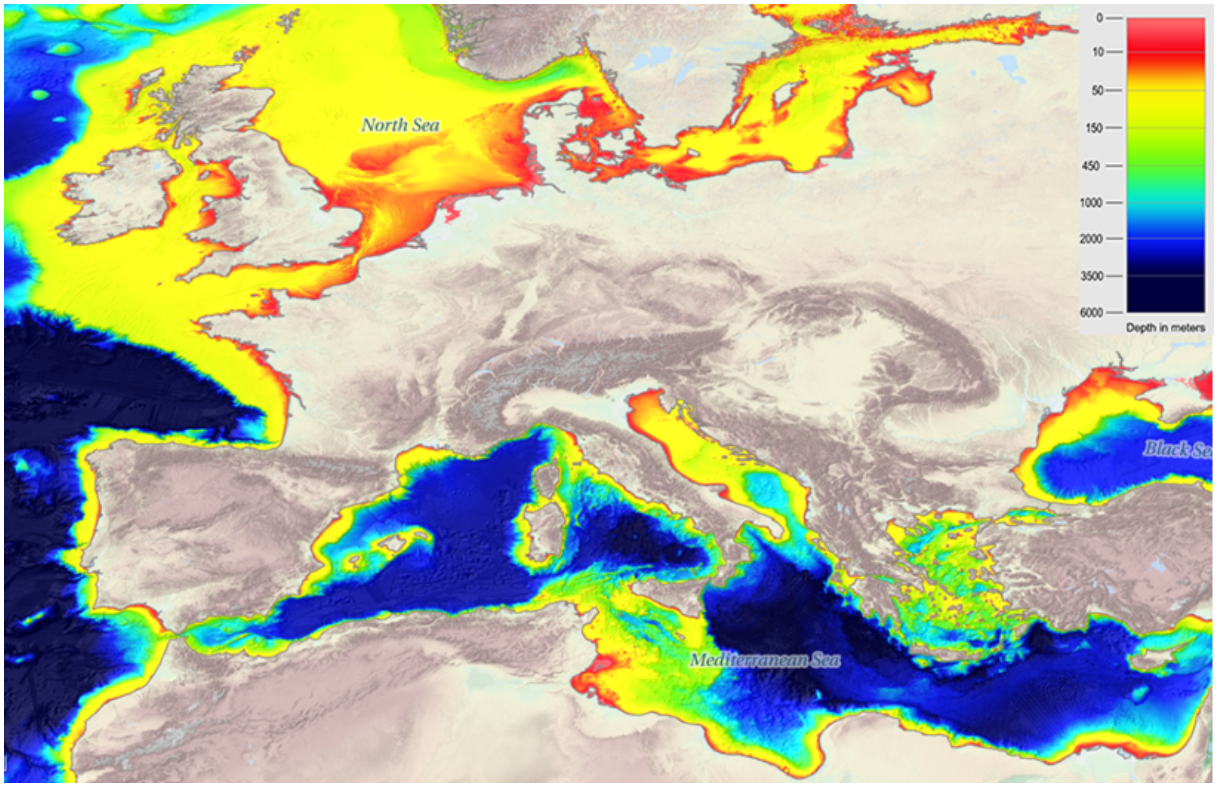

Figure 1.2: Bathymetry of the European seas. Constructed from [15].

contrary to offshore wind energy, offshore solar energy is principally depth-independent as the structure does not change. This makes both applicability in deep water or combined with bottom-founded wind turbines possible. Furthermore, floating PV have the advantage that the panels are cooled by the sea water, achieving good efficiencies of the panels [12, 13]. However, the motions and possible deformation of the offshore solar platform require flexible solar panels or hinged modules and advanced tracking systems. Furthermore, the salinity of the harsh ocean environment might also be an issue and needs to be further investigated [14].

Figure 1.2 presents the bathymetry, i.e. the sea water depths over Europe, based on the bathymetry database EMODnet[2] [15]. The figures from Meerkötter et al. [16] (see figure 1.3) provide insights in cloud cover and the findings from Miglietta et al.[17] show that solar radiation is mainly latitude but also on longitude. Based on data of bathymetry, solar radiation, cloudcover and the wind and wave data of Kalogeri et al.[11] amongst others, potential areas for utilisation of offshore solar energy converters can be identified in a similar way. It is clearly seen that the North-Western part of the Mediterranean sea has a low wind and wave energy potential, but that the solar energy potential at sea might be relatively high. One drawback in this region, however, is that the bathymetry is relatively high and hence mooring concepts for floating solar platforms can be rather complex.

! TO DO: [?]

[2] http://www.emodnet-bathymetry.eu/

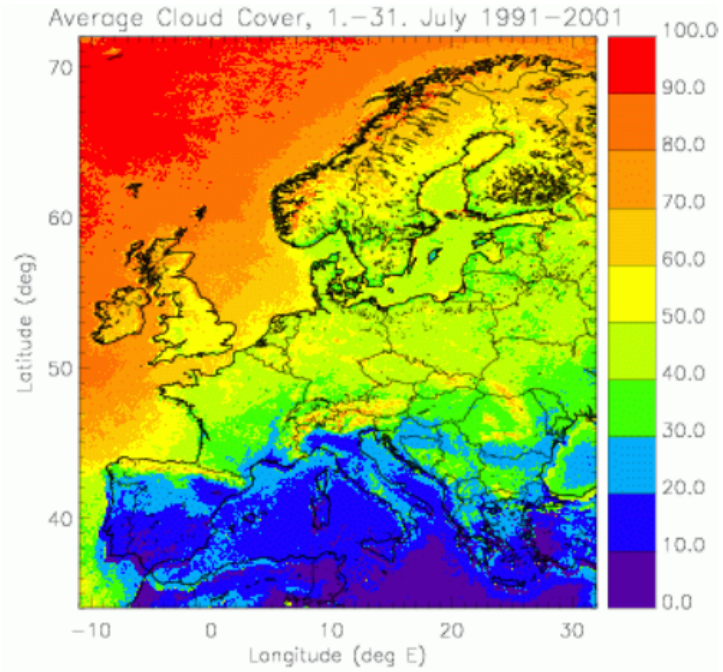

Figure 1.3: Average cloud cover over Europe in the month July between 1991 and 2001. Adopted from Meerkötter et al.[16], which can be consulted for similar figures for other months.

1.2 Platform Characteristics

Platforms for offshore solar energy generation are intended to carry PV panels, either implemented in the floater or installed on top, and the required electronic infrastructure to transfer the generated power from the PV system to the grid or a fuel production unit near the platform. Furthermore, the platform has to resist oceanic loads while maintaining its position. Hence, environmental in-plane loads due to wind, waves and current need to be transferred from the surface area of the platform to the mooring point. Additionally, out-plane loads due to waves need to be resisted by platform deformations without permanent damage.

Without giving full detailed specifications for the platform, the working characteristics of the platform that are adopted including their motivation are listed below:

Circular & Large scale To generate a future-proof framework for analysis of such structures, it is assumed that the structure that is considered is very large, i.e. surface area is of order $\mathcal{O}\left(km^2\right)$). The platforms considered by Kashiwagi[18] amongst others, are of similar size and are referred to as Very Large Floating Structures (VLFSs).
With this assumption, it is reasonable that current and wind speeds are non-uniform and have different direction over the whole platform. Furthermore, it is assumed that the in-plane characteristic length of the platform is larger than the wave lengths exciting the platform. The geometry of the platform is considered to be circular, but analyses can be performed for other geometries without loss of generality.

Continuum As concept designs are not yet available, it is assumed that the platform is a continuum. In other words, the platform does not consist of modules, but rather can be seen as a *continuous structure* without hinges. This assumption is made since hinge forces are expected to be large [3].

[3] Waals presented hinge loads of the concept of the H2020 project SPACE@SEA in March 2018 at MARIN's "The Floating Future Seminar". For their platform with interconnected triangles of sides with dimension 100m, hinge loads of 20,000t

Low Payload: Lightweight Structure The main task of the platform is to carry the PV modules. Hence the payload of the platform is several kilograms per square metre (mg/m^2). Hence, the payload of the platform is characterised to be low compared to other offshore structures. This allows for relatively light-weight structure to carry the panels.

Flexible The lightweight structure should be able to resist large wave heights. If the structure is stiff, its thickness-dimension is rather large in comparison to its payload. This is contradictory to the lightweight structure. Furthermore, the size of the structure causes large internal bending moments, as large wave heights need to be resisted without introducing pitch motions. Alternatively, the structure can be made flexible. In this way, the structure deforms with the waves and is considered to be *wetted* even in large wave heights. Consequently, the bending stiffness of the structure is very low, and the structure behaves as a membrane.

1.3 Thesis Goal

`Parts of this section are to be updated according to the final work.`

In this work, the first steps towards a structural model incorporating fluid-structure interaction of the platform in oceanic conditions are made. To this extend, the Isogeometric Finite Element Method, often referred to as Isogeometric Analysis, is utilised. Emphasis will be on the structural model, rather than the fluid model. The latter will be adopted from XXX. The goal of this thesis is:

> *Develop and implement a 2D Fluid-Structure Interaction framework using Isogeometric Analysis for application for offshore membrane structures, with emphasis on the structural response.*

As full modelling of the floating membrane structure is a big step, all computational aspects for the development of the FSI model for offshore solar membranes are developed and combined in a case study (`to be defined. Probably flutter`). The main difference between the case study and the offshore floating membrane is that the case study does not contain an interface between water and air, whereas the offshore membrane does. In **??**, this will be discussed into more detail.

Moreover, in order to achieve the goal of this thesis a number of sub goals are defined. They are described in the following:

1. *Identify governing equations for both fluid and structure and motivate assumptions.* To facilitate a background for the reader and to clarify limits of certain models, the governing equations for the fluid and structural behaviour will be derived. Furthermore, simplifications on these equations based on the applications and the computational costs will be motivated.

2. *Motivate a coupling strategy for the Fluid-Structure Interaction coupling to be included in the model.* Based on application of a Fluid-Structure Interaction model, different modelling strategies can be adopted. These include monolithic/partitioned system solving and mesh deformation strategies.

3. *Discuss the use of Isogeometric Analysis and apply it in the model problem.* Isogeometric Analysis is a method that is similar to the Finite Element Method to solve Partial Differential Equations (PDEs). This method, its applications and its (dis)advantages compared to the FEM are of importance to the justification of the final model.

4. *Verify and validate (parts of) the model using benchmark cases and discuss improvements of (parts of) the model.* Modelling of the phenomena of fluid structure is a challenge on it self. However, validation and verification of intermediate model steps/components is the core of justification of the final model results.

5. *Give recommendations for modelling of membrane-like structures in the ocean environment, taking into account extreme cases as well as fatigue life predictions.* The final goal of this study is to work

were measured in waves with $H_s = 15.5m$. [19]

towards a model for the response of a membrane-like offshore structure. Hence, the last but not the least deliverable of this study should be recommendations for further steps in the development of the model.

1.4 Outline

`to be updated`

The report is structured as follows:

Literature review The literature review is in chapter 2

Methods The methods of the modelling process are covered in 4–**??**.

Model problem The model problem that is solved using the methods is described in **??**

Results and Discussion The results and discussion of the modelled problem are described in section 5.3

Conclusions and Recommendations Lastly, conclusions and recommendations are given in **??**–**??**

Appendices

```
Additions:
- Proofs about coercivity, well-posedness etc. (see book Scientific Computing)
```

2 | Literature Review

In this chapter, a literature review is presented for topics relating to the present research. Firstly, a brief literature review on past research on Very Large Floating Structures (VLFSs) is presented to identify the state-of-the-art of previously used analysis methods for such structures. Secondly, the phenomena of wrinkling and folding of membranes on substrates or fluid-beds is investigated. The mechanism of wrinkling and folding is presented and state-of-the-art experimental results as well as analysis methods are investigated. Thereafter, two sections will go into more detail on numerical analysis. Firstly, the state-of-the-art of Isogeometric Analysis is presented, covering works from 2005 up to 2019. This section discusses the general philosophy behind IGA, but also topics like meshing techniques and a comparison between IGA and Finite Element Analaysis (FEA). The basics of IGA including examples are discussed in chapter 4. In the last section of this literature review (section 2.4), the topic of Fluid-Structure Interaction (FSI) is covered. This section shows the wide range of applications of different FSI frameworks and their similarities to the present study.

2.1 Previous Work on the Response of Very Large Floating Structures (VLFSs)

Very Large Floating Structures (VLFSs) have been studied in the early 2000s by Kashiwagi for investigation of near-shore floating airport in Japan. Kashiwagi [20] summarizes research on VLFSs which has been done just before 2000. This also includes Kashiwagi [21], where modal-expansion is used and where the pressure integral is calculated using a Galerkin approach with B-splines. Furthermore Kashiwagi [22] modelled an airplane landing on a membrane-like structure on the ocean surface with the modal-expansion method. In all research performed by Kashiwagi, however, thin plate structural vibration equations are used and hence the presence of non-linear structural effects is neglected.

Thereafter, [23] developed an analytical model for the response of VLFSs in waves. In this PhD thesis, an extensive summary of existing VLFS projects is given. Additionally, one can consult [24] for a more recent review of different concepts of VLFSs. Furthermore, Andrianov gives an overview of the assumptions that are made in the analysis of VLFSs. They are:

- VLFSs are modelled as thin, elastic (isotropic/orthotropic) plates with free edges,
- Potential flow is used as fluid model,
- The amplitude of the incident wave and the motions of the VLFS are small. Furthermore, the motions of the VLFS are considered in vertical direction only,
- There is no gap between the VLFS and the water surface, i.e. air entrapment effects are not considered,
- Bathymetry effects are not considered, i.e. the sea bottom is assumed to be flat.

Using these assumptions, an analytical model for the hydroelasticity of VLFSs was developed and applied for different shapes of the VLFS. Recommendations following from this study include modelling of the

structure in large waves, modelling the structure with a non-flat hull and modelling of the response for different mooring solutions. The response of the VLFS for non-constant bathymetry was studied by [25]

Wang and Tay [26] developed a Finite Element - Boundary Element (FE-BE) method for the structural and hydrodynamical model. An uncoupled approach was used where the plate deflection is computed using a modal expansion and thereafter applied on the domain of the fluid. Thereafter, the fluid potential is calculated and pressures were applied on the plate to calculate its deflection. Recommendations by the authors follow from limitations of the model, and include non-linear analysis of the response of the VLFS due to non-linear wave impact and analysis using a Navier-Stokes fluid model.

Wei et al.[27] investigate the hydroelastic response of a VLFS in inhomogeneous waves using a time-domain approach, contrary to the approach by [26] for instance. Their conclusion is that the response in irregular waves significantly differs from the response in homogeneous waves and even severe homogeneous waves cannot be used for design of VLFSs. Their recommendations are therefore to investigate the response with non-free boundary conditions, mooring systems and non-linear wave fields.

In [28, 29] VLFSs with a hinge connection are considered. In both case, a hydroelastic model assuming small elastic deformations of the plate is used. The analytical model from Khabakhpasheva and Korobkin is used to study different boundary conditions and different conditions of the hinge between the plates. They also modelled the plates being moored with a spring. Riyansyah et al. focus on optimal design of the location and torsional stiffness of the hinge, regarding motions of the platform. Both models show the wide applicability of hydroelastic, simplified, models on VLFSs.

Lastly, [30] gives an analysis of the hydroelastic response statistics of a VLFS due to the stochastic character of wave and wind loads. They use modal (wet modes) superposition for the response of the platform. The stochastic response is obtained using a spectral approach and using linear transfer functions.

2.2 Wrinkling

When a membrane is in (uni/bi)-axial compression the phenomenon of wrinkling can occur. In the ocean engineering and offshore literature, research to wrinkling is hardly performed as the structures are usually designed far from the buckling instabilities [1]. However, an extensive amount of research has been performed on wrinkling of elastic/elastoplastic films which are buckling, wrinkling and folding on a surface of liquid. This section briefly summarises the literature regarding wrinkling experiments and observations not necessarily from engineering studies.

2.2.1 Governing Mechanism

In the paper by Li et al.[33], a review of the state-of-the-art in the year 2012 is given. This review contains some cases which will be discussed later in this section. Generally speaking, the authors conclude that wrinkling patterns are highly depending on the geometrical configuration of the system. By this means, the paper reviews experiments and numerical models on different scales (approx. from $\mathcal{O}\left(10^{-6}m\right)$ up to $\mathcal{O}\left(10^{-1}m\right)$). Furthermore, the definitions of wrinkling, folding and creasing are given by the authors (see **??**):

Wrinkling is chaotic or periodic surface deflections of a originally flat surface.

Folding is a buckling induced surface structure with localised deep surface valleys. They are often observed during the post buckling evolution of surface wrinkles of nearly inextensible thin films on spring foundation.

Creasing occurs with thin films that are soft (and hence extensible) and the shape is characterised by self-contact of the instability. Contrary to folding, creasing is not a post-buckling phenomena and

[1] For references about buckling in general or in marine structures the works of Brush et al. and Hughes et al.[31, 32].

hence bypasses the wrinkling state. Furthermore, creasing is highly sensitive to surface defects and perturbation whereas folds are relatively stable.

Hence, wrinkling and folding are two succeding mechanisms that occur when a membrane on a substrate is compressed. As mentioned in the review paper by Li et al.[33], but also by Rivetti, Rivetti and Neukirch, Diamant and Witten, Jambon-Puillet et al.[34, 35, 36, 37], the wrinkle-to-fold transition is governed by an energy balance between the potential energy of the membrane deflecting into the substrate and the potential bending energy.

In [38] and [39] the physics of wrinkling of thin sheets are discussed and scaling laws for the wave length and amplitude of wrinkles were derived.

$$\lambda \sim \left(\frac{B}{K}\right)^{1/4} \qquad A \sim \left(\frac{\Delta}{W}\right)^{1/2} \lambda \tag{2.1}$$

Where B is the bending stiffness of the sheet, K is the foundation stiffness and Δ/W is an imposed compressive strain. As seen in these scaling laws, the bending stiffness penalises short wave lengths and the foundation stiffness penalises long wavelengths.

2.2.2 Experimental Findings

Experimental findings regarding an inextensible membrane subject to a compression, resting on a substrate, were reported by Cerda et al., Cerda and Mahadevan, Pocivavsek et al.[40, 38, 39]. In [38], a distinction between compression and tension wrinkles is made using examples of people's skin. An example of a tensional wrinkle is depicted in figure 2.1 and as described by Cerda and Mahadevan they are formed because of lateral contractions in the material due to constraints at boundaries combined with pre-stress of the membrane. Tensional wrinkles are found on one's knee or elbow, typically [38]. Compression wrinkles, on the contrary, are formed on skin which is resting on a soft substrate (e.g. fat) and compressed such that the skin locally penetrates the substrate, leading to folds. Additionally, Pocivavsek et al.[39] elaborates the wrinkle-to-fold transition on different scales (see **??**). Here, the wave lengths are in the centimetre to micrometre range. Again, Pocivavsek et al. assume an inextensible sheet. From their scaling analysis, the findings are that the wrinkled state and the folded state of a membrane differ only in a higher order term from the enforcement of the inextensibility. Lastly, experiments were performed with a thin film inbetween two fluids with different densities and a film with a mass by Jambon-Puillet et al.[37].

2.2.3 Analytical and Numerical Mathematical Models

Besides the experiments that were performed by Cerda and Mahadevan and Pocivavsek et al., mathematical models for thin membranes resting on fluids (i.e. an elastic foundation) have been developed. Similar to the energy scalings used by Cerda and Mahadevan and [39], these models are derived by using different expressions for the potential energy in the membrane (due to bending) and in the foundation. Audoly used two expressions of a nonlinear foundation (referred to as a floating foundation and a nonlinear Winkler foundation) to derive general formulations for the amplitude of the localised buckling phenomena and compared the results to the experiments by Pocivavsek et al.. Additionally, [36] provides an analytical solution for the wrinkle to fold transition. Later on, this was improved by [34] who generalised the solution of Diamant and Witten to a continuous family of solutions which yield a non-symmetric shape of the fold. Later on Rivetti and Neukirch[35] compute equilibrium and stability of the solutions and also secondary bifurcation points. In the work of Diamant and Witten, Rivetti and Rivetti, the following differential equation was solved:

$$\frac{\partial^4\theta}{\partial s^4} + \frac{3}{2}\left(\frac{\partial\theta}{\partial s}\right)^2 \frac{\partial^2\theta}{\partial s^2} + P\frac{\partial^2\theta}{\partial s^2} + \sin(\theta) = 0 \tag{2.2}$$

A numerical study of an elasto*plastic* film on a soft substrate was performed by Cao et al.[43]. In this study, the substrate was modelled as an elastic 'foam' and the film was modelled as a membrane with a

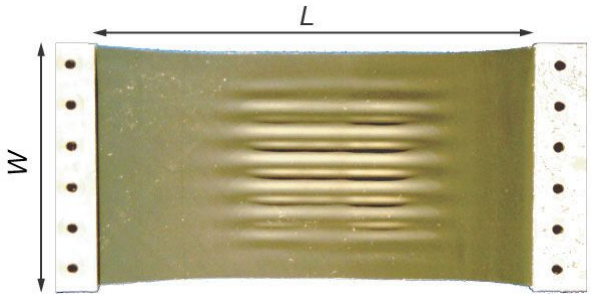

Figure 2.1: Wrinkling due to tension of a membrane because the clamped boundaries on the left and on the right prevent lateral contraction of the membrane. Image is courtesy of [41].

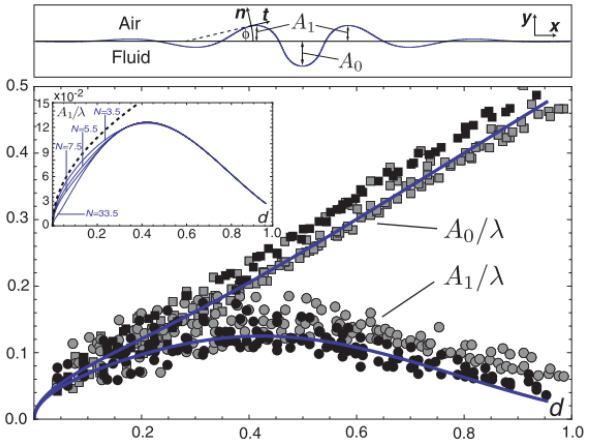

Figure 2.2: Wrinkle-to-fold transition from experimental data. The top figure gives definitions of A_0 and A_1 and the bottom figure presentes the evaluation of A_0 (squares) and A_1 (circles) for increasing non-dimensional compression distance d. It can be seen that for increasing d, A_1 decreases and A_0 increases, hence a fold forms. Image is courtesy of [39].

certain yield strength. When the applied displacement on the boundaries of the film was above a certain critical value, wrinkles occured. Additionally, an increase of the displacements resulted in localised creasing. According to the authors, creasing occured due to plastic deformation of the substrate. However, this is contradictory to the definitions given by Li et al.[33]. Cao et al. found that for an elastic model, thus a model without plasticity, no creasing appeared and they acknowledge that creasing can also be explained by inextensibility of elastic films.

Vella et al.[44] investigates the effect of wrinking of a ball which is pressurised internally. This analysis, which is based on a spherical description of a thin membrane. Consequently, the limits of very weakly pressurised shells as well as stongly pressurised shells. Their findings are that for low internal pressures a fixed number of wrinkles is observed (referred to as *polygonal structures*) whereas for large pressures the number of wrinkles increases. Additionally the authors found that the internal pressure affects the critical indentation depth for localised wrinkles. Taffetani and Vella[45] continued the study on pressurised shells by elaborating further on the number of wrinkles as well as the effects of large indentation depths.

In the paper of Ning et al.[46], the effects of a film on a foundation for different stiffness ratios and inhomogeneous materials has been investigated. The authors used a FEM package to model post-buckling behaviour of the beam starting with a buckled beam with infinitesmal amplitude. The conclusions from the study were that the ratio between the bending stiffness and the foundation stiffness have a great impact on the evolution of the wrinkles as well as the final morphology.

Lastly, some studies have been performed in the fields of elastocapillary instabilities [47, 48], delamination of floating elastic sheets [49] and wrinkling of sandwich columns using the core as 'elastic foundation' [50]. These works are presented here for further reference on the topic of wrinkling and folding, but their relevance to this work is small.

2.3 Isogeometric Analysis

2.3.1 Origins of Isogeometric Analysis

Isogeometric Analysis was proposed by Hughes et al. [51] in 2005. In this paper, the authors mention the link with and inspiration by Computer Aided Design (CAD), more specifically with B-splines and Non-Uniform Rational B-splines (NURBS). As motivated in the paper, using NURBS for analysis purposes circumvents the need for meshing of the geometry generated by CAD. Furthermore, NURBS allow the use of h, p and hp-refinements and additionally the use of k-refinement which increases the continuity of the basis functions systematically, lately discussed in more detail by [52]. Later on, the book [53] by Cottrell et al. was published which covers a wide variety of applications of Isogeometric Analysis, additionally to those mentioned in [51]. Furthermore, the book covers the basics of Isogeometric Analysis in great detail. In 2015, Nguyen et al.[54] published a paper which gives a general overview of the state-of-the-art in that time. This paper covers applications, alternative discretisations and notes on computational aspects. These topics will be discussed in subsequent subsections. The basics of Isogeometric Analysis are futher covered in chapter 4.

2.3.2 Isogeometric Analysis for Structural Mechanics

Isogeometric Analysis for structural mechanics has been developed over the past years. The Kirchhoff-Love Shell, the Reissner-Mindlin Shell, solid, cable and beam elements have been developed in the past. The Kirchhoff-Love shell formulation is of special interest in this study, as the Kirchhoff assumption is also made here. The literature on an isogeometric Reissner-Mindlin shell formulation is briefly given for the sake completeness.

Kiendl et al. published several papers on the Kirchhoff-Love formulation in the Isogeometric Analysis framework [55, 56, 57]. In [55], the formulation was developed for thin shell structures with large deformations and neglegible through-thickness deformations induced by shear effects(Kirchhoff hypothesis, see **??**). Later on, the "Bending Strip Method" was developed in [56] to couple multiple NURBS patches. Lastly, [57] extends the Kirchhoff-Love shell formulation for hyper-elastic materials, such as rubber-like materials and biological tissues. Applications of different material models on biological tissues are also given in [58] and [59] gives an application of a contact model using the Kirchhoff-Love shell formulation.

Benson et al. [60] derive a Reissner-Mindlin shell element. The derived elements were tested on one linear elastic case (pinched cylinder) and four non-linear elasto-plastic cases, including buckling of a cylinder and square tube. The element is implemented as user-defined element in LS-DYNA and the implementation shows effective use of quadratic and quartic shells. Furthermore, Beirão da Veiga et al. [61] presents an isogeometric method for the Reissner-Mindlin shell formulation which is locking-free, i.e. over-stiff solutions in the thin plate limit ([62]). Furthermore, they show for general boundary conditions that the method is uniformly stable and that it satisfies optimal convergence estimates. The derivations are formally mathematical.

In [63] an isogeometric cable element is presented. This cable element is developed for cables under self-weight or uniformly distributed loads. In the paper, the element is validated for different cable net configurations. For slack cables where the sag effect is significant, the equilibrium state of the cable should be defined since the behaviour of the structure is sensitive. In order to cope with this problem, a penalty technique has been used to calculate the equilibrium configuration of the cable.

Raknes et al. [64] derive a cable element from 3D continuum mechanics equations. In their formulation, bendings stiffness is included, under the Kirchhoff hypothesis. Besides providing some interesting validation cases, such as the bow and arrow problem to couple cables and beams, or the opening umbrella to couple a truss and a Kirchhoff-plate, they conclude that the bending term in the cable element formulation works as a stabilising factor in the computations. This is especially the case when modelling

beams under compression. Additionally, [63] developed an isogeometric cable element under self weight and elaborated on sagging cable nets using a penalty technique to calculate the equilibrium configuration.

Lee and Park [65] and Luu et al. [66] derive Timoshenko beam models with an isogeometric approach. In the former paper, it is concluded that the beam model is very efficient and robust with k refinements. Furthermore, they found that higher order elements do not show shear-locking effect and the mode shapes are represented compared to FEA results. In the latter paper by Luu et al. [66], the focus is on the free-form vibration of curved beams. They conclude that rotary inertia and shear are important for thick, elliptic rings and that the use of NURBS allows for efficient modelling of arbitrarily curved beams.

[67, 68] present the work of Cazzani et al. on curved beams with IGA. Basically, this is an extension of the 'regular' IGA beam elements. Besides the formulations and implementation of the curved beam elements, both papers provide validation cases for similar structures. In the conclusion of the paper [68], the authors stress that the use of 'regular' IGA beam elements works for relatively small curved beams. When the initial curvature is present, however, the need for their constitutive model for curved beams needs to be adopted. The benchmarks defined by [67, 68] are used for verification later in this report. (see section 5.3.4).

The works of Weeger et al., Kolman et al., Luu et al., Qin et al.[69, 70, 66, 71] focus on structural vibrations. Applications of IGA for structural vibrations is beneficial for panels with curved stiffeners (see [71]), curved geometries such as rings (see [66]), but also because the method outperforms the Finite Element Method (FEM) in eigenfrequency and mode shape calculation, as discussed in the following subsection.

2.3.3 Comparison to Finite Element Analysis

As mentioned in section 2.3.1 Isogeometric Analysis originates from the idea of a seamless integration between CAD and Finite Element Analysis (FEA). The fundamental difference between Isogeometric Analysis and FEA, however, is that basis functions have a compact support (element-wise) in case of FEA, whereas they have a global (patch-wise) support in Isogeometric Analysis. A domain can be sub-devided into multiple patches and per patch, there are usually multiple non-zero basis functions. More detail will be given in chapter 4.

Regarding the performance of FEA and Isogeometric Analysis, few comparing studies have been performed in the past. Furthermore, most (dis)advantages of Isogeometric Analysis compared to FEA are shown by means of application or hypothesis, rather than by formal mathematical proofs.

Regarding performance of Isogeometric Analysis compared to FEA, some publications in literature are recalled here. First of all, [72] compared p-method finite elements with a NURBS-based approach and concluded that for structural dynamics, the whole frequency spectrum converges with p whereas in FEA the errors in the higher-order modes even diverge with p. In [73] and [74] two applications comparing Isogeometric Analysis with FEA were given. In the present studies, stunning accuracy and fast computing times were observed for Isogeometric Analysis compared to FEA.

Regarding structural vibrations, Weeger et al. studied non-linear vibrations of an Euler-Bernoulli beam in the IGA and FEA framework. The conclusions were that IGA outperforms FEA since IGA does not show so-called optical branches (see **??**) and that the number of degrees of freedom to reach a certain accuracy is lower. Furthermore, it was found that k-refinement were more beneficial than conventional p-refinement procedures for numerical results. Additionally, [70] performed an analysis of free vibrations of simple-shaped elastic samples using solid elements and also found that the number of degrees of freedom that is needed for IGA and FEM for similar accuracy is significantly smaller for IGA, and that the number of Gauss-evaluations for assembly of the system is also smaller, although IGA has less-sparse systems. [71] considered stiffned panels with curved stiffners and compared IGA to FEA. Besides the advantage that IGA can exactly describe curved stiffeners, it was found that IGA outperformed FEA on

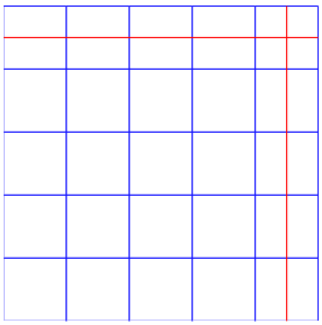

Figure 2.3: [75]

accuracy for a smaller amount of degrees of freedom compared to FEA.

2.3.4 Meshing Techniques

B-splines and NURBS are defined by a set of knots in a knot vector. A disadvantage of those is that they are generally not able to represent topologies that contains holes. Furthermore, as they are defined by a tensor product of knot vectors, local refinements are inefficient, as shown in figure 2.3 [75]. A solution to this is the use of T-splines, which are introduced in [76]. As discussed by Bazilevs et al.[75], T-splines allow for watertight merging of patches and efficient local mesh refinement. The efficiency of adaptive mesh refinement with T-splines compared to ordinary B-splines is discussed in [77], although improvements in the algorithm were still needed.

Application of T-splines has been done for Reissner-Mindlin shells [78], where an algorithm has been developed to calculate surface normals on a T-mesh. Furthermore, [79] utilises T-splines for analysis of a bioprosthetic heart valve. Furthermore, Kostas et al. [80] present results from IGA-BEM optimisation of ship hulls with respect to their resistance. Here T-splines are used to describe the geometry of the vessel.

2.3.5 Computational Aspects

Principally, Isogeometric Analysis is based on variational forms, similarly to FEA [2]. The integrals in the variational form are usually computed using quadrature rules (e.g. GaußQuadrature) per element. In case of NURBS and B-splines, such quadrature rules are far from efficient, due to the fact that NURBS and B-splines pose some degree of smoothness across element boundaries, as illustrated in [82]. Hence, a computationally very expensive step in Isogeometric Analysis is integration of the variational form and hence assembly of the system. As this thesis will not further look into optimal quadrature for Isogeometric Analysis, the reader is adviced to read the papers [82] and [83]. In this work, Gaußquadrature is used for integration.

Collier et al. discusses the computational costs that are associated with k-refinements (i.e. refinement of the continuity) for direct solvers [84] and for iterative solvers [85]. Garcia et al. [86] provides the 'refined IGA' (rIGA) method which uses separators in the domain (lines of reduced continuity) that make the resulting linear system more suitable to solve for direct solvers.

2.3.6 Recent Developments (2015-2018) and Future Directions

`What is going on?`

[2] See [81] amongst others for an overview of the Finite Element Method.

```
What is left?
Something about Quadrature?
```

2.4 Fluid Structure Interaction (FSI)

Fluid-structure interaction, often abbreviated as FSI, is the study of the interaction between a fluid (liquid or gas) and a structure. Theoretically, every structure has a finite stiffness such that every fluid that applies a pressure on this structure makes the structure deform. Hence, one can state that FSI is always present. Obviously, there are different examples of cases where the FSI effect is more relevant than others. Some examples are illustrated in figure 2.4. Throughout this section, references are made to applications of hydro-/aeroelasticity and FSI to illustrate the broad application as well as different methods that are utilised.

In literature, FSI cases are often referred to as *hydro-* or *aeroelastic* cases. Hydro-/Aeroelasticity is often an analytical study of FSI cases where the loads are often applied as a function of the structural displacements. Examples include a dropping wedge, widely known from [87, 88], and later extended to a flexible wedge by [89] amongst others; slamming of a wave on a plate [90]; or studies on vibrations in the frequency domain, e.g. hydroelasticity of a sloshing fluid in a tank with deforming side walls [91]. In all such cases, hydrodynamic added mass and damping influence the structural dynamic behaviour. Often, structures are considered elastic and fluid models are simplified rather than using full Navier-Stokes fluid descriptions.

On the contrary, references to FSI contain hydro-/aeroelastic cases and cases with more complex fluid/structure models and with strong coupling between these two. Strong or weak coupling in Fluid Structure Interaction is often defined as 'how much the fluid and structure are influenced by eachother'. In case of strongly coupled FSI, the change of the velocity and pressure fields in the fluid are significantly influenced by the structural deformations and vice versa. In this thesis, emphasis will be on the strongly coupled FSI models incorporating large structural deformations.

2.4.1 Monolithic vs. Partitioned FSI

As defined above, FSI is about coupling between fluid and structural models or *solvers*. The coupling between these models can be done in two ways; monolithically and partitioned (or segregated). In the former case, the fluid and structure governing equations are solved together. In the latter case, separate fluid and structure solvers are utilised and coupled using a data exchange.

Partitioned FSI solvers have the advantage that they utilise existing fluid and structure solver and hence the features included in these solvers (e.g. turbulence, plasticity) are available for FSI calculations. Futhermore, these separate solvers are usually optimised for their purpose and hence 'the best of both worlds' is taken. A disadvantage of partitioned solvers is that the stronger the FSI coupling, the more iterations between the solvers are needed to get a sufficiently accurate solution [94]. Furthermore, the partitioned approach allows for using different time steps for the structural and fluid models. Several time integration schemes for fluid and structural models in case of a partitioned coupling are discussed in [95].

Contrary to partitioned FSI solvers, monolithic solvers are usually newly developed and do not utilise existing solvers for fluid and structure. The advantage of these solvers is that they can be computationally efficient for strongly coupled problems as no subiterations are needed compared to the partitioned approach, since fluid and structure are assembled in the same matrix system. This also guarantees convergence of the system. A downside of solving with one system is that the time step for the structure and the fluid is the same, although this is usually not needed. [96]

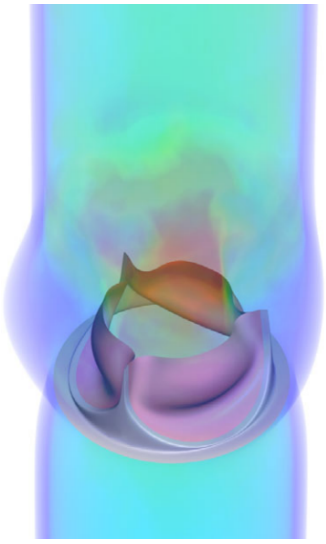

(a) *Application in biomedical engineering*: Fluid-Structure Interaction model of a bioprosthetic heart valve. In this model, the structure (the valve) is fully submerged in the fluid. Using this FSI model, which has been developed by [79], the design of bioprosthetic heart valves can be optimised for lifetime.

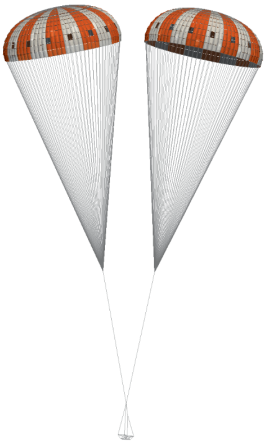

(b) *Application for sails, parachutes, and other thin membranes*: Fluid-Structure Interaction of a cluster of parachutes for spacecraft landing [92]. This type of Fluid-Structure interaction combines lightweight structures (e.g. parachutes or sails) with turbulent flows (e.g. air), which is an example of strongly coupled fluid-structure interaction.

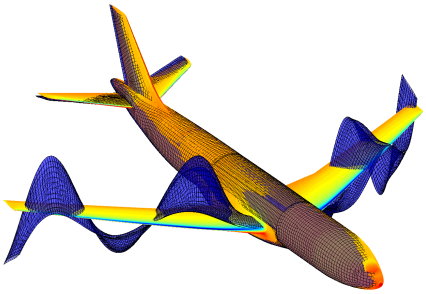

(c) *Application in aerospace engineering*: Aeroelasticity/Fluid-Structure interaction of an airplane (magnified structural deformations). As seen in this picture, the deformation of the wings of an airplane in flight are relatively large. (Self-excited) Oscillation of the wings due to turbulent air is called *wing flutter* and is a long studied subject in aerospace engineering. ⋆

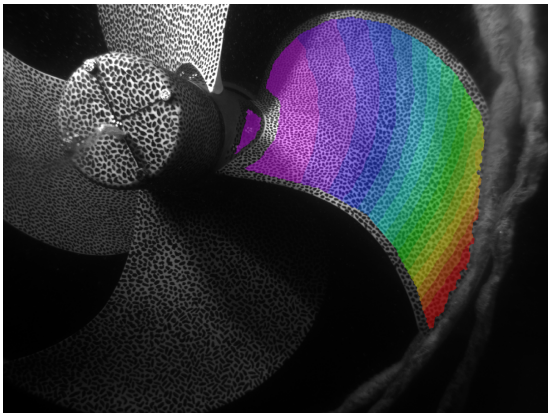

(d) *Application in maritime engineering*: Fluid-Structure Interaction model of a composite propeller (GreenProp project †). By designing the composite structure of propeller blades, advances in the efficiency and cavitation inception of the propeller are obtained. The deformation of the propeller blade in the wake field of a ship is an example of FSI for maritime purposes. [93]‡ .

Figure 2.4: Different application where Fluid-Structure Interaction is relevant.
⋆: Image from German Aerospace Center (DLR) https://www.dlr.de/ae/en/desktopdefault.aspx/tabid-9410/
†: See: https://www.tudelft.nl/3me/afdelingen/maritime-and-transport-technology/research/ship-and-offshore-structures/research/greenprop/
‡: Picture from Solico, partner in the GreenProp project (https://www.solico.nl/projects/greenprop-composite-propeller)

2.4.2 Grid matching

Besides coupling of the interaction of the fluid and the structure, matching of both grids is a main challenge in FSI. This challenge is present when different mesh sizes are used for the fluid and structure models. Hence, it mainly occurs for partitioned FSI algorithms. Usually, the mesh size of the fluid model is smaller than that of the structural model, which implies that pressures have to be combined on a coarser structure mesh and that displacements have to be interpolated on a finer fluid mesh. In [97], some mesh coupling procedures are evaluated regarding accuracy and computational costs. The most efficient methods discussed in this paper are Thin Plate Splines (TPS), Multi-quadric biharmonic splines (MQ) and Radial Basis Functions (RBF).

In [98], a NURBS-based coupling of the fluid and structure model is developed. Here, Isogeometric Analysis is applied for the structure and a so-called 'NURBS-Enhanced Finite Element Method' is used for the flow simulations. In this way, they achieved a direct transfer of the necessary coupling variables over the interface, as the NURBS shape can be identical despite the number of points.

2.4.3 Mesh Deformation

In FSI problems, one usually separates a number of domains based on being a fluid or a structure. Hence, a minimum of two domains is present in FSI calculations, extended to more if there are multiple fluids or structures. Since fluid and structure are solved on their own domain, they are defined on separate grids. The deformation of the structure, however, implies the fluid domain to deform. Hence, the mesh on which the fluid is solved is changing. On the one hand, one can fix the fluid mesh and let the structure move through the mesh, to which is referred as the *immersed boundary method*. On the other hand, the fluid mesh can be attached to the structure mesh and hence deforms which the structure.

The immersed boundary method has the advantage that the fluid mesh can be kept cartesian and structured and fixed over time. This implies that there is no need for and Arbitrary Lagrangian Eulerian (ALE) fluid and structure description, in which the velocity of the mesh is incorporated in the Navier-Stokes equation (see for instance [75] amongst others). On the other hand, the interface between the structure and the fluid is moving through the fluid domain. This implies the need for an algorithm for determination of the location of this interface, as developed by [99] amongst others.

When the fluid and structure domains are coupled and connected, mesh motions are present for both domains. This implies the use of the ALE formulations for structure and fluid. This formulation for the fluid takes into account convection of the fluid through the mesh due to mesh motion. In general, there are two types of mesh motion techniques for unstructured grids; grid-connectivity and point-by-point schemes [100].
In the former method, grid connectivity information together with a spring analogy of the mesh lines is used to calculate the position of each individual node, making this technique computationally expensive. For large deformations, linear elasticity solvers can be used for mesh deformation [101, 102], so that the domain is considered as a (curved) plate or a solid where the boundary displacements are applied. [102] investigated the use of different material models and different material parameters. It was concluded in their paper that the Saint-Venant Kirchhoff model is sufficient to acquire promising results for non-trivial geometries and that future work should focus on non-homogeneous distribution of material parameters and their influence on the mesh.
In the latter method, the points in the meshed are moved according to their coordinate in the undeformed case and it requires solving a system as large as the number of boundary nodes. Calculation of the deformed mesh can then for instance be done using radial basis function interpolation as described by [100]. In this paper, it is concluded that the radial basis function mesh deformation algorithm is an efficient and accurate method compared to the grid-connectivity scheme.

In general metrics for meshes were investigated by Lipton et al.[103] for isogeometric analysis specifically. However, the performance of mesh deformation techniques is out of the scope of this study and

hence the work of Lipton et al. is for further reading.

3 | Governing Equations and Mathematical Preliminaries

3.1 Structural Model

In this chapter the foundations of the structural model are laid. The goal of this chapter is to provide a motivation for and an explanation of the structural models that are used in this study. Hereby, the first section mentions the assumptions of the structural model and takes this as a starting point for the derivation of the stress-strain relationship. In the second section, the principles are applied on a 1D element to derive a beam element. In this section, the relation with a catenary element for which bending stiffness is by definition neglected, is also covered.

3.1.1 Kirchhoff Hypothesis

In the forthcoming derivations, the Kirchhoff Hypothesis is a fundamental hypothesis for the deformation of the beam or shell. The theory makes the following three assumptions for the displacement field [104, sec. 6.2.1]:

1. Straight lines perpendicular to the mid-surface (i.e. transverse normals) before deformation, remain straight after deformation.
2. The transverse normals do not experience elongation (i.e. they are inextensible)
3. The transverse normals rotate such that they remain perpendicular to the mid-surface after deformation. Hence, no shear of a material element is present.

Based on these assumptions, the coordinates of an arbitrary point $\mathbf{X}$ in the undeformed configuration can be expressed into the formulation of the coordinates in the deformed configuration $\mathbf{x} = \mathbf{X}+\mathbf{u}$. Firstly, based on the third assumption, we note that the in-plane transverse shears must be zero. Hence, the in-plane displacements are the sum of the in-plane displacements of the mid-plane u_0, v_0 and the contribution of the out-of-plane rotations of the mid-plane times the distance to the mid-plane $z\frac{\partial w_0}{\partial x}, z\frac{\partial w_0}{\partial y}$. [62, p.97] Hence,

$$u(x,y,z) = u_0(x,y) - z\frac{\partial w_0}{\partial x},$$
$$v(x,y,z) = v_0(x,y) - z\frac{\partial w_0}{\partial y}.$$

Furthermore, based on the first two assumptions, the term $\frac{\partial w}{\partial z}$ must be equal to zero. In other words, the elongation of the normals is zero. Lastly, for the vertical deflection, the displacements due to the rotation of the mid-plane (assumed to be moderate, i.e. $10-15°$) can be neglected. Hence, the mid-plane displacement is the only effect that causes the vertical deflection of a point:

$$w(x,y,z) = w_0(x,y).$$

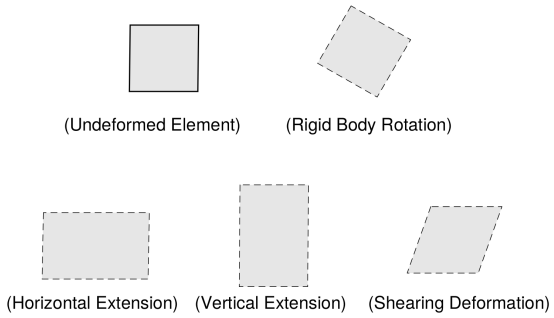

Figure 3.1: Typical deformations of a rectangular element, adopted from [105]

In tensor notation, let us denote the displacement vector by $\boldsymbol{u}$. Then,

$$u_\alpha = u_\alpha^0 - x_3 \frac{\partial u_3^0}{\partial x_\alpha}, \qquad \alpha = 1, 2$$
$$u_3 = u_3^0$$

3.1.2 Strain-displacement relationship

In the book of Sadd [105] the derivation of simple linear strain is clearly derived from the typical deformations of a rectangular element (see figure 3.1).

In a more general sense, the Green strain tensor can be used to describe the strains due to deformations of a medium. This tensor is denoted by:

$$\underline{\underline{\boldsymbol{E}}}^G = \frac{1}{2}\left[(\nabla \boldsymbol{u}) + \nabla \boldsymbol{u}^T + (\nabla \boldsymbol{u}) \cdot \nabla \boldsymbol{u}^T\right] \tag{3.1}$$

Here, the nabla operator ∇ consists of the derivatives with respect to the initial configuration. Furthermore, the vector $\mathbf{u}$ contains the displacements. In index notation, this tensor is denoted by:

$$E_{ij}^G = \frac{1}{2}\left[\frac{\partial u_i}{\partial x_j} + \frac{\partial u_j}{\partial x_i} + \sum_{k=1}^{3} \frac{\partial u_k}{\partial x_i}\frac{\partial u_k}{\partial x_j}\right] \tag{3.2}$$

Here, the first two derivatives contribute to the linear strains and the last term is the non-linear strain contribution. With the assumption that strains in normal directions and in-plane shear effects are small, the Von Kármán strains can be derived (see section A.1). Here, the strains related to the z-direction are zero and the strain tensor hence is determined by the strains in and curvature of the plate:

$$\underline{\underline{\boldsymbol{E}}} = \begin{bmatrix} E_{11} & E_{12} \\ E_{21} & E_{22} \end{bmatrix} = \begin{bmatrix} \varepsilon_{11} & \varepsilon_{12} \\ \varepsilon_{21} & \varepsilon_{22} \end{bmatrix} + x_3^0 \begin{bmatrix} \kappa_{11} & \kappa_{12} \\ \kappa_{21} & \kappa_{22} \end{bmatrix}$$

3.1.3 Stress-Strain relationship

For the relationship between stresses and strains, the generalised Hooke's law is used. This law relates strains to stresses using the following formulation (in index notation):

$$\sigma_{ij} = \frac{E}{1+\nu} E_{ij} + \frac{\nu E}{(1+\nu)(1-2\nu)} \sum_{k=1}^{3} E_{kk}\delta_{ij} \tag{3.3}$$

Where ν is Poisson's ratio, E is Young's modulus and δ_{ij} is the Kronecker delta function. In Voight notation, this becomes:

$$\begin{bmatrix}\sigma_{11}\\ \sigma_{22}\\ \sigma_{33}\\ \sigma_{12}\\ \sigma_{13}\\ \sigma_{23}\end{bmatrix} = \frac{E}{(1+\nu)(1-2\nu)}\begin{bmatrix}1-\nu & \nu & \nu & 0 & 0 & 0\\ \nu & 1-\nu & \nu & 0 & 0 & 0\\ \nu & \nu & 1-\nu & 0 & 0 & 0\\ 0 & 0 & 0 & 1-2\nu & 0 & 0\\ 0 & 0 & 0 & 0 & 1-2\nu & 0\\ 0 & 0 & 0 & 0 & 0 & 1-2\nu\end{bmatrix}\begin{bmatrix}E_{11}\\ E_{22}\\ E_{33}\\ E_{12}\\ E_{13}\\ E_{23}\end{bmatrix} \tag{3.4}$$

However, from the Von Kármán strains, we know that $E_{13} = E_{23} = E_{33} = 0$. Hence, Hooke's law simplifies to:

$$\begin{bmatrix}\sigma_{11}\\ \sigma_{22}\\ \sigma_{12}\end{bmatrix} = \frac{E}{(1+\nu)(1-2\nu)}\begin{bmatrix}1-\nu & \nu & 0\\ \nu & 1-\nu & 0\\ 0 & 0 & 1-2\nu\end{bmatrix}\begin{bmatrix}E_{11}\\ E_{22}\\ E_{12}\end{bmatrix} \tag{3.5}$$

Or, under plane stress assumptions:

$$\begin{bmatrix}\sigma_{11}\\ \sigma_{22}\\ \sigma_{12}\end{bmatrix} = \frac{E}{(1-\nu^2)}\begin{bmatrix}1 & \nu & 0\\ \nu & 1 & 0\\ 0 & 0 & 1-\nu\end{bmatrix}\begin{bmatrix}E_{11}\\ E_{22}\\ E_{12}\end{bmatrix} \tag{3.6}$$

In tensor notation, this will be denoted as:

$$\underline{\underline{\boldsymbol{\sigma}}} = \mathrm{D}\underline{\underline{\boldsymbol{E}}}$$

3.1.4 The principle of Virtual Work

The principle of virtual work is extensively covered in the book Reddy [62, ch. 2]. The method is mostly suitable for problems where force and moment equilibrium are not easily used to obtain the governing equations in a volume element. Furthermore, the principle of virtual work involves boundary conditions and can be used to obtain weak forms for FEA or IGA.

The main concept in the principle of virtual work is to apply virtual displacements on a body and equate the total energy to zero. For structural dynamics, this means that the sum of the internal workand the external work needs to be equal to zero, i.e.

$$\Pi = \delta W_I + \delta W_E = 0 \tag{3.7}$$

Where Π is the total energy in the system. Furthermore, δW_I is the internal work and δW_E is the external work, respectively given by:

$$\delta W_I = \int_{\Omega^*} \underline{\underline{\boldsymbol{\sigma}}} : \delta\underline{\underline{\boldsymbol{E}}}\,\mathrm{d}\Omega^* \tag{3.8}$$

$$\delta W_E = -\left(\int_{\Omega^*} \mathbf{f}\cdot\delta\mathbf{u}\,\mathrm{d}\Omega^* + \int_{\partial\Omega_\sigma} \mathbf{T}\cdot\delta\mathbf{u}\,\mathrm{d}\Gamma\right) \tag{3.9}$$

Here, the volumetric domain is denoted by Ω^* with boundary $\partial\Omega^* = \partial{\Omega^*}_\sigma \cup \partial{\Omega^*}_u$. Here, $\partial{\Omega^*}_\sigma$ is the boundary where traction is applied and $\partial{\Omega^*}_u$ is the boundary where displacements are applied. The latter implies that no virtual displacements are present and hence that it is not present in the virtual work formulation.

Furthermore, for dynamical systems, Hamilton's principle can be used, which states [62]:

> Of all possible paths that a material particle could travel from its position at time t_1 to its position at time t_2, its actual path will be one for which the integral
>
> $$\int_{t_1}^{t_2} K - W\,\mathrm{d}t \tag{3.10}$$

is an extremum.

Here, W is the potential energy in the system, given by the sum of the internal and external work, and K is the kinetic energy of the system, given by:

$$K = \int_{\Omega^*} \rho \frac{\partial \mathbf{u}}{\partial t} \cdot \frac{\partial \mathbf{u}}{\partial t} \, \mathrm{d}\Omega^* \tag{3.11}$$

For further derivations under the Kirchhoff hypothesis, it is convenient to introduce the in-plane forces and bending moments $\underline{\underline{\boldsymbol{N}}}$ and $\underline{\underline{\boldsymbol{M}}}$. These are defined by the zeroth and first moment of the stress over the plate thickness. Hence,

$$\begin{aligned}
\underline{\underline{\boldsymbol{N}}} &= \int_{-\frac{h}{2}}^{\frac{h}{2}} \mathrm{D}\underline{\underline{\boldsymbol{E}}} \, \mathrm{d}z &&= \int_{-\frac{h}{2}}^{\frac{h}{2}} \mathrm{D}\underline{\underline{\boldsymbol{\varepsilon}}} \, \mathrm{d}z &&= \mathrm{D}h\underline{\underline{\boldsymbol{\varepsilon}}} \\
\underline{\underline{\boldsymbol{M}}} &= \int_{-\frac{h}{2}}^{\frac{h}{2}} x_3 \mathrm{D}\underline{\underline{\boldsymbol{E}}} \, \mathrm{d}z &&= \int_{-\frac{h}{2}}^{\frac{h}{2}} x_3^2 \mathrm{D}\underline{\underline{\boldsymbol{\kappa}}} \, \mathrm{d}z &&= \frac{\mathrm{D}h^3}{12}
\end{aligned}$$

This yields (in Voigt notation):

$$\begin{aligned}
\begin{bmatrix} N_{11} \\ N_{22} \\ N_{12} \end{bmatrix} &= \frac{Eh}{1-\nu^2} \begin{bmatrix} 1 & \nu & 0 \\ \nu & 1 & 0 \\ 0 & 0 & 1-\nu \end{bmatrix} \begin{bmatrix} \varepsilon_{11} \\ \varepsilon_{22} \\ \varepsilon_{12} \end{bmatrix} \\
\begin{bmatrix} M_{11} \\ M_{22} \\ M_{12} \end{bmatrix} &= \frac{Eh^3}{12(1-\nu^2)} \begin{bmatrix} 1 & \nu & 0 \\ \nu & 1 & 0 \\ 0 & 0 & 1-\nu \end{bmatrix} \begin{bmatrix} \kappa_{11} \\ \kappa_{22} \\ \kappa_{12} \end{bmatrix}
\end{aligned}$$

Hence, the virtual work statement from equation (3.9) becomes:

$$\begin{aligned}
\delta W_I &= \int_{\Omega^*} \mathrm{D}(\underline{\underline{\boldsymbol{\varepsilon}}} + x_3 \underline{\underline{\boldsymbol{\kappa}}}) : \delta(\underline{\underline{\boldsymbol{\varepsilon}}} + x_3 \underline{\underline{\boldsymbol{\kappa}}}) \, \mathrm{d}\Omega^* \\
&= \int_{\Omega} \underline{\underline{\boldsymbol{N}}} : \delta\underline{\underline{\boldsymbol{\varepsilon}}} + \underline{\underline{\boldsymbol{M}}} : \delta\underline{\underline{\boldsymbol{\kappa}}} \, \mathrm{d}\Omega
\end{aligned}$$

Where Ω denotes the xy-plane.

3.1.5 Euler-Bernoulli Beam Equation

In section A.2 several formulations for the Euler-Bernoulli beam including their weak forms are derived. Firstly, the full non-linear formulation of the Euler-Bernoulli beam using the previously derived strain-displacement and stress-strain models is (see equation (A.6)):

$$\begin{aligned}
-EA\left(\frac{\partial^2 u_0}{\partial x^2} + \frac{\partial w_0}{\partial x}\frac{\partial^2 w_0}{\partial x^2}\right) &= \rho A \ddot{u}_0 + t \\
-EA\frac{\partial}{\partial x}\left[\left(\frac{\partial u_0}{\partial x} + \frac{1}{2}\left(\frac{\partial w_0}{\partial x}\right)^2\right)\frac{\partial w_0}{\partial x}\right] + EI\frac{\partial^4 w_0}{\partial x^4} &= \rho A \ddot{w}_0 + p
\end{aligned} \qquad \text{(see equation (A.6))}$$

With corresponding weak form:

$$\begin{cases} \text{Find } u_0 \in H^1(\Omega),\ w_0 \in H^2(\Omega),\ \Omega = (x_1, x_2) \in \mathbb{R}^1 \text{ s.t.} \\ \\ \displaystyle\int_{x_1}^{x_2} EA\frac{\mathrm{d}\psi}{\mathrm{d}x}\left(\frac{\mathrm{d}u_0}{\mathrm{d}x} + \frac{1}{2}\left(\frac{\mathrm{d}w_0}{\mathrm{d}x}\right)^2\right) + \psi\rho A\ddot{u}_0\,\mathrm{d}x - EA\left[\psi\left(\frac{\mathrm{d}u_0}{\mathrm{d}x} + \frac{1}{2}\left(\frac{\mathrm{d}w_0}{\mathrm{d}x}\right)^2\right)\right]_{x_1}^{x_2} = \int_{x_1}^{x_2} \psi t\,\mathrm{d}x \\ \\ \displaystyle\int_{x_1}^{x_2} \varphi\rho A\ddot{w}_0 + EA\frac{\mathrm{d}\varphi}{\mathrm{d}x}\left[\frac{\mathrm{d}w_0}{\mathrm{d}x}\left(\frac{\mathrm{d}u_0}{\mathrm{d}x} + \frac{1}{2}\left(\frac{\mathrm{d}w_0}{\mathrm{d}x}\right)^2\right)\right] + EI\frac{\mathrm{d}^2\varphi}{\mathrm{d}x^2}\frac{\mathrm{d}^2w_0}{\mathrm{d}x^2}\,\mathrm{d}x + \\ \quad + \left[-EA\left\{\varphi\frac{\mathrm{d}w_0}{\mathrm{d}x}\left(\frac{\mathrm{d}u_0}{\mathrm{d}x} + \frac{1}{2}\left(\frac{\mathrm{d}w_0}{\mathrm{d}x}\right)^2\right)\right\} + EI\left\{\varphi\frac{\mathrm{d}^3w_0}{\mathrm{d}x^3} - \frac{\mathrm{d}\varphi}{\mathrm{d}x}\frac{\mathrm{d}^2w_0}{\mathrm{d}x^2}\right\}\right]_{x_1}^{x_2} = \int_{x_1}^{x_2} \varphi p\,\mathrm{d}x \\ \\ \forall\varphi \in \Sigma(\Omega) \end{cases}$$

(See equation (A.11))

Neglecting horizontal displacements, the result from equation (A.7) is obtained. Here, only one equation is left. Basically, this equation uses non-linear strains, resulting from vertical deflections only.

$$-EA\frac{3}{2}\frac{\partial^2 w_0}{\partial x^2}\left(\frac{\partial w_0}{\partial x}\right)^2 + EI\frac{\partial^4 w_0}{\partial x^4} = \rho A\ddot{w}_0 + p. \qquad \text{(see equation (A.7))}$$

The corresponding weak form is:

$$\begin{cases} \text{Find } w_0 \in \Sigma(\Omega) = H^2(\Omega),\ \Omega = (x_1, x_2) \in \mathbb{R}^1 \text{ s.t.} \\ \\ \displaystyle\int_{x_1}^{x_2} -\varphi\rho A\ddot{w}_0 + \frac{1}{2}EA\frac{\mathrm{d}\varphi}{\mathrm{d}x}\left(\frac{\mathrm{d}w_0}{\mathrm{d}x}\right)^3 + EI\frac{\mathrm{d}^2\varphi}{\mathrm{d}x^2}\frac{\mathrm{d}^2w_0}{\mathrm{d}x^2}\,\mathrm{d}x + \\ \quad + \left[EI\varphi\frac{\mathrm{d}^3w_0}{\mathrm{d}x^3} - EI\frac{\mathrm{d}\varphi}{\mathrm{d}x}\frac{\mathrm{d}^2w_0}{\mathrm{d}x^2} - \frac{1}{2}EA\varphi\left(\frac{\mathrm{d}w_0}{\mathrm{d}x}\right)^3\right]_{x_1}^{x_2} = \int_{x_1}^{x_2} \varphi p\,\mathrm{d}x \\ \\ \forall\varphi \in \Sigma(\Omega) \end{cases} \qquad \text{(See equation (A.10))}$$

Finally, neglecting membrane forces, the well-known linear Euler-Bernoulli beam equation is obtained (see equation (A.8)):

$$EI\frac{\partial^4 w_0}{\partial x^4} = \rho A\ddot{w}_0 + p \qquad \text{(see equation (A.8))}$$

With corresponding weak form:

$$\begin{cases} \text{Find } w_0 \in \Sigma(\Omega) = H^2(\Omega),\ \Omega = (x_1, x_2) \in \mathbb{R}^1 \text{ s.t.} \\ \\ \displaystyle\int_{x_1}^{x_2} -\varphi\rho A\ddot{w}_0 + EI\frac{\mathrm{d}^2\varphi}{\mathrm{d}x^2}\frac{\mathrm{d}^2w_0}{\mathrm{d}x^2}\,\mathrm{d}x + \left[EI\varphi\frac{\mathrm{d}^3w_0}{\mathrm{d}x^3} - EI\frac{\mathrm{d}\varphi}{\mathrm{d}x}\frac{\mathrm{d}^2w_0}{\mathrm{d}x^2}\right]_{x_1}^{x_2} = \int_{x_1}^{x_2} \varphi p\,\mathrm{d}x \\ \\ \forall\varphi \in \Sigma(\Omega) \end{cases} \qquad \text{(See equation (A.9))}$$

3.2 Fluid Model

As the floating solar membrane is located at sea, a fluid model should be coupled to the structural model. In this chapter, three fluid models are discussed, namely i) Ideal Flow; ii) Eulerian Flow; iii)

Stokes Flow; and iv) the Navier-Stokes equations. All models will be solved in a monolythical sense (see section 2.4), which means that the fluid formulations will be written in weak forms for IGA implementation. This chapter provides a brief background in all fluid models and gives their corresponding weak forms.

3.2.1 Navier-Stokes Equations

The Navier-Stokes equations are derived from the principle of mass conservation and the principle of conservation of momentum. Both laws are fundamental laws in continuum mechanics and hold for continua in general. This means that the equations for the beams and the plate derived in section 3.1 can also be derived via these equations. The main difference between solids and fluids from this perspective lies in the stress tensor, denoted by $\underline{\underline{\boldsymbol{\sigma}}}$.

The mass conservation law states that the amount of mass in a certain material volume $V(t)$ is constant over time. In integral form, this is denoted by:

$$\frac{\mathrm{d}}{\mathrm{d}t}\int_{V(t)} \rho(\boldsymbol{x},t)\,\mathrm{d}V = 0$$

When following the steps in [106], i.e. application of Gauß' rule and partial integration, the following differential form of the principle of mass conservation is obtained:

$$\frac{\partial \rho}{\partial t}(\boldsymbol{x},t) + \nabla\cdot(\rho(\boldsymbol{x},t)\boldsymbol{u}(\boldsymbol{x},t)) = 0,$$

To which is also referred as the continuity equation. Note that up to this point, no assumptions for the continuum 'being a fluid' are not made.

For constant density flows, where ρ is constant over the flow field, and for incompressible flows, where the density of particles does not change but where different particles might have different densities, the continuity equation reduces to the following:

$$\nabla\cdot\boldsymbol{u} = 0. \tag{3.12}$$

Similar to the principle of mass conservation, the principle of conservation of momentum can also be defined in integral form over a material volume $V(t)$. Hence, using Newton's second law, the following holds [106]:

$$\frac{\mathrm{d}}{\mathrm{d}t}\int_{V(t)} \rho(\boldsymbol{x},t)\boldsymbol{u}(\boldsymbol{x},t)\,\mathrm{d}V = \int_{V(t)} \rho(\boldsymbol{x},t)\boldsymbol{g}\,\mathrm{d}V + \int_{A(t)} \boldsymbol{f}(\boldsymbol{n},\boldsymbol{x},t)\,\mathrm{d}A$$

Where $\boldsymbol{g}$ and $\boldsymbol{f}$ are external forces working in the body $V(t)$ or at the boundary surface $A(t)$, respectively. Furthermore, the normal of the boundary is denoted by $\boldsymbol{n}$. Again, using the steps from [106], including partial integration, the following differential form of the momentum equation is derived:

$$\frac{\partial}{\partial t}(\rho\boldsymbol{u}) + \boldsymbol{u}\cdot\nabla\boldsymbol{u} = \rho\boldsymbol{g} + \nabla\cdot\underline{\underline{\boldsymbol{\sigma}}},$$

To which is referred to as the Cauchy momentum equation. Note that up to now, no assumptions about the fluid have been made hence this equation is valid for all continua. To obtain the Navier-Stokes momentum equation, the stress tensor is substituted. This is defined as:

$$\underline{\underline{\boldsymbol{\sigma}}} = -\underline{\underline{\boldsymbol{I}}}p + \underline{\underline{\boldsymbol{\tau}}}$$

Where the first term represents hydrostatic pressure and the last term represents the deviatoric stress tensor. For incompressible fluids, the deviatoric stress tensor further simplifies to:

$$\underline{\underline{\boldsymbol{\tau}}} = 2\mu\left(\nabla\boldsymbol{u} + (\nabla\boldsymbol{u})^T\right)$$

Where μ is the dynamic viscosity. Using this formulation, the momentum equation finally reduces to the Navier-Stokes momentum equation:

$$\rho\frac{\partial \boldsymbol{u}}{\partial t} + \rho\boldsymbol{u}\cdot\nabla\boldsymbol{u} = -\nabla p + \rho\boldsymbol{g} + \mu\nabla^2\boldsymbol{u}, \tag{3.13}$$

For constant density ρ.

3.2.1.1 Weak Form

The weak form of the Navier-Stokes equations will be derived by multiplying the momentum equation (see equation (3.13)) with a test function $\boldsymbol{\varphi} \in \mathbb{R}^{(3\times 1)}$ since the momentum equations are three-dimensional. Furthermore, the continuity equation (see equation (3.12)) is multiplied by the scalar test function q. Both equations are integrated over the domain Ω, resulting in the system:

$$\begin{cases} \displaystyle\int_\Omega \rho\boldsymbol{\varphi}\cdot\frac{\partial \boldsymbol{u}}{\partial t} + \rho\boldsymbol{\varphi}\cdot(\boldsymbol{u}\cdot\nabla)\boldsymbol{u}\,\mathrm{d}\Omega = \int_\Omega -\boldsymbol{\varphi}\cdot\nabla p + \rho\boldsymbol{\varphi}\cdot\boldsymbol{g} + \boldsymbol{\varphi}\nabla^2\boldsymbol{u}\,\mathrm{d}\Omega, \\ \displaystyle\int_\Omega q\nabla\cdot\boldsymbol{u}\,\mathrm{d}\Omega = 0. \end{cases}$$

The main interest now lies in the momentum equation. Namely, working out these expressions will show that the requirement on the function space is that it must contain first order derivatives. Hence, further simplification of the weak form of the continuity equation is not needed. Considering the momentum equation, using partial integration on the pressure statement (first term, right-hand side) and the viscous term (third term, right-hand side) gives:

$$\begin{aligned} \int_\Omega \rho\boldsymbol{\varphi}\cdot\frac{\partial \boldsymbol{u}}{\partial t} + \rho\boldsymbol{\varphi}\cdot(\boldsymbol{u}\cdot\nabla)\boldsymbol{u}\,\mathrm{d}\Omega &= \int_\Omega -\nabla\cdot(p\boldsymbol{\varphi}) + p\nabla\cdot\varphi + \mu\left(\nabla\cdot(\boldsymbol{\varphi}\cdot\nabla\boldsymbol{u})\right) - \nabla\boldsymbol{\varphi} : \nabla\boldsymbol{u}\,\mathrm{d}\Omega, \\ &= \int_\Omega p\nabla\cdot\boldsymbol{\varphi} - \mu\nabla\boldsymbol{\varphi} : \nabla\boldsymbol{u}\,\mathrm{d}\Omega + \int_{\partial\Omega} -p\boldsymbol{\varphi}\cdot\boldsymbol{n} + \mu\boldsymbol{\varphi}\cdot(\nabla\boldsymbol{u}\cdot\boldsymbol{n})\,\mathrm{d}\Gamma. \end{aligned}$$

Hence, the weak form becomes:

$$\begin{cases} \text{Find } (\boldsymbol{u}, p) \in \Sigma(\Omega) = (H^1(\Omega), L^2(\Omega)) \text{ s.t.} \\ \\ \displaystyle\int_\Omega \rho\boldsymbol{\varphi}\cdot\frac{\partial \boldsymbol{u}}{\partial t} + \rho\boldsymbol{\varphi}\cdot(\boldsymbol{u}\cdot\nabla)\boldsymbol{u}\,\mathrm{d}\Omega = \int_\Omega p\nabla\cdot\boldsymbol{\varphi} - \mu\nabla\boldsymbol{\varphi} : \nabla\boldsymbol{u}\,\mathrm{d}\Omega + \int_{\partial\Omega} -p\boldsymbol{\varphi}\cdot\boldsymbol{n} + \mu\boldsymbol{\varphi}\cdot(\nabla\boldsymbol{u}\cdot\boldsymbol{n})\,\mathrm{d}\Gamma, \\ \displaystyle\int_\Omega q\nabla\cdot\boldsymbol{u}\,\mathrm{d}\Omega = 0, \\ \\ \forall(\boldsymbol{\varphi}, q) \in \Sigma(\Omega). \end{cases} \tag{3.14}$$

In the literature, this weak formulation usually is the basis for flow models, see for instance papers [98],[107],[108],[109]

3.2.1.2 Isogeometric Discretisation

If this subsection will be relevant in further versions of the thesis, it will maybe be moved to another section in the report.

The isogeometric discretisation of the weak form of the Navier-Stokes equation (see equation (3.14)) is done similar to a finite element discretisation. Let $q = q_i$ and let $\boldsymbol{\varphi} = \boldsymbol{\varphi}_i$. Furthermore, let

$$p \approx \sum_{j=1}^{m} \beta_j q_j, \quad \text{and} \quad \boldsymbol{u} \approx \sum_{j=1}^{n} \boldsymbol{\alpha}_j \odot \boldsymbol{\varphi}_j.$$

Where $\odot$ defines element-wise multiplication, i.e. $\boldsymbol{a}_j \odot \boldsymbol{b}_j = a_j b_j \forall j$. With a little abuse of notation, but for the sake of brievety, this will be abbreviated by $\boldsymbol{a}_j \boldsymbol{b}_j$. Then, the discretised weak form becomes:

$$\begin{aligned}\sum_{j=1}^{n} \int_\Omega \rho \boldsymbol{\varphi}_i \cdot \frac{\partial (\boldsymbol{\alpha}_j \boldsymbol{\varphi}_j)}{\partial t} \,\mathrm{d}\Omega + \sum_{j=1}^{n} \int_\Omega \rho \boldsymbol{\varphi}_i \cdot (\boldsymbol{u} \cdot \nabla) \boldsymbol{\alpha}_j \boldsymbol{\varphi}_j \,\mathrm{d}\Omega = \sum_{j=1}^{m} \int_\Omega \beta_j q_j \nabla \cdot \boldsymbol{\varphi}_i \,\mathrm{d}\Omega - \sum_{j=1}^{n} \int_\Omega \mu \nabla \boldsymbol{\varphi}_i : \boldsymbol{\alpha}_j \nabla \boldsymbol{\varphi}_j \,\mathrm{d}\Omega + \\ - \sum_{j=1}^{m} \int_{\partial\Omega} \beta_j q_j \boldsymbol{\varphi}_i \cdot \boldsymbol{n} \,\mathrm{d}\Omega + \\ + \sum_{j=1}^{n} \int_{\partial\Omega} \mu \boldsymbol{\varphi}_i \cdot (\boldsymbol{\alpha}_j \nabla \boldsymbol{\varphi}_j \cdot \boldsymbol{n}) \,\mathrm{d}\Gamma, \quad \forall i = 1, \ldots, n, \\ \sum_{j=1}^{n} \int_\Omega q_i \nabla \cdot (\boldsymbol{\alpha}_j \boldsymbol{\varphi}_j) \,\mathrm{d}\Omega = 0, \quad \forall i = 1, \ldots, m,\end{aligned} \tag{3.15}$$

Here, the velocity field $\boldsymbol{u}$ is kept in the second term on the left-hand side because this term involves a non-linearity. From the discretised form in equation (3.15), the following matrices can be derived:

$$\begin{aligned} M_{ij} &= \int_\Omega \rho \boldsymbol{\varphi}_i \cdot \boldsymbol{\varphi}_j \,\mathrm{d}\Omega, \\ C_{ij}(\boldsymbol{u}) &= \int_\Omega \rho \boldsymbol{\varphi}_i \cdot (\boldsymbol{u} \cdot \nabla) \boldsymbol{\varphi}_j \,\mathrm{d}\Omega, \\ S_{ij} &= \int_\Omega \mu \nabla \boldsymbol{\varphi}_i : \nabla \boldsymbol{\varphi}_j \,\mathrm{d}\Omega, \\ L_{ij} &= \int_\Omega q_i \nabla \boldsymbol{\varphi}_j \,\mathrm{d}\Omega, \end{aligned}$$

Such that the discretised weak form from equation (3.15) simplifies to the following:

$$\begin{aligned} [\mathrm{M}\dot{\boldsymbol{u}} + \mathrm{C}(\boldsymbol{u}) + \mathrm{S}]\,\boldsymbol{\alpha} - \mathrm{L}^T \boldsymbol{\beta} &= \boldsymbol{0} \\ \mathrm{L}\boldsymbol{\alpha} &= \boldsymbol{0} \end{aligned} \tag{3.16}$$

Here, it is assumed that the boundary conditions are included in the system matrices. Furthermore, the ordering of the matrices and coefficient vector $\boldsymbol{\alpha}$ is chosen such that the dimensionality is right. For instance, one can choose to assemble the matrices such that

$$\boldsymbol{\alpha} = \begin{bmatrix} \alpha_1^1 \\ \vdots \\ \alpha_n^1 \\ \alpha_1^2 \\ \vdots \\ \alpha_n^2 \end{bmatrix} \quad \text{and} \quad \mathrm{M} = \begin{bmatrix} \mathrm{M}^1 & 0 \\ 0 & \mathrm{M}^2 \end{bmatrix} \quad \text{such that} \quad M_{ij}^1 = \int_\Omega \rho \varphi_i^1 \varphi_j^1 \,\mathrm{d}\Omega \quad \text{etc. for the other matrices}$$

Where α_j^1 is the first coefficient of the j^{th} basis function in the first dimension φ_j^1, and α_j^2 is the first coefficient of the j^{th} basis function in the second dimension φ_j^2.

3.2.2 Eulerian and Stokes Flow

Eulerian flow is in fact a simplification of the Navier-Stokes equations. The so-called Euler equations describe inviscid fluid flow. Hence, these equations are not valid in boundary layers or for low Reynolds numbers, as viscous effects dominate inertial effects in these cases. The Euler equations can easily be

derived from the Navier-Stokes equations by non-dimensionalisation using the Reynolds number [1]. This implies:

$$\begin{aligned} \frac{\partial}{\partial t}(\rho \boldsymbol{u}) + \boldsymbol{u} \cdot \nabla \boldsymbol{u} &= -\nabla p + \rho \boldsymbol{g}, \\ \nabla \cdot \boldsymbol{u} &= 0. \end{aligned} \tag{3.17}$$

Stokes flow is another simplification of the Navier-Stokes equations. Contrary to Eulerian flow, Stokes flow is applicable for low Reynolds numbers and hence describes viscid, laminar flow. The corresponding equations are:

$$\begin{aligned} -\nabla p + \rho \boldsymbol{g} + \mu \nabla^2 \boldsymbol{u} &= \boldsymbol{0}, \\ \nabla \cdot \boldsymbol{u} &= 0. \end{aligned} \tag{3.18}$$

3.2.3 Ideal Flow

Ideal flow is a flow description which assumes that the velocity field of the flow is derived from the velocity potential ϕ and that the flow is incompressible (see [111, 112] for reference). The former implies that the velocity field is equal to the gradient of the potential, i.e.

$$\boldsymbol{u} = \nabla \phi \tag{3.19}$$

And hence that the flow is irrotational by one fundamental law of vector calculus [113],

$$\nabla \times \boldsymbol{u} = \nabla \times \nabla \phi = 0. \tag{3.20}$$

Furthermore, the incompressibility condition implies that the continuity equation simplifies to (assuming constant pressure):

$$\nabla^2 \phi = 0.$$

Which is the governing equation for ideal flow. Once the velocity potential is known, the velocity field can be calculated from equation (3.19) which makes the model relatively simple. However, the downside of the potential flow assumption is that the irrotationaly of the flow shows that this theory is only applicable where vortices are not developed, away from boundaries and low Mach-number flows.

Using the (unsteady) Bernoulli equation [106][2], the pressures in the flow can be calculated. The (unsteady) Bernoulli equation is valid for constant-viscosity, irrotational, unsteady, constant-density flow. Furthermore, the equation is constant over an arbitrary streamline $\mathcal{S}$ in the flow. The unsteady Bernoulli equation reads:

$$\frac{\partial \phi}{\partial t} + \frac{1}{2}|\nabla \phi|^2 + gz + \frac{p_0}{\rho} = \text{constant along } \mathcal{S}. \tag{3.21}$$

Here, p_0 is an ambient pressure (e.g. atmospheric) and ρ is the density. Furthermore, the term gz incorporates the hydrostatic pressure in the system. The use of this equation together with equation (3.20) makes time-dependent problems possible to solve.

[1] An important note that should be made here is that the Euler equations were the predecessors of the Navier-Stokes equations and hence they were not derived from them [110]. So, the 'arrow of time' points in the wrong direction in this derivation. However, for the sake of simplicity and brievety, the derivation is performed in this order.

[2] The first version of the Bernoulli equation was published in 1738 by Daniel Bernoulli. However, the unsteady Bernoulli equation is extended by Euler in the 1750s. [114]

3.2.3.1 Weak Form

The weak form for ideal flow is in principle similar to the weak form of the Poisson equation; as equation (3.20) is a Poisson equation. This implies that the weak form of equation (3.20) is:

$$\begin{cases} \text{Find } \phi \in \Sigma(\Omega) = H^1(\Omega), \text{ s.t.} \\ \\ -\displaystyle\int_\Omega \nabla\varphi \cdot \nabla\phi \, \mathrm{d}\Omega + \int_{\partial\Omega} \varphi \nabla\phi \cdot \boldsymbol{n} \, \mathrm{d}\Gamma = 0 \\ \\ \forall\varphi \in \Sigma \end{cases} \tag{3.22}$$

The unsteady Bernoulli equation (see equation (3.21)) can be used to apply pressure on a coupled structure in order to obtain its deformations.

3.2.3.2 Isogeometric Discretisation

If this subsection will be relevant in further versions of the thesis, it will maybe be moved to another section in the report.

The isogeometric discretisation for the ideal flow problem is rather straightforward, as the weak form is rather straightforward. Let $\varphi = \varphi_i$ and approximate ϕ by a linear combination of basis functions, i.e.

$$\phi \approx \sum_{j=1}^{n} \alpha_j \varphi_j.$$

Then, the weak form becomes:

$$-\sum_{j=1}^{n} \int_\Omega \alpha_j \nabla\varphi_i \nabla\varphi_j \, \mathrm{d}\Omega + \sum_{j=1}^{n} \int_{\partial\Omega} \alpha_j \varphi_i \nabla\varphi_j \cdot \boldsymbol{n} \, \mathrm{d}\Gamma = 0,$$

Which can be written as a linear system:

$$\mathrm{A}\boldsymbol{\alpha} = \mathbf{0},$$

Where,

$$A_i j = \int_\Omega \alpha_j \nabla\varphi_i \nabla\varphi_j \, \mathrm{d}\Omega,$$

And where the boundary conditions are assembled in A in the right way. The boundary conditions for ideal flow are either a prescribed potential at the boundary (Dirichlet boundary condition) or a prescribed velocity (Neumann boundary condition).

3.2.4 Example: Flow around a Cylinder

This example shows the application of the isogeometric potential flow model on the flow around a sphere. For the ideal flow computation, the domain depicted in figure 3.2 is used. The domain is a quarter annulus fitted around the cylinder. Since the flow is irrotational and incompressible, it suffices to compute only the flow in a quarter annulus, using symmetry conditions. The total potential Φ is decomposed of a perturbation potential ϕ and an undisturbed flow field which in this case corresponds to uniform flow with velocity U_∞ in horizontal direction, i.e. $\Phi = \phi + U_\infty x$. The boundary value problem

that is solved for ϕ on the domain is:

$$\begin{aligned} \Delta\varphi &= 0 && \\ \text{s.t. } \phi &= 0 && \text{at } \partial\Omega_4 \\ \nabla\phi \cdot \boldsymbol{n} &= U_\infty && \text{at } \partial\Omega_1 \\ \nabla\phi \cdot \boldsymbol{n} &= 0 && \text{at } \partial\Omega_2 \\ \phi &= \frac{U_\infty R_1^2 x}{R_2^2} && \text{at } \partial\Omega_3 \end{aligned}$$

The inflow boundary condition results from an a-symmetry statement of the flow around the cylinder, subject to the vertical axis. The second boundary condition follows from the fact that the velocity of the flow should be zero to the normal of the cylinder and hence,

$$\nabla\Phi \cdot \boldsymbol{n} = \begin{bmatrix} \frac{\partial\Phi}{\partial x} \\ \frac{\partial\Phi}{\partial y} \end{bmatrix} = \begin{bmatrix} U_\infty + \frac{\partial\phi}{\partial x} \\ \frac{\partial\phi}{\partial y} \end{bmatrix} \implies \nabla\phi \cdot \boldsymbol{n} = -U_\infty n_x$$

The third boundary condition follows from symmetry of streamlines over the horizontal axis, hence the velocity 'through' the axis is zero. The last boundary condition follows from the fact that the total potential is prescribed at the boundary and hence,

$$\Phi = \frac{U_\infty (R_1^2 + R_2^2) x}{R_2^2} \implies \phi = \Phi - U_\infty x = \frac{U_\infty R_1^2 x}{R_2^2}$$

Which is a Dirichlet boundary condition for ϕ. The analytical solution of this problem can be derived from [106, p.294] and reads:

$$\frac{U_\infty R_1^2 x}{x^2 + y^2}$$

The results for the computation are depicted in figure 3.3 and the convergence of the L_2 error for several mesh refinements is depicted in figure 3.4. Results are obtained using `G+smo`[115][3]

3.3 Mathematical Preliminaries

[3] The Geometry + Simulation module is an open-source `C++` library "that brings together mathematical tools for geometric design and numerical simulation. (..) It implements the relatively new paradigm of isogeometric analysis, which suggests the use of a unified framework in the design and analysis pipeline". More information can be found on https://github.com/gismo/gismo/wiki.

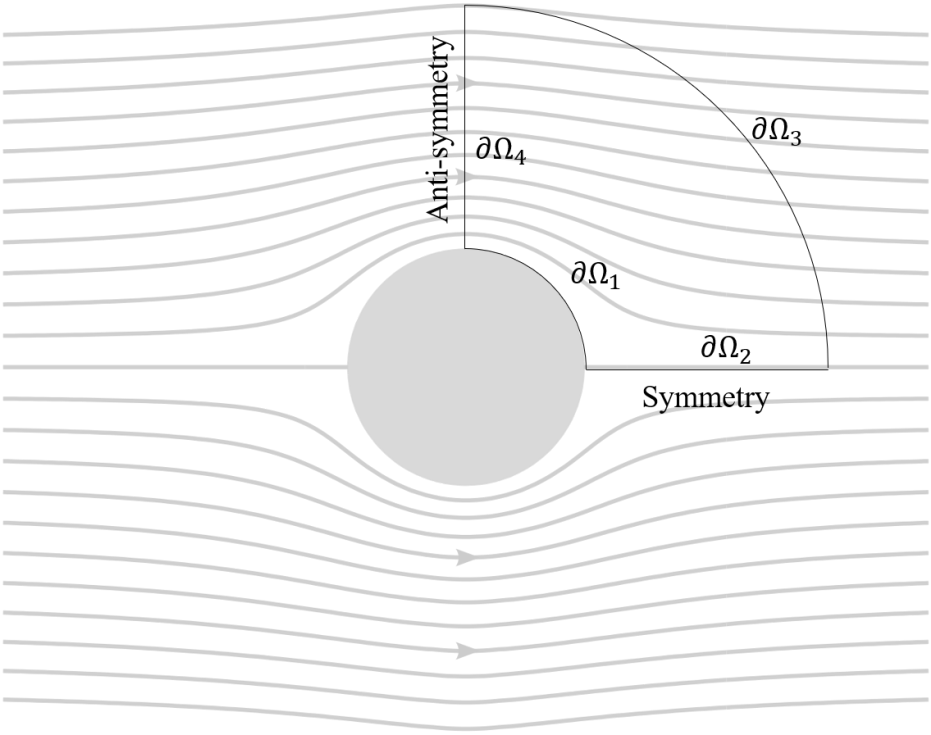

Figure 3.2: Domain for ideal flow around a sphere. The radius of the sphere is 1 and the outer radius of the domain is 5.

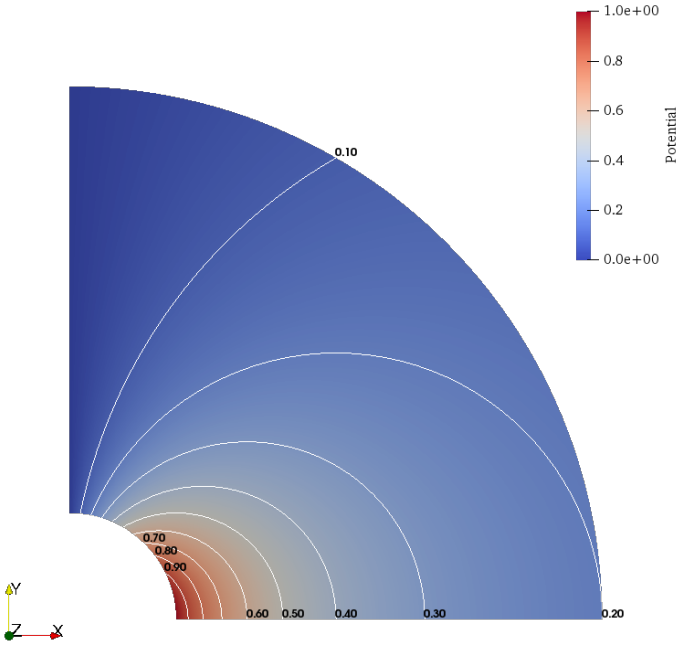

(a)

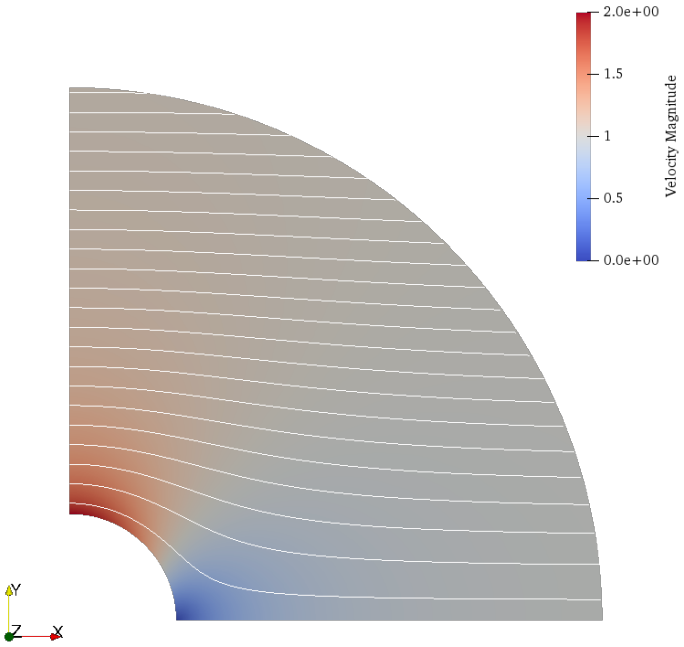

(b)

Figure 3.3: (Figure continues on next page)

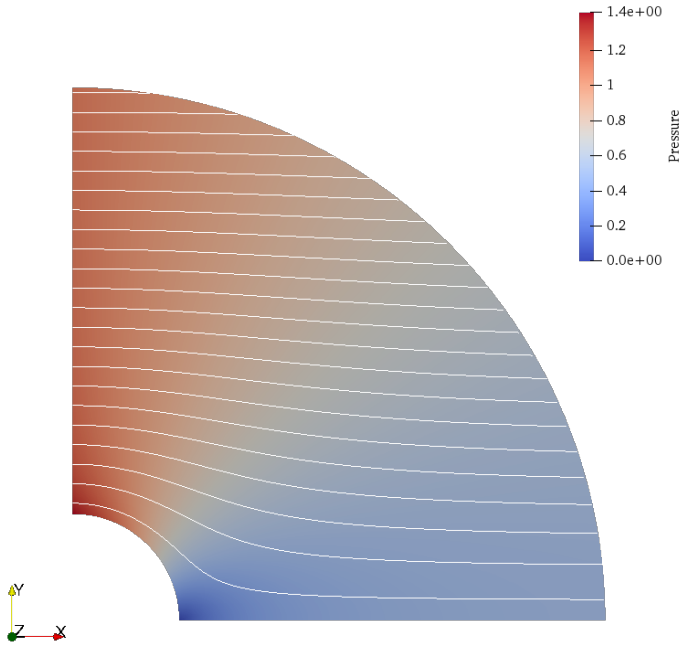

(c)

Figure 3.3: Results for the ideal flow computation around a sphere. On top is the perturbation potential ϕ, in the middle is the magnitude of the velocity including stream lines and at the bottom is the pressure according to equation (3.21).

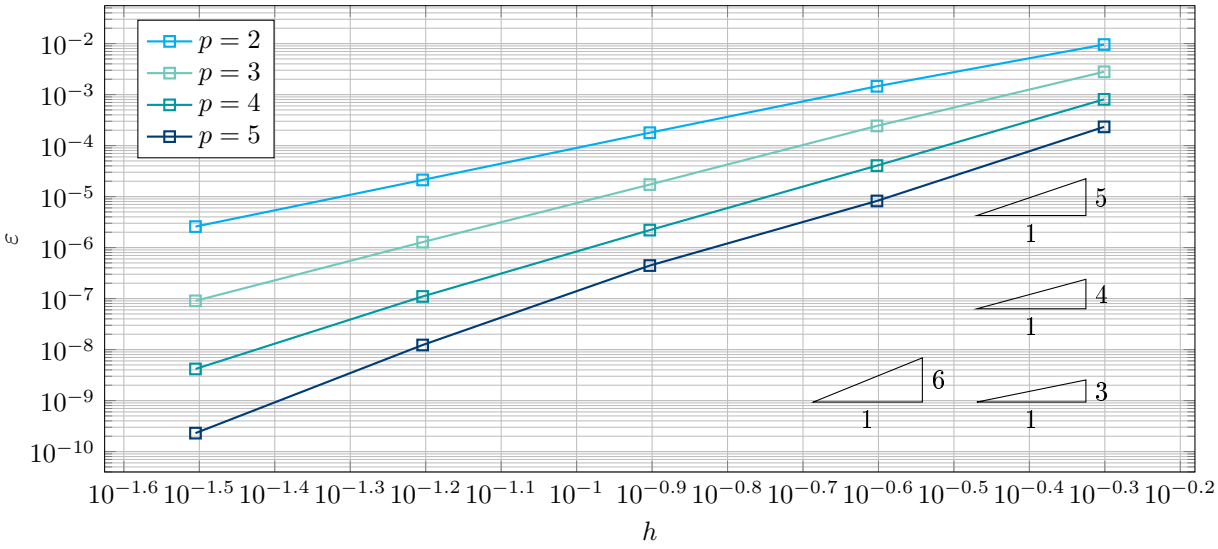

Figure 3.4: L_2-norm of potential flow around a cylinder for different orders of basis functions ($p = 2 \dots 5$) subject and refinement levels with respect to the initial mesh.

4 | Basics of Isogeometric Analysis

This section covers the basics of Isogeometric Analysis. That is, section 4.1 gives an overview of Isogeometric Analysis. This section starts with defining B-splines and NURBS. Thereafter, the analysis framework for solving differential equations, which is similar to Finite Element Analysis (FEA) is discussed. In order to illustrate the simple concepts of Isogeometric Analysis, **??** *treats discretisation of the Poisson equation with B-spline of various orders and with various knot vectors.*

4.1 Overview

Isogeometric Analysis is a type of analysis that was firstly introduced by Hughes et al. and that is most familiar to Finite Element Analysis (FEA) compared to the Finite Difference Method or the Finite Volume Method. The reader is refered to section 2.3.3 for a literature review on the differences between IGA and FEA. The main motivation for the use of Isogeometric Analysis was the integration of CAD and Finite Element Analysis, since CAD uses B-splines or NURBS for geometry definition and Isogeometric Analysis uses them for calculation. The main difference with respect to FEA is that the basis functions, i.e. the splines, that are used for analysis have a support that is not restricted to elements. In this way, literature often refers to *patches* instead of elements, whereby multiple basis functions can work on one patch. A more detailed explanation of patches and elements can be found in [53, Ch. 3.5].

The driving philosophy of IGA is, as mentioned in the previous paragraph, based on seamless integration between CAD and FEA. As will be shown in the remainder of this chapter, geometries can be constructed using a series of control points (i.e. a *control net*) and NURBS, B-spline or similar basis functions. As will be clear from equation (4.4), the mathematical formulations for surfaces and volumes (but also for lines), can be represented by parametric coordinates. Hence, the idea behind IGA is to use the parametric basis (usually denoted by *knot vectors* with knots ξ, η, ζ) from the geometry description (in any dimension) for analysis of physical Partial Differential Equations (PDEs) working on the geometry. The geometry descriptions in equation (4.4) can then be seen as so-called *geometrical mappings* and the field of differential geometry (see chapter B) can be used to do numerical analyses of the PDEs on the parametric domain and compute the solution on the domain using the mappings from equation (4.4)

4.1.1 B-splines and NURBS

By the time of the introduction of IGA, in 2005, the basis functions were B-splines or NURBS. Later on, T-splines and other splines that were developed in the CAD community (e.g. [76]) were also used as basis for IGA ([75]).

B-splines are curves that are defined by so-called knot vectors that are described by knot vectors. A knot vector is a non-decreasing sequence of coordinates in the parameter space. Thus, $\Xi = \{\xi_1, \xi_2, \ldots, \xi_{n+p+1}\}$ where $\xi_i \geq \xi_j$ for $i > j$ and $\xi_k \in \mathbb{R}$ for all k. Here, n is the number of basis functions and p is the degree of the basis functions that construct the B-spline.

Construction of B-splines is done recursively. Let $N_{i,p}$ denote the i^{th} basis function of order p. The

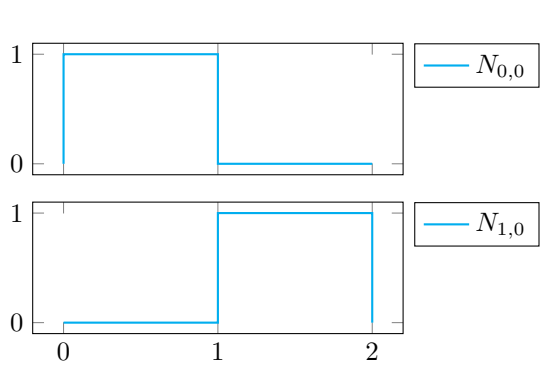

(a) Zeroth order basis functions with knot vector $\Xi = \{0, 1, 2\}$

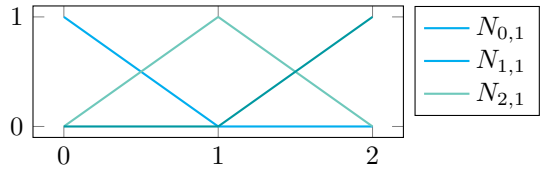

(b) First order basis functions with knot vector $\Xi = \{0, 0, 1, 2, 2\}$

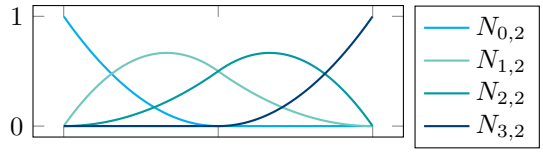

(c) Second order basis functions with knot vector $\Xi = \{0, 0, 0, 1, 2, 2, 2\}$

Figure 4.1: Examples of basis functions of different order and the same *unique* knots. As the order increases, the end knots are repeated $p + 1$ times. Furthermore, these examples also illustrate that the number of basis functions increases as the order increases.

0^{th} order basis function in general coordinate ξ is defined by:

$$N_{i,0}(\xi) = \begin{cases} 1 & \text{if } \xi_i \leq \xi < \xi_{i+1} \\ 0 & \text{elsewhere} \end{cases}$$

Now, the higher-degree basis functions ($p \geq 1$) are constructed with the Cox-De Boor recursion formula [116, 117]:

$$N_{i,p} = \frac{\xi - \xi_i}{\xi_{i+p} - \xi_i} N_{i,p-1}(\xi) + \frac{\xi - \xi_{i+1}}{\xi_{i+p+1} - \xi_{i+1}} N_{i+1,p-1}(\xi)$$

For repeated indices, so in case $\xi_i = \xi_{i+1}$, then the basis function is defined to be zero everywhere. Additionally, the Cox-De Boor formula needs an assumption for the case that $\frac{0}{0}$, which is assumed to be equal to zero for the construction of the basis function. Hence, one can see that all basis functions are zero between two identical indices.

The derivatives of the basis function N_i are determined in the following way:

$$\frac{\mathrm{d}}{\mathrm{d}\xi} N_{i,p}(\xi) = \frac{p}{\xi_{i+p} - \xi_i} N_{i,p-1}(\xi) - \frac{p}{\xi_{i+p+1} - \xi_{i+1}} N_{i+1,p-1}(\xi)$$

And obtaining higher-order derivatives iteratively by taking the derivative of this expression:

$$\frac{\mathrm{d}^k}{\mathrm{d}\xi^k} N_{i,p}(\xi) = \frac{p}{\xi_{i+p} - \xi_i} \left(\frac{\mathrm{d}^{k-1}}{\mathrm{d}\xi^{k-1}} N_{i,p-1}(\xi) \right) - \frac{p}{\xi_{i+p+1} - \xi_{i+1}} \left(\frac{\mathrm{d}^{k-1}}{\mathrm{d}\xi^{k-1}} N_{i+1,p-1}(\xi) \right)$$

As an extension for B-splines, Non-Uniform Rational B-splines are constructed by adding a weight for each basis function. Then, the weighting function $W(\xi)$ is defined by:

$$W = \sum_{i=1}^{n} N_{i,p}(\xi) w_i \tag{4.1}$$

Where w_i is the weight for spline $N_{i,p}$ of order p. Then, the i^{th} NURBS of order p is defined by:

$$R_i^p = \frac{N_{i,p}(\xi) w_i}{W(\xi)} \tag{4.2}$$

By introducing a weight per basis function, one is able to represent each geometry accurately.

In order to generate spline curves in 2D or 3D, the basis functions N_i based on one or more knot vectors $\Xi, \mathcal{H}$ can be utilised. Define a curve l in 2D and let $\boldsymbol{S}_i$ be control points in the 2D plane. Then, the curve is constructed by:

$$\boldsymbol{C}(\xi) = \sum_{i=1}^{n} R_i^p(\xi)\boldsymbol{B}_i \tag{4.3}$$

Where R_i^p can also be a B-spline if all weights are equal. Furthermore, $\boldsymbol{B}_i$ contains the coordinates of a control point in 2 or 3 dimensions. Furthermore, for the generation of surfaces, or volumes, the parametric domain $\xi \in \mathbb{R}^1$ is extended to $(\xi, \eta) \in \mathbb{R}^2$ or $(\xi, \eta, \zeta) \in \mathbb{R}^3$. The formulations for surfaces and solids are then:

$$\begin{aligned} \boldsymbol{S}(\xi, \eta) &= \sum_{i=1}^{n}\sum_{j=1}^{m} R_i^p(\xi)P_j^q(\eta)\boldsymbol{B}_{i,j} \\ \boldsymbol{V}(\xi, \eta, \zeta) &= \sum_{i=1}^{n}\sum_{j=1}^{m}\sum_{k=1}^{l} R_i^p(\xi)P_j^q(\eta)T_k^r(\zeta)\boldsymbol{B}_{i,j,k} \end{aligned} \tag{4.4}$$

Where R_i^p, P_j^q and T_k^r are NURBS of orders p, q and r. Furthermore, with preservation of the exact geometry, it is possible to insert a control point of a curve (or surface or volumes) for refinement purposes. This is called knot insertion. The principle of knot insertion is based on redefining the control points such that one is added but that the geometry remains the same. Let $\bar{\boldsymbol{B}}$ be the vector of new control points and let $\bar{\boldsymbol{B}}$ be the old control points and let the new knot $\bar{\xi}$ be added between ξ_k and ξ_{k+1}. Then, the new control points are determined by:

$$\bar{B}_i = \alpha_i B_i + (1 - \alpha_i)B_{i-1}$$

With

$$\alpha_i = \begin{cases} 1, & 1 \leq i \leq k-1 \\ \dfrac{\bar{\xi} - \xi_i}{\xi_{i+p} - \xi_i}, & k-p+1 \leq i \leq k \\ 0, & k+1 \leq i \leq n+p+2 \end{cases}$$

Lastly, order elevation of B-splines is performed by increasing the multiplicity of *each* knot without adding new knot values. In this way, the original basis functions are increased by order. When knot insertion is followed by order elevation, the equivalence of a p-refinement in FEA is constructed. In this way, the basis of the basis functions does not increase, but their order does. When order elevation is followed by knot insertion the so-called k refinement is constructed, in which continuity of basis function on internal knots can be increased.

4.1.2 Isogeometric Analysis

As mentioned before, Isogeometric Analysis is similar to Finite Element Analysis. Basically, Isogeometric Analysis utilises spline basis functions that have a global support. Hence, discretisation according to the Isogeometric Analysis framework is done in a similar way compared to FEA. Firstly, given a PDE (or a system of PDEs), the weak form is determined by multiplying the PDE by a test function and integrating it over the domain. Partial integration is applied to incorporate boundary conditions. Up to this point, there is no difference with classical FEA. Secondly, when the weak form is known, the solution is approximated by a finite number of the product of a basis function and a weight. Here, in terms of the basis functions, differences come into play.

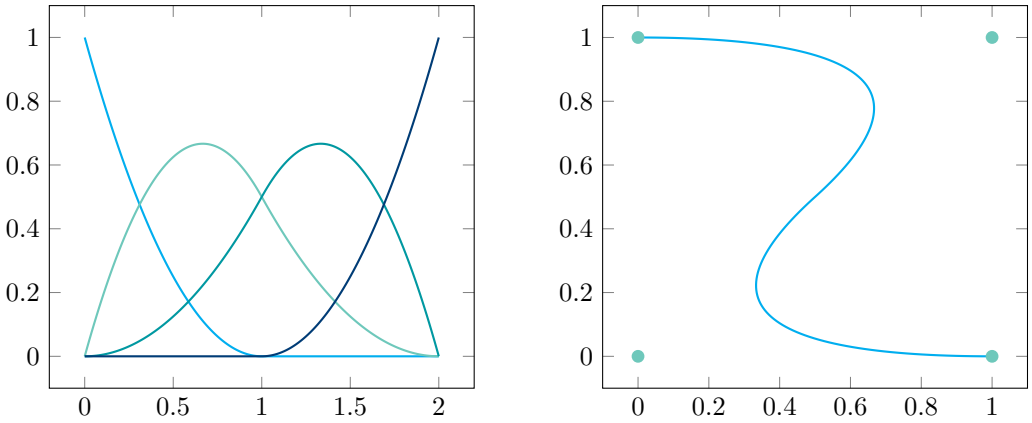

(a) (b)

Figure 4.2

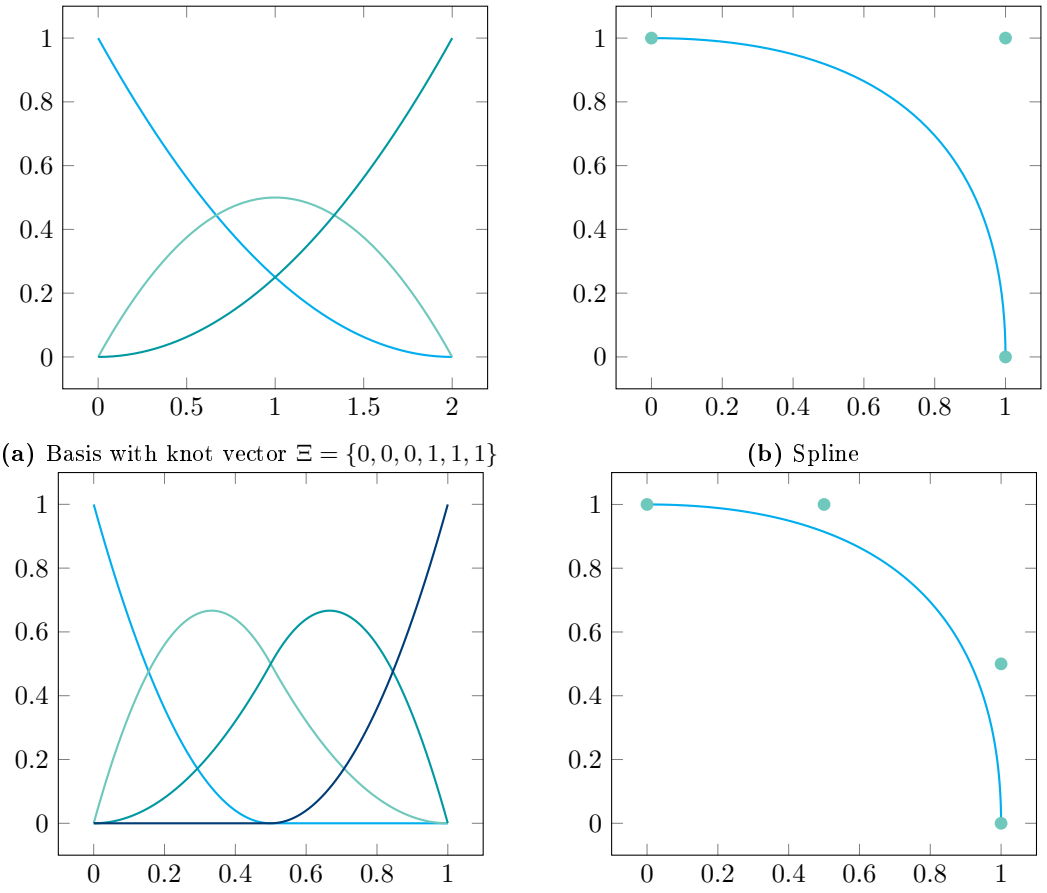

(a) Basis with knot vector $\Xi = \{0, 0, 0, 1, 1, 1\}$

(b) Spline

(c) Basis with knot vector $\Xi = \{0, 0, 0, 0.5, 1, 1, 1\}$

(d) B-spline

Figure 4.3: Principle of knot insertion. On top, a B-spline of order 2 with three basis functions for the knot vector $\Xi = \{0, 0, 0, 1, 1, 1\}$ is presented. On the bottom, a B-spline of order 2 with four basis functions and modified knot vector $\Xi = \{0, 0, 0, 0.5, 1, 1, 1\}$ is presented. Knot insertion moves the control point such that the B-spline remains the same.

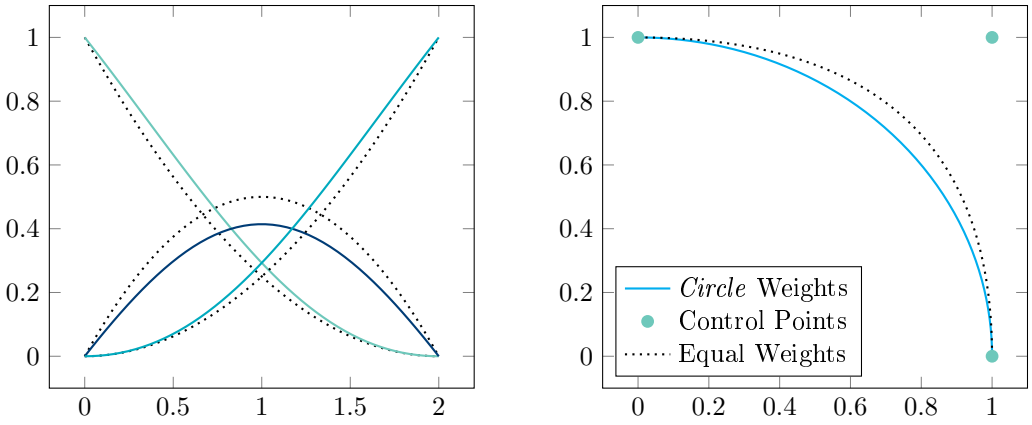

Figure 4.4: NURBS (weights $\{1, 1/\sqrt{2}, 1\}$) curve versus B-spline. On the left, the basis functions of the B-spline curve are dotted and the basis functions of the NURBS are coloured. On the right, the B-spline is dotted and the NURBS curve is coloured. With these weights, the NURBS exactly represents a quarter of a circle. [118]

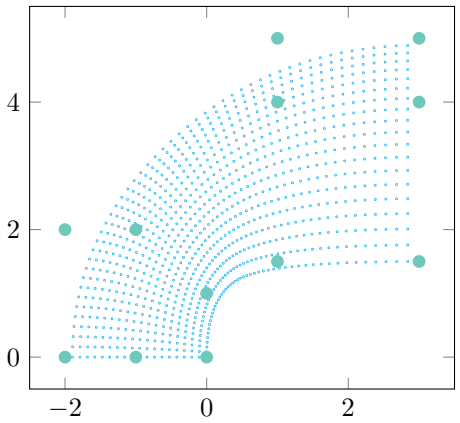

Figure 4.5: Surface generated with the control points as shown in the figure and with knot vectors $\Xi = \{0, 0, 0, 0.5, 1, 1, 1\}$ (horizontal, see figure 4.3c) and $\mathcal{H} = \{0, 0, 0, 1, 1, 1\}$ (vertical, see figure 4.3a).

Given a weak form, denote by the following combination of a bi-linear operator $a(\cdot,\cdot)$ and an inner product $(\cdot,\cdot)$,

$$a(u,\varphi) = (\varphi, f)$$

Where φ is the basis function, u is the solution and f is the forcing term of the PDE. Using the Galerkin approximation

$$u = \sum_{j=1}^{\infty} \alpha_j \varphi_j \approx \sum_{j=1}^{n} \alpha_j \varphi_j,$$

And substituting $\varphi = \varphi_i$, the weak form changes to (given linearity of $a(\cdot,\cdot)$):

$$\sum_{j=1}^{n} \alpha_j a(\varphi_j, \varphi_i) = (\varphi_i, f), \forall i$$

In case of classical FEA, the integrals in $a(\cdot,\cdot)$ and in the inner product can be simplified to band matrices, since the basis functions have a local support. When B-splines or NURBS are used as basis functions, this simplification cannot be made. Hence, the system to be solved cannot be simplified further and domain integrals have to be calculated for all combinations of basis functions φ_i, φ_j.

In sequel, an example of Isogeometric Analysis is given for the linear Euler beam equation. Here, the discretisation procedure using B-splines is briefly explained, but it can be found in more detail in section 5.1.

4.2 An Example: Clamped-Clamped Linear Euler Beam

Let us consider a linear Euler-Bernoulli beam with length 1, which is clamped at both ends and which is subject to a uniform pressure load $q = -1\, N/m$. As we have seen in section 3.1.5, equation (A.8), the governing equation for a linear beam is (see section 5.1 for boundary conditions):

$$EI\frac{\partial^4 w}{\partial x^4} = q$$
$$w(0) = \frac{\mathrm{d}w}{\mathrm{d}x}(0) = w(1) = \frac{\mathrm{d}w}{\mathrm{d}x}(1) = 0$$

The weak form is, using equation (A.9):

$$\begin{cases} \text{Find } w \in \Sigma(\Omega) = \left\{ w \in H^2(\Omega) | w(0) = \dfrac{\mathrm{d}w}{\mathrm{d}x}(0) = w(1) = \dfrac{\mathrm{d}w}{\mathrm{d}x}(1) = 0 \right\}, \Omega = (0,1) \in \mathbb{R}^1 \text{ s.t.} \\ \\ \displaystyle\int_0^1 EI \frac{\mathrm{d}^2\varphi}{\mathrm{d}x^2}\frac{\mathrm{d}^2 w}{\mathrm{d}x^2}\,\mathrm{d}x = \int_0^1 \varphi q\,\mathrm{d}x \\ \\ \forall \varphi \in \Sigma(\Omega) \end{cases}$$

(See equation (A.9))

Here, the boundary terms drop out because the clamped boundary conditions are essential boundary conditions. The spatial discretisation, which is also treated in section 5.1, is done by the Galerkin method. Here, it is assumed that the solution w can be approximated by the following:

$$u(x) = \sum_{j=1}^{\infty} c_j N_j(x) \approx \sum_{j=1}^{n} c_j N_j(x)$$

With c_j, $j = 1, \ldots, n$ unknown constants. Substituting this into the obtained weak formulation gives a linear system (see section 5.1 for the details):

$$\mathrm{K}\boldsymbol{c} = \boldsymbol{f},$$

Where,

$$\begin{aligned} K_{ij} &= \int_0^1 EI \frac{\mathrm{d}^2\varphi_i}{\mathrm{d}x^2} \frac{\mathrm{d}^2\varphi_j}{\mathrm{d}x^2} \,\mathrm{d}x, \\ f_i &= \int_0^1 \varphi_i p \,\mathrm{d}x, \\ \boldsymbol{c} &= \begin{bmatrix} c_1 & c_2 & \ldots & c_n \end{bmatrix}^T. \end{aligned}$$

Using this linear system, the coefficients $\boldsymbol{c}$ can be calculated and an approximation of the solution u_n can be constructed using the Galerkin method. In figure 4.6 and figure 4.7, the basis functions and their decomposition to the solution of the problem, respectively, are presented. As seen in these figures, the second order basis functions clearly deviate from the analytical solution and since the analytical solution is a fourth order polynomial, the basis functions of fourth order always represent the exact solution. Another observation that can be made is that the basis functions are indeed global, which is a property of the IGA framework. Since they have this global support, the basis functions that overlap with others do not have the property that they represent the solution on nodes, as we know from basic Finite Element Methods.

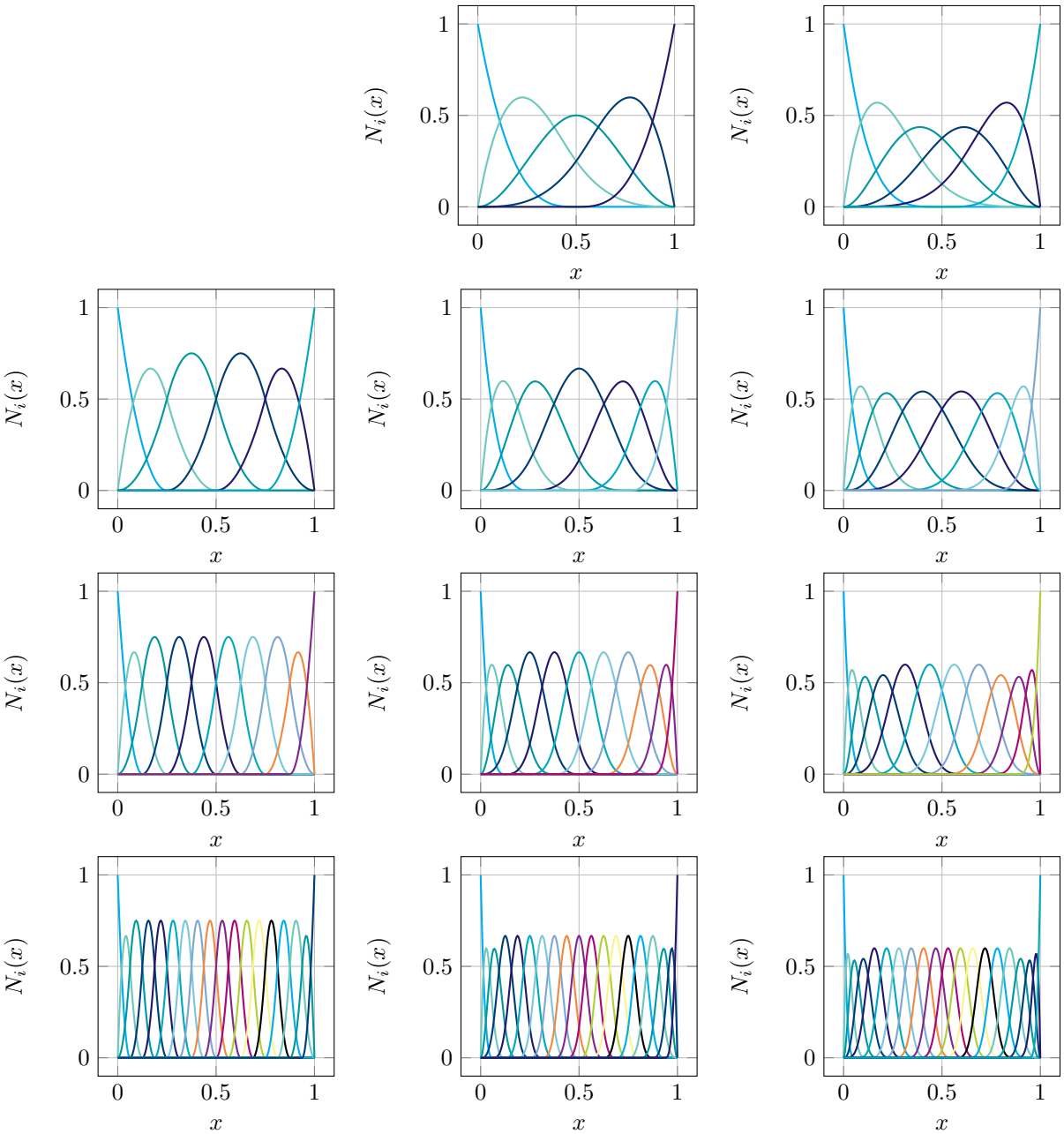

Figure 4.6: Basis functions of ordder p 2 (left), 3 (mid) and 4 (right) for knot vectors $\Xi = \{0.0, 1.0\}$ (top), $\Xi = \{0.0, 0.5, 1.0\}$ (mid top), $\Xi = \{0.0, 0.25, 0.5, 0.75, 1.0\}$ (mid bottom) and $\Xi = \{0.0, 0.125, 0.25, 0.375, 0.5, 0.625, 0.75, 0.875, 1.0\}$ (bottom). **note:** unique the first and last knots are repeated $p + 1$ times.

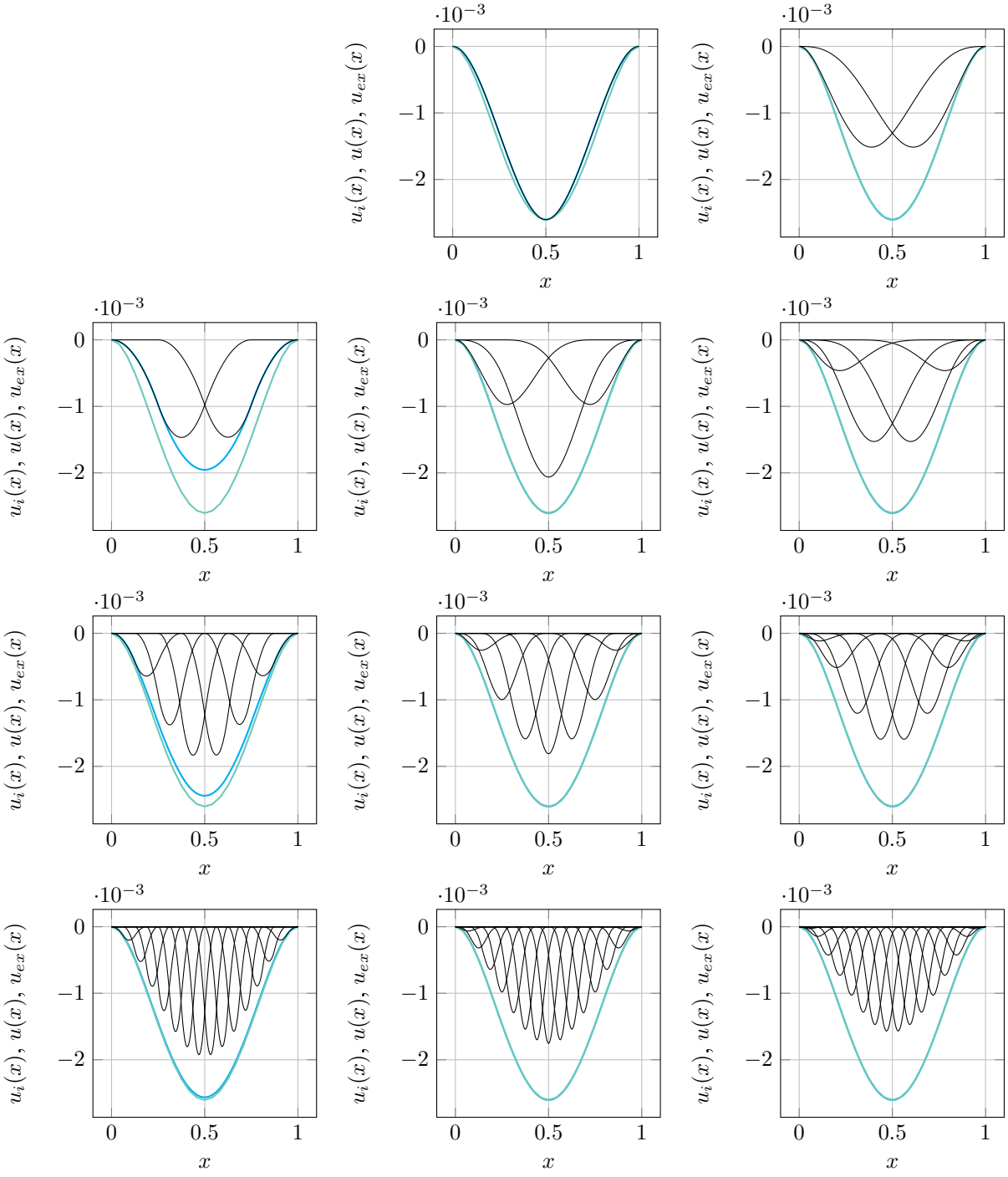

Figure 4.7: Analytical solution (sea green), numerical solution (cyan) and decomposition of the solution (black) for basis function of order p 2 (left), 3 (mid) and 4 (right) for knot vectors $\Xi = \{0.0, 1.0\}$ (top), $\Xi = \{0.0, 0.5, 1.0\}$ (mid top), $\Xi = \{0.0, 0.25, 0.5, 0.75, 1.0\}$ (mid bottom) and $\Xi = \{0.0, 0.125, 0.25, 0.375, 0.5, 0.625, 0.75, 0.875, 1.0\}$ (bottom).

5 | Isogeometric Euler-Bernoulli Beam Models

In this chapter, the spatial and temporal discretisation of Euler-Bernoulli beams are discussed. Using different benchmark cases, the beam model is verified and theoretical orders of convergence in both space and time are evaluated. Furthermore, a curvilinear beam model is presented and verified as well. The governing equations for this model are slightly different and require basic Differential Geometry. The latter is given for the reader in chapter B. Throughout the whole chapter, references to section 3.1 and chapter 4 are made.

5.1 Spatial Discretisation

5.1.1 Linear Euler-Bernoulli Beam

Equation (A.9) presents the weak formulation for the linear Euler-Bernoulli beam formulation. Derivation of the isogeometric model for this equation is similar to the derivation of a FEM model and an example was given in section 4.2. For this equation, the solution is approximated by a finite number of weighted basis functions, i.e.

$$w_0(x,t) = \sum_{j=1}^{\infty} c_j(t)\varphi_j(x) \approx \sum_{j=1}^{n} c_j(t)\varphi_j(x)$$

Here, $c_j(t)$ represents the weight of the basis function $\varphi_j(x)$. Furthermore, the basis functions $\varphi_j(x)$ are from a function space $\Sigma(\Omega)$, $x \in \Omega$. Substituting this approximation in the weak form, letting $\varphi = \varphi_i \quad \forall i = 1, \ldots, n$ and omitting the notations (t) and (x) gives:

$$\sum_{j=1}^{n} \left\{ \int_{x_1}^{x_2} -\ddot{c}_j \varphi_i \rho A \varphi_j + EI c_j \frac{\mathrm{d}^2\varphi_i}{\mathrm{d}x^2}\frac{\mathrm{d}^2\varphi_j}{\mathrm{d}x^2}\,\mathrm{d}x + c_j \left[EI\varphi_i \frac{\mathrm{d}^3\varphi_j}{\mathrm{d}x^3} - EI\frac{\mathrm{d}\varphi_i}{\mathrm{d}x}\frac{\mathrm{d}^2\varphi_j}{\mathrm{d}x^2} \right]_{x_1}^{x_2} \right\} = \int_{x_1}^{x_2} \varphi_i p\,\mathrm{d}x \quad \forall i = 1, \ldots, n \tag{5.1}$$

Here, the coordinates x_1 and x_2 can be chosen arbitrarily and without loss of generality they are chosen here as $x_1 = 0$ and $x_2 = 1$. This means that the considered beam has length 1. The boundary term in the formulation above is

$$c_j \left[\underbrace{EI\varphi_i \frac{\mathrm{d}^3\varphi_j}{\mathrm{d}x^3}}_{\text{BC I.1}} - \underbrace{EI\frac{\mathrm{d}\varphi_i}{\mathrm{d}x}\frac{\mathrm{d}^2\varphi_j}{\mathrm{d}x^2}}_{\text{BC I.2}} \right]_{x_1}^{x_2}, \tag{5.2}$$

and is decomposed of two terms, which are referenced by BC I.1 and BCI.2, respectively. The choice of the space for the basis functions is depending on the physical boundary conditions of the beam. For

Table 5.1: Physical beam boundary conditions and the implementation of the quantities Displacement, Rotation, Moment and Force. For each boundary condition, combinations of {Displacement, Rotation} and {Force, Moment} are prescribed. The notation $\neq 0$ denotes an inhomogeneous term.

Boundary Condition	Prescribed	Unknown
Clamped	Displacement, Rotation	Force, Moment
Pinned	Displacement, Moment	Rotation, Force
Rolled, Vertically	Rotation, Force	Displacement, Moment
Free end	Force, Moment	Displacement, Rotation
Force + clamped	Force ($\neq 0$), Rotation	Displacement, Moment
Force + free	Force ($\neq 0$), Moment	Displacement, Rotation
Moment + pinned	Displacement, Moment ($\neq 0$)	Rotation, Force
Moment + free	Force, Moment ($\neq 0$)	Displacement, Rotation

implementation of the boundary conditions, prescribed displacements, rotations, forces and moments can be applied on a beam end $x_i, i = 1, 2$:

Prescribed displacement If a displacement is prescribed on the beam end, BC I.1 is relevant. As seen in this term, the boundary condition is essential and hence it should be incorporated by a restriction on the basis function space Σ. For example, a homogeneous boundary displacement, i.e. $w(x_i) = 0$, the basis should be homogeneous and hence $\varphi_k(x_i)$ should be zero for all k.

Prescribed rotation For a prescribed rotation on the beam end, BC I.2 is relevant. In this term, the derivative of the basis function, $\frac{\mathrm{d}^2\varphi_j}{\mathrm{d}x^2}$, shows that a prescribed rotation on the beam end x_i is likewise an essential boundary condition. Similar to a prescribed displacement, this boundary condition is incorporated by adding a restriction to the function space Σ.

Prescribed force If a vertical force is prescribed on the boundary point x_i, BC I.1 is relevant because $c_j EI \frac{\mathrm{d}^3\varphi_j}{\mathrm{d}x^3}$ denotes the shear force in the beam. Hence, prescribing this force on beam end x_i requires this natural boundary contribution to be shifted to the right-hand side in the system resulting from the Galerkin discretisation.

Prescribed moment Similarly to the prescribed vertical force, a prescribed moment resulting from $c_j EI \frac{\mathrm{d}^2\varphi_j}{\mathrm{d}x^2}$ in BCI.2 is also a natural boundary condition and hence it can be included by moving the specific term to the right-hand-side of the assembled linear system resulting from the Galerkin discretisation.

Based on these four prescribed mathematical boundary conditions, sets of physical boundary conditions can be defined for the beam equations. These are listed in table 5.1. Note that in any case, a quantity of both {Force,Displacement} and {Moment,Rotation} is prescribed. This is because only in these cases, both contributions in the boundary term vanish.

For different combinations of boundary conditions, analytical solutions are available for the linear Euler-Bernoulli beam. For the choice of the basis functions, the boundary conditions are of great importance. Namely, the basis functions φ_j that are used for the approximation of the solution have to fullful the same boundary conditions as imposed on the problem. Hence, referring back to equation (A.9), the function space in which the solution w_0 and the test function φ_i are 'living in' must be respecified according to the boundary conditions. For example, suppose we have a beam with clamped at $x = 0$ and free at $x = L$, then $w_0, \varphi \in \Sigma(\Omega) = \left\{w \in H^1(\Omega) : w(0) = \frac{\mathrm{d}w}{\mathrm{d}x}(0) = 0\right\}$.

Finally, for a beam model with certain boundary conditions, the discretised linear beam equation from equation (5.1) can be evaluated for all $\varphi_j \in \Sigma(\Omega), j = 1, ..., n$. This results in the following system

of equations:

$$-\mathrm{M}\ddot{\boldsymbol{c}} + \mathrm{K}\boldsymbol{c} = \boldsymbol{f}, \tag{5.3}$$

Where,

$$\begin{aligned}
M_{ij} &= \int_0^1 \rho A \varphi_i \varphi_j \,\mathrm{d}x, \\
K_{ij} &= \int_0^1 EI \frac{\mathrm{d}^2\varphi_i}{\mathrm{d}x^2}\frac{\mathrm{d}^2\varphi_j}{\mathrm{d}x^2} \,\mathrm{d}x, \\
f_i &= \int_0^1 \varphi_i p \,\mathrm{d}x, \\
\ddot{\boldsymbol{c}} &= \begin{bmatrix}\ddot{c}_1 & \ddot{c}_2 & \dots & \ddot{c}_n\end{bmatrix}^T, \\
\boldsymbol{c} &= \begin{bmatrix}c_1 & c_2 & \dots & c_n\end{bmatrix}^T.
\end{aligned}$$

5.1.2 Curvilinear Beam

The result that has been derived in the previous sections is valid for straight beams, i.e. beams with an inifinite radius of curvature. To calculate the displacements of a beam with finite radius of curvature, extra terms are added to the equation and the formulation has to be solved in a curvilinear coordinate system. The former will be discussed in this section using the works of Lim et al.[119] and Qatu[120], whereas the latter is discussed in chapter B.

Let t denote the thickness of the beam and $R(s)$ the radius of curvature depending on a curvelinear coordinate s. For a thin curved beam, i.e. a beam where $R \gg t$, the normal strain ε_1 and the curvature change κ_1 are given by:

$$\begin{aligned}
\varepsilon_1^* &= \frac{\mathrm{d}u}{\mathrm{d}s} + \frac{w}{R} \\
\kappa_1^* &= -\frac{\mathrm{d}^2 w}{\mathrm{d}s^2} + \frac{1}{R}\frac{\mathrm{d}u}{\mathrm{d}s}
\end{aligned}$$

The total strain of the beam is decomposed by these two components:

$$\varepsilon_1 = \frac{1}{1\frac{z}{R}}(\varepsilon_1^* + z\kappa_1^*)$$

Note that these strains are linear. Analoguously to the derivation of the equations, the internal strain energy is calculated by integrating the stress σ_1 times the change in strain $\delta\varepsilon_1$ over the beam length L and thickness t. The superscript * is ommitted in the sequel.

$$\int_{-\frac{t}{2}}^{\frac{t}{2}}\int_0^L E\left(\varepsilon_1\delta\varepsilon_1 + z\kappa_1\delta\kappa_1\right)\,\mathrm{d}x\,\mathrm{d}z = \int_0^L EA\varepsilon_1\frac{\mathrm{d}\delta u}{\mathrm{d}s} + EA\varepsilon_1\frac{\delta w}{R} - EI\kappa_1\frac{\mathrm{d}^2 w}{\mathrm{d}s^2} + \frac{EI}{R}\kappa_1\frac{\mathrm{d}\delta u}{\mathrm{d}s}\,\mathrm{d}x$$

Applying partial integration and yields the terms with δu or δw, anologuous to the derivation of the straight beam equations. Applying Hamilton's principle with the kinetic energy and external work from chapter A gives the following equations, neglecting rotary inertia:

$$\begin{aligned}
\rho A\ddot{u} - EA\frac{\mathrm{d}\varepsilon_1}{\mathrm{d}s} - \frac{EI}{R}\frac{\mathrm{d}\kappa_1}{\mathrm{d}s} &= q \\
\rho A\ddot{w} + \frac{EA}{R}\varepsilon_1 - EI\frac{\mathrm{d}^2\kappa_1}{\mathrm{d}s^2} &= p
\end{aligned} \tag{5.4}$$

The weak formulation of this system can be calculated in a similar way compared to the linear beam, except there will be extra terms related to the radius of curvature involved.

$$\begin{cases} \text{Find } (u,w) \in \left(H^1(\Omega), H^2(\Omega)\right) \text{ , } \Omega \in \mathbb{R}^1 \text{ such that:} \\ \\ \displaystyle\int_\Omega EA\left(\frac{\mathrm{d}\psi}{\mathrm{d}s}\frac{\mathrm{d}u}{\mathrm{d}s} + \frac{\mathrm{d}\psi}{\mathrm{d}s}\frac{w}{R}\right) + \frac{EI}{R}\left(-\frac{\mathrm{d}\psi}{\mathrm{d}s}\frac{\mathrm{d}^2w}{\mathrm{d}s^2} + \frac{1}{R}\frac{\mathrm{d}\psi}{\mathrm{d}s}\frac{\mathrm{d}u}{\mathrm{d}s}\right)\mathrm{d}\Omega - \\ \quad - \left[EA\left(\psi\frac{\mathrm{d}u}{\mathrm{d}s} + \frac{\psi}{R}w\right) + \frac{EI}{R}\left(-\psi\frac{\mathrm{d}^2w}{\mathrm{d}s^2}\right) + \frac{1}{R}\psi\frac{\mathrm{d}u}{\mathrm{d}s}\right]_{x_0}^{x_1} = \displaystyle\int_\Omega \psi q\,\mathrm{d}\Omega \\ \displaystyle\int_\Omega \frac{EA}{R}\left(\phi\frac{\mathrm{d}u}{\mathrm{d}s} + \phi\frac{w}{R}\right) - EI\left(-\frac{\mathrm{d}^2\phi}{\mathrm{d}s^2}\frac{\mathrm{d}^2w}{\mathrm{d}s^2} + \frac{1}{R}\frac{\mathrm{d}^2\phi}{\mathrm{d}s^2}u\right)\mathrm{d}\Omega + \\ \quad + \left[-EI\phi\left(\frac{\mathrm{d}^3w}{\mathrm{d}s^3} + \frac{1}{R}\frac{\mathrm{d}^2u}{\mathrm{d}s^2}\right) + EI\frac{\mathrm{d}\phi}{\mathrm{d}s}\left(-\frac{\mathrm{d}^2w}{\mathrm{d}s^2} + \frac{1}{R}\frac{\mathrm{d}u}{\mathrm{d}s}\right)\right]_{x_0}^{x_1} = \displaystyle\int_\Omega \phi p\,\mathrm{d}\Omega \\ \\ \forall(\psi,\phi) \in \left(H^1(\Omega), H^2(\Omega)\right) \end{cases} \tag{5.5}$$

This weak form can again be used with the Galerkin approximation, and letting $\phi = \phi_i$ and $\psi = \psi_i$ to obtain:

$$\begin{gathered} \sum_{j=1}^{m} a_j \int_\Omega EA\frac{\mathrm{d}\psi_i}{\mathrm{d}s}\frac{\mathrm{d}\psi_j}{\mathrm{d}s} + \frac{EI}{R^2}\frac{\mathrm{d}\psi_i}{\mathrm{d}s}\frac{\mathrm{d}\psi_j}{\mathrm{d}s}\,\mathrm{d}\Omega + \sum_{j=1}^{n} c_j \int_\Omega EA\frac{\mathrm{d}\psi_i}{\mathrm{d}s}\frac{\phi_j}{R} - \frac{EI}{R}\frac{\mathrm{d}\psi_i}{\mathrm{d}s}\frac{\mathrm{d}^2\phi_j}{\mathrm{d}s^2}\,\mathrm{d}\Omega - \\ - \left[\sum_{j=1}^{n} c_j\left(EA\psi_i\frac{\mathrm{d}\psi_j}{\mathrm{d}s} + \frac{EI}{R^2}\psi_i\frac{\mathrm{d}\psi_j}{\mathrm{d}s}\right) + \sum_{j=1}^{n} c_j\left(EA\psi_i\frac{\phi_j}{R} - \frac{EI}{R}\psi_i\frac{\mathrm{d}^2\phi_j}{\mathrm{d}s^2}\right)\right]_{x_0}^{x_1} = \sum_{j=1}^{m} c_j\int_\Omega \psi_i q\,\mathrm{d}\Omega \\ \sum_{j=1}^{n} a_j \int_\Omega \frac{EA}{R}\phi_i\frac{\mathrm{d}\psi_j}{\mathrm{d}s} - \frac{EI}{R}\frac{\mathrm{d}^2\phi_i}{\mathrm{d}s^2}\psi_j\,\mathrm{d}\Omega + \sum_{j=1}^{n} c_j\int_\Omega \frac{EA}{R^2}\phi_i\phi_j + EI\frac{\mathrm{d}^2\phi_i}{\mathrm{d}s^2}\frac{\mathrm{d}^2\phi_j}{\mathrm{d}s^2}\,\mathrm{d}\Omega + \\ + \left[\sum_{j=1}^{n} a_j\frac{EI}{R}\left(-\phi_i\frac{\mathrm{d}^2\psi_j}{\mathrm{d}s^2} + \frac{\mathrm{d}\phi_i}{\mathrm{d}s}\frac{\mathrm{d}\psi_j}{\mathrm{d}s}\right) + \sum_{j=1}^{n} c_j EI\left(\phi_i\frac{\mathrm{d}^3\phi_j}{\mathrm{d}s^3} - \frac{\mathrm{d}\phi_i}{\mathrm{d}s}\frac{\mathrm{d}^2\phi_j}{\mathrm{d}s^2}\right)\right]_{x_0}^{x_1} \end{gathered} \tag{5.6}$$

In all the weak formulations, the derivatives are with respect to the curve coordinate s. Since the basis functions and hence the solutions are depending on the coordinate ξ which is generally not coinciding with s, the operators have to be transformed to derivatives with respect to ξ. Basically, this is done using the results from the field of differential geometry. However, on a one-dimensional domain, the chainrule is sufficient to derive these derivatives (see for instance the work of Almstedt and Safari Hesari[121] and chapter B). Namely,

$$\begin{aligned} \frac{\partial N}{\partial x} &= \frac{\mathrm{d}N}{\mathrm{d}\xi}\frac{\mathrm{d}xi}{\mathrm{d}x} = \frac{1}{J}\frac{\mathrm{d}N}{\mathrm{d}\xi} \\ \frac{\partial^2 N}{\partial x^2} &= -\frac{1}{J^3}\frac{\mathrm{d}J}{\mathrm{d}\xi}\frac{\mathrm{d}N}{\mathrm{d}\xi} + \frac{1}{J^2}\frac{\mathrm{d}^2N}{\mathrm{d}\xi^2} \end{aligned} \tag{5.7}$$

And the differential $\mathrm{d}\Omega = J\,\mathrm{d}\hat{\Omega}$ where $\hat{\Omega}$ is the reference domain where $\xi \in \hat{\Omega}$. Hence, the integrals are also mapped. Using these derivatives in the weak form after using the Galerkin approximation in equation (5.6) allows to solve a system of equation for the curvilinear case.

5.1.3 Euler-Bernoulli Beam with Geometric Non-Linearities

In section A.2.1, more specifically in equation (A.11), the weak form for the non-linear Euler Bernoulli beam was derived. Firstly, analoguous to the Linear beam and to FEA, the Galerkin method is applied

to the system of equations. Hence, the solutions are approximated by a finite number of weighted basis functions. Note that the horizontal and vertical displacements of the midplane, u_0 and w_0, respectively, are both unknowns and approximated with different basis fucntions.

$$u_0(x,t) = \sum_{j=1}^{\infty} a_j(t)\psi_j(x) \approx \sum_{j=1}^{n} a_j(t)\psi_j \qquad w_0(x,t) = \sum_{j=1}^{\infty} c_j(t)\varphi_j(x) \approx \sum_{j=1}^{m} c_j(t)\varphi_j(x)$$

Again, a_j and c_j represent the weights of the basis functions ψ_j and φ_j, respectively. Substitution of these approximations in the weak form in equation (A.11) yields:

$$\begin{aligned}
\sum_{j=1}^{n}\left\{\int_{x_1}^{x_2} a_j EA\frac{\mathrm{d}\psi_i}{\mathrm{d}x}\frac{\mathrm{d}\psi_j}{\mathrm{d}x}\right\}\mathrm{d}x + \int_{x_1}^{x_2}\frac{EA}{2}\frac{\mathrm{d}\psi_i}{\mathrm{d}x}\left(\sum_{j=1}^{m} c_j\frac{\mathrm{d}\varphi_j}{\mathrm{d}x}\right)^2\mathrm{d}x - \sum_{j=1}^{n}\int_{x_1}^{x_2}\ddot{a}_j\rho A\psi_i\psi_j\,\mathrm{d}x \\
-EA\left[\psi\left(\frac{\mathrm{d}u_0}{\mathrm{d}x}+\frac{1}{2}\left(\frac{\mathrm{d}w_0}{\mathrm{d}x}\right)^2\right)\right]_{x_1}^{x_2} = \int_{x_1}^{x_2}\psi_i f\,\mathrm{d}x \\
\int_{x_1}^{x_2} EA\frac{\mathrm{d}\varphi_i}{\mathrm{d}x}\left(\sum_{j=1}^{m} c_j\frac{\mathrm{d}\varphi_j}{\mathrm{d}x}\right)\left(\sum_{j=1}^{n} a_j\frac{\mathrm{d}\psi_j}{\mathrm{d}x}\right)\mathrm{d}x + \int_{x_1}^{x_2}\frac{EA}{2}\frac{\mathrm{d}\varphi_i}{\mathrm{d}x}\left(\sum_{j=1}^{m} c_j\frac{\mathrm{d}\varphi_j}{\mathrm{d}x}\right)^3\mathrm{d}x + \qquad (5.8)\\
+\sum_{j=1}^{m} c_j\left\{\int_{x_1}^{x_2} EI\frac{\mathrm{d}^2\varphi_i}{\mathrm{d}x^2}\frac{\mathrm{d}^2\varphi_j}{\mathrm{d}x^2}\,\mathrm{d}x\right\} - \sum_{j=1}^{n}\int_{x_1}^{x_2}\ddot{a}_j\rho A\varphi_i\varphi_j\,\mathrm{d}x + \\
\left[-EA\left\{\varphi\frac{\mathrm{d}w_0}{\mathrm{d}x}\left(\frac{\mathrm{d}u_0}{\mathrm{d}x}+\frac{1}{2}\left(\frac{\mathrm{d}w_0}{\mathrm{d}x}\right)^2\right)\right\} + \sum_{j=1}^{n} c_j\left\{EI\varphi_i\frac{\mathrm{d}^3\varphi_j}{\mathrm{d}x^3} - EI\frac{\mathrm{d}\varphi_i}{\mathrm{d}x}\frac{\mathrm{d}^2\varphi_j}{\mathrm{d}x^2}\right\}\right]_{x_1}^{x_2} = \int_{x_1}^{x_2}\varphi_i p\,\mathrm{d}x
\end{aligned}$$

The Galerkin approximation is not substituted in all boundary terms because of their non-linear character and hence for the sake of brievety of notation. Treatment of the non-linear terms and hence also the corresponding boundary conditions is discussed in the next subsection. Furthermore, as the horizontal deflection of the mid-plane, u_0 is introduced in the non-linear Euler-Bernoulli beam, extra requirements on the boundary conditions are necessary. Based on the boundary terms of both equations,

$$\left[\underbrace{-EA\psi\left(\frac{\mathrm{d}u_0}{\mathrm{d}x}+\frac{1}{2}\left(\frac{\mathrm{d}w_0}{\mathrm{d}x}\right)^2\right)}_{\text{BC.III}}\right]_{x_1}^{x_2} \qquad (5.9)$$

$$\left[\underbrace{-EA\left\{\varphi\frac{\mathrm{d}w_0}{\mathrm{d}x}\left(\frac{\mathrm{d}u_0}{\mathrm{d}x}+\frac{1}{2}\left(\frac{\mathrm{d}w_0}{\mathrm{d}x}\right)^2\right)\right\}}_{\text{BC.II}} + \sum_{j=1}^{n} c_j\left\{\underbrace{EI\varphi_i\frac{\mathrm{d}^3\varphi_j}{\mathrm{d}x^3}}_{\text{BC I.1}} - \underbrace{EI\frac{\mathrm{d}\varphi_i}{\mathrm{d}x}\frac{\mathrm{d}^2\varphi_j}{\mathrm{d}x^2}}_{\text{BC I.2}}\right\}\right]_{x_1}^{x_2} \qquad (5.10)$$

Based on the additional boundary conditions denoted by BC.II and BC.III, additional implementations are defined:

Prescribed horizontal displacement When a horizontal displacement is prescribed, BC.III is relevant. In this case, the horizontal displacement imposes an essential boundary condition on the basis functions ψ. Similarly to previously mentioned essential boundary conditions, this boundary condition poses a restriction on the function space for basis function ψ only.

Prescribed horizontal force The horizontal force is defined by $EA\left(\frac{\mathrm{d}u_0}{\mathrm{d}x}+\frac{1}{2}\left(\frac{\mathrm{d}w_0}{\mathrm{d}x}\right)^2\right)$. Hence, a prescribed horinzontal force influences boundary integrals BC.II and BC.III. In both cases, the condition yields a natural boundary condition. However, for BC.II, the implementation of the boundary

condition as a natural boundary condition requires non-linear treatment of the extra $\frac{\mathrm{d}w_0}{\mathrm{d}x}$ term. Alternatively, the term can be assembled in the left-hand-side matrix by using the Galerkin approximation on the extra $\frac{\mathrm{d}w_0}{\mathrm{d}x}$-term, making the treatment of the BC linear. This yields in the system matrix an extra term:

$$-EA\left\{\varphi_i \frac{\mathrm{d}\varphi_j}{\mathrm{d}x}\left(\frac{\mathrm{d}u_0}{\mathrm{d}x}+\frac{1}{2}\left(\frac{\mathrm{d}w_0}{\mathrm{d}x}\right)^2\right)\right\}$$

Prescribed vertical displacement A prescribed vertical displacement was discussed for BC.I. However, BC.II requires additional treatment of the vertical displacement. Namely, this boundary condition contains the basis function φ and hence it is an essential boundary condition. Hence, the restriction of the function space of φ holds also for BC.II.

Prescribed rotation For a prescribed rotation, the first derivative of φ, which is included in $\frac{\mathrm{d}w_0}{\mathrm{d}x}$ acts as a natural boundary condition in BC.II.

As for the linear beam, the boundary conditions determine the function space of the basis functions ψ and φ. If these functions are chosen according to the boundary conditions, a system of equations can be specified. For the non-linear Euler-Bernoulli beam, the following system is obtained:

$$-\begin{bmatrix} M_A & 0 \\ 0 & M_B \end{bmatrix}\ddot{\boldsymbol{\alpha}}+\begin{bmatrix} \mathrm{K}_A & 0 \\ 0 & \mathrm{K}_B \end{bmatrix}\boldsymbol{\alpha}+\begin{bmatrix} \boldsymbol{S}_A(\boldsymbol{\alpha}) \\ \boldsymbol{S}_B(\boldsymbol{\alpha}) \end{bmatrix}=\begin{bmatrix} \boldsymbol{F}_A \\ \boldsymbol{F}_B \end{bmatrix}. \tag{5.11}$$

Where,

$$\begin{aligned}
M_{A,ij} &= \int_0^1 \rho A \psi_i \psi_j \,\mathrm{d}x, \\
M_{B,ij} &= \int_0^1 \rho A \varphi_i \varphi_j \,\mathrm{d}x, \\
K_{A,ij} &= \int_0^1 EA \frac{\mathrm{d}\psi_i}{\mathrm{d}x}\frac{\mathrm{d}\psi_j}{\mathrm{d}x} \,\mathrm{d}x, \\
K_{B,ij} &= \int_0^1 EI \frac{\mathrm{d}^2\varphi_i}{\mathrm{d}x^2}\frac{\mathrm{d}^2\varphi_j}{\mathrm{d}x^2} \,\mathrm{d}x, \\
S_{A,i}(\boldsymbol{\alpha}) &= \int_0^1 \frac{EA}{2}\frac{\mathrm{d}\psi_i}{\mathrm{d}x}\left(\sum_{j=1}^m c_j \frac{\mathrm{d}\varphi_j}{\mathrm{d}x}\right)^2 \mathrm{d}x, \\
S_{B,i}(\boldsymbol{\alpha}) &= \int_0^1 EA \frac{\mathrm{d}\varphi_i}{\mathrm{d}x}\left(\sum_{j=1}^m c_j \frac{\mathrm{d}\varphi_j}{\mathrm{d}x}\right)\left(\sum_{j=1}^n a_j \frac{\mathrm{d}\psi_j}{\mathrm{d}x}\right)\mathrm{d}x + \int_{x_1}^{x_2} \frac{EA}{2}\frac{\mathrm{d}\varphi_i}{\mathrm{d}x}\left(\sum_{j=1}^m c_j \frac{\mathrm{d}\varphi_j}{\mathrm{d}x}\right)^3 \mathrm{d}x, \\
F_{A,i} &= \int_0^1 \psi_i f \,\mathrm{d}x, \\
F_{B,i} &= \int_0^1 \varphi_i p \,\mathrm{d}x,
\end{aligned}$$

Please note that in this system the vector S depends on the solution and is hence the only non-linear term. Futhermore, by leaving out one of the sums in both S_A and S_B vectors, a modified non-linear matrix S*can be created and the system to be solved reads:

$$-\begin{bmatrix} M_A & 0 \\ 0 & M_B \end{bmatrix}\ddot{\boldsymbol{\alpha}}+\begin{bmatrix} \mathrm{K}_A & 0 \\ 0 & \mathrm{K}_B \end{bmatrix}\boldsymbol{\alpha}+\begin{bmatrix} 0 & \mathrm{S}^*_{AB}(\boldsymbol{\alpha}) \\ \mathrm{S}^*_{BA}(\boldsymbol{\alpha}) & \mathrm{S}^*_B(\boldsymbol{\alpha}) \end{bmatrix}\boldsymbol{\alpha}=\begin{bmatrix} \boldsymbol{F}_A \\ \boldsymbol{F}_B \end{bmatrix}. \tag{5.12}$$

Where,

$$S_{AB,ij}(\boldsymbol{\alpha}) = \int_0^1 \frac{EA}{2} \frac{\mathrm{d}\psi_i}{\mathrm{d}x} \frac{\mathrm{d}\varphi_j}{\mathrm{d}x} \left(\sum_{j=1}^{m} c_j \frac{\mathrm{d}\varphi_j}{\mathrm{d}x} \right) \mathrm{d}x,$$

$$S_{BA,ij}(\boldsymbol{\alpha}) = \int_0^1 EA \frac{\mathrm{d}\varphi_i}{\mathrm{d}x} \frac{\mathrm{d}\psi_j}{\mathrm{d}x} \left(\sum_{j=1}^{m} c_j \frac{\mathrm{d}\varphi_j}{\mathrm{d}x} \right) \mathrm{d}x = 2S_{BA,ji},$$

$$S_{B,ij}(\boldsymbol{\alpha}) = \int_{x_1}^{x_2} \frac{EA}{2} \frac{\mathrm{d}\varphi_i}{\mathrm{d}x} \frac{\mathrm{d}\varphi_j}{\mathrm{d}x} \left(\sum_{j=1}^{m} c_j \frac{\mathrm{d}\varphi_j}{\mathrm{d}x} \right)^2 \mathrm{d}x,$$

Alternatively, one can merge S_{BA} and S_B in a new S_B matrix by considering the coefficients c_j as unknowns instead of the a_j coefficients.

5.1.4 Initial Beam Deformations

From text books in structural analysis and buckling, it is well-known that initial deformations of beams or columns cause additional bending moments in the beam. section A.3 presents the governing equation and weak form when a straight beam is initially deformed by a function $w^*(x)$. Using the weak form from equation (A.14), additional (non-)linear stiffness matrices, denoted with superscript $*$ are found using the Galerkin approximation:

$$-\begin{bmatrix} M_A & 0 \\ 0 & M_B \end{bmatrix} \ddot{\boldsymbol{\alpha}} + \begin{bmatrix} \mathrm{K}_A + \mathrm{K}_A^* & \mathrm{K}_{AB}^* \\ \mathrm{K}_{AB}^* & \mathrm{K}_B + \mathrm{K}_B^* \end{bmatrix} \boldsymbol{\alpha} + \begin{bmatrix} \boldsymbol{S}_A(\boldsymbol{\alpha}) + \boldsymbol{S}_A^*(\boldsymbol{\alpha}) \\ \boldsymbol{S}_B(\boldsymbol{\alpha}) + \boldsymbol{S}_B^*(\boldsymbol{\alpha}) \end{bmatrix} = \begin{bmatrix} \boldsymbol{F}_A \\ \boldsymbol{F}_B \end{bmatrix}.$$

Where,

$$\begin{aligned}
\mathrm{K}_{A,ij}^* &= 0 \\
\mathrm{K}_{AB,ij}^* &= \int_0^1 EA \frac{\mathrm{d}\psi_i}{\mathrm{d}x} \frac{\mathrm{d}\varphi_j}{\mathrm{d}x} \frac{\mathrm{d}w^*}{\mathrm{d}x} \mathrm{d}x, \\
\mathrm{K}_{BA,ij}^* &= \int_0^1 EA \frac{\mathrm{d}\varphi_i}{\mathrm{d}x} \frac{\mathrm{d}\psi_j}{\mathrm{d}x} \frac{\mathrm{d}w^*}{\mathrm{d}x} \mathrm{d}x, \\
\mathrm{K}_{B,ij}^* &= \int_0^1 EA \frac{\mathrm{d}\varphi_i}{\mathrm{d}x} \frac{\mathrm{d}\varphi_j}{\mathrm{d}x} \left(\frac{\mathrm{d}w^*}{\mathrm{d}x} \right)^2 \mathrm{d}x, \\
\boldsymbol{S}_{A,i}^*(\boldsymbol{\alpha}) &= 0 \\
\boldsymbol{S}_{B,i}^*(\boldsymbol{\alpha}) &= \int_0^1 \frac{3}{2} EA \frac{\mathrm{d}\varphi_i}{\mathrm{d}x} \frac{\mathrm{d}w^*}{\mathrm{d}x} \left(\sum_{j=1}^{m} c_j \frac{\mathrm{d}\varphi_j}{\mathrm{d}x} \right)^2 \mathrm{d}x.
\end{aligned}$$

5.1.5 Hydrostatic Pressure

When hydrostatic pressure is added to the beam, the term $\rho_f g b w_0$ is added to the second equation of the system equation (5.11) as a vertically distributed shear load which is depending on the deflection of the beam. Here, b is the width of the beam, ρ_f the density of the fluid and g the graviational acceleration. The corresponding contribution to the global stiffness matrix is:

$$\mathrm{K}_{B,ij}^{HP} = \int_0^1 \rho_f g b \varphi_i \varphi_j \, \mathrm{d}x,$$

Furthermore, if an initial beam deflection is present, this deflection also contributes to hydrostatic loading and hence a contribution to the forcing vector results in

$$\mathrm{F}_{B,ij}^{HP} = \int_0^1 \rho_f g b \varphi_i w^* \,\mathrm{d}x,$$

5.1.6 Euler-Bernoulli Beam with Loading Non-Linearities

5.1.6.1 Following Pressure

In case of a following pressure $p(x)$ acting on the beam, most of the spatial discretisation from above is similar. However, the $\boldsymbol{F}$ vectors of the (non-)linear systems change according to this following pressure. Recall the definition of the normal vector from equation (A.12):

$$\boldsymbol{n} = \frac{1}{\sqrt{\left(1+\frac{\mathrm{d}u_0}{\mathrm{d}x}\right)^2 + \left(\frac{\mathrm{d}w_0}{\mathrm{d}x}\right)^2}} \begin{bmatrix} -\frac{\mathrm{d}w_0}{\mathrm{d}x} \\ 1+\frac{\mathrm{d}u_0}{\mathrm{d}x} \end{bmatrix}. \qquad \text{(see equation (A.12))}$$

As the normal vector depends on the solution in the numerator, the forcing vectors can partially be added to the blocks of S^* as follows:

$$S_{AB,ij}^*(\boldsymbol{\alpha}) = \int_0^1 \frac{EA}{2} \frac{\mathrm{d}\psi_i}{\mathrm{d}x} \frac{\mathrm{d}\varphi_j}{\mathrm{d}x} \left(\sum_{j=1}^m c_j \frac{\mathrm{d}\varphi_j}{\mathrm{d}x} \right) \mathrm{d}x + \int_0^1 \frac{p(x)\psi_i \frac{\mathrm{d}\varphi_j}{\mathrm{d}x}}{\sqrt{\left(1+\sum_{j=1}^n a_j \frac{\mathrm{d}\psi_j}{\mathrm{d}x}\right)^2 + \left(\sum_{j=1}^n c_j \frac{\mathrm{d}\varphi_j}{\mathrm{d}x}\right)^2}} \mathrm{d}x,$$

$$S_{BA,ij}^*(\boldsymbol{\alpha}) = \int_0^1 EA \frac{\mathrm{d}\varphi_i}{\mathrm{d}x} \frac{\mathrm{d}\psi_j}{\mathrm{d}x} \left(\sum_{j=1}^m c_j \frac{\mathrm{d}\varphi_j}{\mathrm{d}x} \right) \mathrm{d}x - \int_0^1 \frac{p(x)\varphi_i \frac{\mathrm{d}\psi_j}{\mathrm{d}x}}{\sqrt{\left(1+\sum_{j=1}^n a_j \frac{\mathrm{d}\psi_j}{\mathrm{d}x}\right)^2 + \left(\sum_{j=1}^n c_j \frac{\mathrm{d}\varphi_j}{\mathrm{d}x}\right)^2}} \mathrm{d}x,$$

$$S_{B,ij}^*(\boldsymbol{\alpha}) = \int_{x_1}^{x_2} \frac{EA}{2} \frac{\mathrm{d}\varphi_i}{\mathrm{d}x} \frac{\mathrm{d}\varphi_j}{\mathrm{d}x} \left(\sum_{j=1}^m c_j \frac{\mathrm{d}\varphi_j}{\mathrm{d}x} \right)^2 \mathrm{d}x,$$

And the forcing vectors are modified accordingly,

$$F_{A,i} = 0,$$
$$F_{B,i} = \int_0^1 \frac{p(x)\varphi_i}{\sqrt{\left(1+\sum_{j=1}^n a_j \frac{\mathrm{d}\psi_j}{\mathrm{d}x}\right)^2 + \left(\sum_{j=1}^n c_j \frac{\mathrm{d}\varphi_j}{\mathrm{d}x}\right)^2}} \mathrm{d}x.$$

As can be noticed, the normalisation of the normal vector introduces a non-linearity in the forcing of the beam, which has to be resolved with the Picard Iterations or Newton's method as well.

5.1.6.2 Following Force

Implementation of a following force, i.e. a force that preserves its orientation after deflection of the beam, is a combination of the implementation of vertical and horizontal forces projected on the beam using the normal vector. Suppose that a force F is applied on the end point of the beam in normal direction. Then, the boundary condition for the first equation of the non-linear system in equation (5.8) results from the normal force Fn_x whilst the boundary condition for the second equation of the non-linear system results from the horizontal force Fn_x and the vertical force $F_n y$. Similar to the following pressure, the following force adds non-linearities to the system because the forces are projected on the beam based on the normal vector from the previous iteration.

5.1.7 Nonlinear Solution Strategies

As the system of equations is non-linear, a solution strategy for solving the non-linear system needs to be included. In this section, two strategies are covered, namely the Picard Iterations and the Newton-Raphson method.

Firstly, the Picard Iteration method, as the name suggests, is an iterative method where the non-linear system is converted to a linear system where the solution in iteration $k-1$ is used to evaluate the non-linear term in iteration k [122]. In case of the system in equation (5.11), there are multiple ways to include the Picard Iteration method. One way to do this is to include the coefficients c_j^{k-1} in the matrices S^*_{AB}, S^*_{BA} and S^*_B and evaluate the sum using the (known) basis functions φ_j. In this way, the submatrices of S^* are linearised around $\boldsymbol{\alpha}^{k-1}$ and $\boldsymbol{\alpha}^k$ can be evaluated from equation (5.12) as if this was a linear equation.

Alternatively, the Newton-Raphson method (or simply Newton's method) can be used [1]. Suppose the non-linear system

$$\mathrm{G}(\boldsymbol{v}) = \mathbf{0}$$

is to be solved. Then, applying a linearisation yields:

$$\mathrm{G}(\boldsymbol{v}_k + \Delta\boldsymbol{v}) = \mathrm{G}(\boldsymbol{v}_k) + \mathrm{J}_G(\boldsymbol{v}_k)\Delta\boldsymbol{v} + \mathrm{R}(\boldsymbol{v}_k)$$

Where $\boldsymbol{v}_k$ is an already known state of the non-linear system, $\mathrm{R}(\boldsymbol{v}_k)$ is the residual due to the Taylor approximation, $\Delta\boldsymbol{v}$ is the increment of the solution and J_G is the Jacobian matrix of the stystem. By solving the right-hand-side of this line to zero, the increment $\Delta\boldsymbol{v}$ from the present state can be found. By following algorithm 1, a solution to the non-linear problem can be found iteratively. Alternatives to

Algorithm 1 Newton-Raphson method for solving non-linear system $\mathrm{G}(\boldsymbol{v}) = \mathbf{0}$

1: Initialise solution vector $\boldsymbol{v}_0$
2: Define maximum number of iterations k_{max} and tolerance TOL
3: Initialise iteration counter k and residual ε
4: **while** $\varepsilon <$TOL and $k < k_{max}$ **do**
5: Compute $\mathrm{G}(\boldsymbol{v}_k)$ and $\mathrm{J}_G(\boldsymbol{v}_k)$
6: Solve $\mathrm{J}_G(\mathrm{v}_k)\Delta\boldsymbol{v}_{k+1} = -\mathrm{G}(\boldsymbol{v}_k)$ for increment $\Delta\boldsymbol{v}_{k+1}$
7: Update solution $\boldsymbol{v}_{k+1} = \boldsymbol{v}_k + \Delta\boldsymbol{v}_{k+1}$
8: Compute residual $\varepsilon = \mathrm{G}(\boldsymbol{v}_{k+1})$.
9: **end while**

the Newton-Raphson method, such as the Quasi-Newton method or Broyden's method can be used. The former method approximates the inverse of the Jacobian matrix based on this matrix in the previous iterations and the latter method approximates the inverse of the Jacobian matrix and hence does not even need an expression for the Jacobian matrix [124, 123]. However, in this study, the Newton-Raphson method is used and hence an approximation of the Jacobian of the non-linear system is required. The Jacobian matrix is defined as follows [104]:

$$\mathrm{J}_G = \frac{\partial \boldsymbol{R}}{\partial \boldsymbol{\alpha}} = \begin{bmatrix} \frac{\partial \boldsymbol{R}_1}{\partial \boldsymbol{a}} & \frac{\partial \boldsymbol{R}_1}{\partial \boldsymbol{c}} \\ \frac{\partial \boldsymbol{R}_2}{\partial \boldsymbol{a}} & \frac{\partial \boldsymbol{R}_2}{\partial \boldsymbol{c}} \end{bmatrix}$$

Where $\boldsymbol{R} = \mathrm{D}(\boldsymbol{\alpha})\boldsymbol{\alpha} - \boldsymbol{F}$ and $\boldsymbol{R}_i$ is the residual for equation i. Matrix K in this case is the sum of both stiffness matrices in equation (5.12) and $\boldsymbol{F}$ is the right-hand-side vector. In section A.4, all Jacobian submatrices for the system of equation of the non-linear Euler-Bernoulli beam, including the ones for the

[1] The books of Wriggers[123] or de Borst et al.[124] can be used as reference for this widely-known method in non-linear finite elements

initial deformation, are given. The Jacobian submatrices for the straight beam are directly derived using [104] and are used in the work of [69], amongst others. The contributions due to initial deflections are derived using the same methodology.

5.1.8 Numerical Integration

In the present analysis, the basis functions are chosen to be B-splines (i.e. NURBS with weights 1). This means that no analytical quadrature rules are available. One could for instance use the quadrature rules described in [82, 83]. Although not optimal according to Hughes et al.[82] Gauss quadrature rules are used to evaluate the integrals for matrix assembly. More specifically, Gauss-Lobatto quadrature, which includes end points of the interval, is used. This integration rule is exact for polynomial functions with degree $2n-3$, $n=p+1$ for spline degree p and has the advantage over Gauss integration since the end-points of the piece-wise polynomials overlap with other intervals, but have to be calculated only once [125, 126]. Generally, Gauss and Gauss-Lobatto integration given weights w_i and quadrature points x_i is given by (given that the order is sufficiently high that integration is exact):

$$\int_{-1}^{1} f(x)\,\mathrm{d}x = \sum_{j=1_{qp}^{n}} w_j f(x_j) \tag{5.13}$$

Or, for an interval $[0,1]$ which is typical for normalised knot vectors,

$$\int_{0}^{1} f(x)\,\mathrm{d}x = \frac{1}{2}\sum_{j=1_{qp}^{n}} w_j f\left(\frac{x_j+1}{2}\right) \tag{5.14}$$

The weights and quadrature point of Gauss and Gauss-Lobatto rules can be found in many textbooks, including the extensive work by Abramowitz et al.[127].

5.2 Temporal Discretisation

So far the matrix equations for both linear and non-linear Euler-Bernoulli beam formulations have been derived. In both formulations (see equation (5.3) and equation (5.11)) the temporal derivatives of the weights of the approximation of the solution, $\ddot{a}_j$ and $\ddot{c}_j$, are still present. Time integration schemes are used to advance the calculations through time. In this section, different classes of time integration schemes are discussed. These methods are all based on solving

$$\dot{y} = f(y,t) \tag{5.15}$$

Where y is a time-dependent variable, $\dot{y}$ is its time dervative and $f(y,t)$ is a system that depends on the previous time step and on time. As this equation only contains first order temporal derivatives, a system with second order temporal derivatives should be rewritten into the following form [128]:

$$\begin{bmatrix}\dot{\boldsymbol{x}}\\ \ddot{\boldsymbol{x}}\end{bmatrix} = \begin{bmatrix}0 & I\\ -M^{-1}K & -M^{-1}C\end{bmatrix}\begin{bmatrix}\boldsymbol{x}\\ \dot{\boldsymbol{x}}\end{bmatrix} + \begin{bmatrix}\mathbf{0}\\ \mathrm{M}^{-1}\boldsymbol{F}(t)\end{bmatrix} \tag{5.16}$$

Here, the matrices M, B and C and the vectors $\boldsymbol{F}$ and $\boldsymbol{x}$ satisfy the following general form for a dynamic system:

$$M\ddot{\boldsymbol{x}} + C\dot{\boldsymbol{x}} + K\boldsymbol{x} = \boldsymbol{F}(t) \tag{5.17}$$

Note that the system here assumes the stiffness matrix to be linear. In the derivations of the methods, this assumption is made. Later on, in section 5.2.5, it is described how a non-linear stiffness matrix can be incorporated in the time integration method. This has similarities with the discussion in section 5.1.7.

Additionally, the Newmark method and its improvement, Bathe's method are derived. Those methods can be derived from the system presented in equation (5.16), but their derivation is usually based on

approximations of displacements, velocities and accelerations which are substituted in equation (5.17). Based on the method, these displacements, velocities and accelerations are updated each time step or substep.

Various analyses of temporal discretisation methods, i.e. time integration methods, have been presented in literature in the past years. This chapter is a summary from various time integration methods from literature and the selected methods will be used for the beam model. Summaries of time integration methods for (non-)linear structural dynamics are given by Xie[129], Dokainish and Subbaraj[130, 131] and Bathe and Baig[132]. Textbooks on this topic are written by Butcher[133] and Vuik et al.[128] amongst others. All these works are used in the following sections.

5.2.1 Implicit and Explicit Euler Methods

The implicit and Explicit Euler methods are simple methods for time integration and have been derived by Leonard Euler in 1768 [134]. Basically, the time derivative the initial value problem from equation (5.15) is approximated by a forward or backward difference step. This yields the Explicit and Implicit Euler methods, respectively. The corresponding eqautions read [133]:

$$\frac{y^{t+\Delta t} - y^t}{\Delta t} = f(y^t, t) \qquad \text{Explicit Euler Method,} \tag{5.18}$$

$$\frac{y^{t+\Delta t} - y^t}{\Delta t} = f(y^{t+\Delta t}, t+\Delta t) \qquad \text{Implicit Euler Method.} \tag{5.19}$$

Using the matrix system as derived in equation (5.16), this can be written as:

$$\begin{bmatrix} \boldsymbol{x} \\ \dot{\boldsymbol{x}} \end{bmatrix}^{t+\Delta t} = \Delta t \left(\underbrace{\begin{bmatrix} 0 & I \\ -M^{-1}K & -M^{-1}C \end{bmatrix} \begin{bmatrix} \boldsymbol{x} \\ \dot{\boldsymbol{x}} \end{bmatrix}^{t} + \begin{bmatrix} \mathbf{0} \\ \mathrm{M}^{-1}\boldsymbol{F}(t) \end{bmatrix}}_{\mathrm{A}} \right) - \begin{bmatrix} \boldsymbol{x} \\ \dot{\boldsymbol{x}} \end{bmatrix}^{t} \qquad \text{Explicit Euler} \tag{5.20}$$

$$\left(\mathrm{I} - \Delta t \begin{bmatrix} 0 & I \\ -M^{-1}K & -M^{-1}C \end{bmatrix} \right) \begin{bmatrix} \boldsymbol{x} \\ \dot{\boldsymbol{x}} \end{bmatrix}^{t+\Delta t} = \Delta t \begin{bmatrix} \mathbf{0} \\ \mathrm{M}^{-1}\boldsymbol{F}(t+\Delta t) \end{bmatrix} - \begin{bmatrix} \boldsymbol{x} \\ \dot{\boldsymbol{x}} \end{bmatrix}^{t} \qquad \text{Implicit Euler} \tag{5.21}$$

As can be see in these formulations, the names of the Euler methods are derived from the way the methods advance over time; for the Explicit method, the solution on time $t + \Delta t$ is determined by the solution on t only, whereas the Implicit method is based on solving a system of equations for $t + \Delta t$. From analyses such as those given in [134, 133, 128] amongst others, it can be shown that the Implicit and Explicit Euler methods are of order 1, i.e. that the error of these methods reduces one order if the time step reduces one order. Furthermore, the Implicit Euler method is unconditionally stable whereas the Explicit Euler method requires

$$\lambda h \in \mathcal{R}_{\text{Ex. Euler}} = \left\{ z \in \mathbb{C} \,\middle|\, |z+1| < 1 \right\}$$

The stability region of the method, $\mathcal{R}_{\text{Ex. Euler}}$, is a unit circle with center -1 in the complex plane. The eigenvalues λ of the system are the eigenvalues of the system matrix denoted by A in equation (5.20). Note that the eigenvalues are depending on δt and on the *mesh size* or knot vector spacing h via the mass, stiffness and damping matrices, M, K and C. If the damping matrix C is a zero-matrix, the eigenvalues of the system are purely imaginary and hence the Explicit Euler method is unstable for all h.

A linear combination of the Euler methods is the so-called Trapezoidal method. Basically, the method is derived from the system

$$\frac{y^{t+\Delta t} - y^t}{\Delta t} = \theta f(y^t, t) + (1-\theta) f(y^{t+\Delta t}, t+\Delta t) \tag{5.22}$$

Hence,

$$\left(\mathrm{I}-(1-\theta)\Delta t\begin{bmatrix}0 & I\\ -M^{-1}K & -M^{-1}C\end{bmatrix}\right)\begin{bmatrix}\boldsymbol{x}\\ \dot{\boldsymbol{x}}\end{bmatrix}^{t+\Delta t}=\theta\Delta t\left(\begin{bmatrix}0 & I\\ -M^{-1}K & -M^{-1}C\end{bmatrix}\begin{bmatrix}\boldsymbol{x}\\ \dot{\boldsymbol{x}}\end{bmatrix}^{t}+\begin{bmatrix}\mathbf{0}\\ \mathrm{M}^{-1}\boldsymbol{F}(t)\end{bmatrix}\right)-\begin{bmatrix}\boldsymbol{x}\\ \dot{\boldsymbol{x}}\end{bmatrix}^{t}\quad\text{Implicit Eu} \tag{5.23}$$

For $\theta=\frac{1}{2}$, the method is called the Trapezoidal method method, which is unconditionally stable and of second order [128].

5.2.2 Runge-Kutta Methods

The family of Runge-Kutta methods contains time integration schemes that are combinations of Explicit and Implicit Euler method steps devided over different stages, which are then combined to find an approximation of the solution at time step $t+\Delta t$. From [134], an s-stage Explicit Runge Kutta Method (ERK) is defined by:

$$\begin{aligned}
k_1 &= f(y_t, t),\\
k_2 &= f(y_t + \Delta t a_{21} k_1, t + c_2\Delta t),\\
k_3 &= f(y_t + \Delta t(a_{3,1}k_1 + a_{32}k_2), t + c_3\Delta t),\\
&\vdots\\
k_s &= f(y_t + \Delta t(a_{s,1}k_1 + \cdots + a_{s,s-1}k_{s-1}), t + c_s\Delta t),\\
y_{t+\Delta t} &= y_t + \Delta t\left(b_1k_1 + \cdots + b_sk_s\right),
\end{aligned} \tag{5.24}$$

Where the coefficients a_{ij}, b_i and c_j can be presented in a so-called Butcher Tableau [135]:

$$\begin{array}{c|ccccc}
c_1 & a_{11} & & & & \\
c_2 & a_{21} & a_{22} & & & \\
c_3 & a_{31} & a_{32} & a_{32} & & \\
\vdots & \vdots & \vdots & \ddots & & \\
c_s & a_{s1} & a_{s,2} & \dots & a_{s,s-1} & a_{s,s}\\
\hline
 & b_1 & b_2 & \dots & b_{s-1} & b_s
\end{array} \tag{5.25}$$

The most 'famous' Runge-Kutta method, which is the Runge-Kutta 4 (RK4) method, is defined by the following Butcher Tableau [136]:

$$\begin{array}{c|cccc}
0 & & & & \\
\frac{1}{2} & \frac{1}{2} & & & \\
\frac{1}{2} & 0 & \frac{1}{2} & & \\
1 & 0 & 0 & 1 & \\
\hline
 & \frac{1}{6} & \frac{2}{6} & \frac{2}{6} & \frac{1}{6}
\end{array} \tag{5.26}$$

Analysis, such as that presented in [128], show that the Runge-Kutta 4 method is of order 4 in time and is stable if and only if:

$$\lambda h \in \mathcal{R}_{\mathrm{RK4}} = \left\{ z \in \mathbb{C} \,\middle|\, \left|1 + z + \frac{1}{2}z^2 + \frac{1}{6}z^3 + \frac{1}{24}z^4\right| < 1 \right\}$$

In this work, the well-known fourth order Runge-Kutta method (RK4) will be used. However, variations on the general Runge-Kutta methods are as follows. As an extension to the equations in equation (5.24), the 'diagonal' coefficients a_{ii} can be added. If at least one of these coefficients is added to the method, the method contains at least one implicit solution step, making it a Diagonal Implicit Runge Kutta Method (DIRK). If, furthermore, all these diagonal elements are equal, the DIRK methods simplify to the Singly DIRK (SDIRK) methods [134]. Lastly, if the first stage of the method is explicit and all the other steps are implicit with the same diagonal coefficients, so-called Explicit first stage,

SDIRK (ESDIRK) schemes are obtained [95]. The ESDIRK schemes that are used by van Zuijlen are unconditionally stable. ERK schemes are Explicit Runge Kutta schemes, that contain the previously presented RK4 method. [137] presents the stability region of these methods. Butcher tableaus for the ESDIRK and the ERK scheme families are:

$$\text{ESDIRK:}\quad \begin{array}{c|cccc} c_1 & 0 & 0 & 0 & 0 \\ c_2 & a_{21} & a_{22} & 0 & 0 \\ c_3 & a_{31} & a_{32} & a_{33} & 0 \\ c_4 & a_{41} & a_{42} & a_{43} & a_{44} \\ \hline & b_1 & b_2 & b_3 & b_4 \end{array} \qquad \text{ERK:}\quad \begin{array}{c|cccc} c_1 & 0 & 0 & 0 & 0 \\ c_2 & a_{21} & 0 & 0 & 0 \\ c_3 & a_{31} & a_{32} & 0 & 0 \\ c_4 & a_{41} & a_{42} & a_{43} & 0 \\ \hline & b_1 & b_2 & b_3 & b_4 \end{array} \tag{5.27}$$

5.2.3 The Newmark and Wilson-θ Methods

The Newmark method was first published in 1959 by Newmark[138]. The method is widely known in the field of structural dynamics. Derivation of the method is not necessarily based on the form as written in equation (5.15) but rather on the system in equation (5.17). Namely, the method relies on the definition of the displacement and velocity on time step $t + \Delta t$ in terms of the acceleration on this time instance. Let y_t, $\dot{y}_t$ and $\ddot{y}_t$ be the displacement, velocity and accelerations at time step t. Then,

$$\begin{aligned} y_{t+\Delta t} &= y_t + \Delta t^2 \left(\frac{1}{2} - \alpha\right) \ddot{y}_t + \Delta t^2 \alpha \ddot{y}_{t+\Delta t} \\ \dot{y}_{t+\Delta t} &= \dot{y}_t + \Delta t \left(1 - \delta\right) \ddot{y}_t + \Delta t \delta \ddot{y}_{t+\Delta t} \end{aligned} \tag{5.28}$$

Substitution of these expression in the equation of motion yields:

$$\left(M + \Delta t \delta C + \Delta t^2 \alpha K\right) \ddot{y}_{t+\Delta t} = F(t + \Delta t) - C\left(y_t + \Delta t(1-\delta)\ddot{u}_t\right) - K\left(y_t + \Delta t \dot{y}_t + \Delta t^2 \left(\frac{1}{2} - \alpha\right) \ddot{y}_t\right), \tag{5.29}$$

Which can be solved for $\ddot{y}_{t+\Delta t}$. For $\delta \geq \frac{1}{2}$ and $\alpha \geq \frac{\left(\delta + \frac{1}{2}\right)^2}{4}$, the method is unconditionally stable and for $\delta = \frac{1}{2}$ the mathod has second-order accuracy. More variations of the tuning parameters are given in [131].

The Wilson-θ method is a variation on the Newmark method and was first presented in 1973 by Wilson et al.[139]. The method is a variation of the Newmark method since it computes the acceleration on time step $t + \Delta t$ using the following interpolation:

$$\ddot{y}_{t+\Delta t} = \left(1 - \frac{1}{\theta}\right) \ddot{y}_t + \frac{1}{\theta} \ddot{y}_{t+\theta\Delta t}. \tag{5.30}$$

In the case where $\theta = 1$, the method simplifies to the original Newmark method. In case of $\theta > 1$, the method works as an interpolation between the solutions on time step t and on $t + \theta\Delta t$. The latter is calculated using the Newmark method with time step $\theta\Delta t$. As mentioned in [139], the method is unconditionally stable for $\theta \geq 1.37$. Increasing θ yields an increase in numerical dissipation and accuracy is lost. Furthermore, the method has the tendency to overshoot the exact solition in the first steps of a transient analysis and hence the method is not suitable for impact loads [131]. Basically, this method can be seen as an extension of Newmark's method, as it contains an extra tuning parameter θ.

Another implicit method that can be used is the Houbolt method. In this method, accelerations and velocities are purely described by displacements at the present time step, and the previous two time steps. The method is unconditionally stable, but algorithmic damping is introduced and contrary to the Newmark and Wilson-θ methods, this cannot be tuned [131]. Additionally, the method needs a starting procedure because it uses the solution at more than one previous time step. Based on these two drawbacks of the method, it is not included in this study.

5.2.4 The Bathe Method

A relatively new method in the field of time integration methods for structural dynamics is Bathe's metod, which was introduced in 2005 by Bathe and Baig[132]. In later papers (see [140, 141, 142, 143]), Bathe investigated the method with co-authors. The motivation behind the Bathe method is that for non-linear dynamic systems, methods such as the Trapezoidal method or the Wilson-θ method lose their property of being unconditionally stable. This is especially the case when long time responses and very large deformations are considered [132]. The method proposed by Bathe and Baig is a single step, double sub-step method. In the first substep a Newmark method is used with time step $\gamma\Delta t^2$. In the second step, an Euler 3-point backward rule is adopted. Hence, the method is specified by the following equations [143]:

Step 1: (Newmark Method)

$$\begin{aligned} y_{t+\gamma\Delta t} &= y_t + \gamma\Delta t\dot{y}_t + \gamma^2\Delta t^2\left[\left(\frac{1}{2}-\alpha\right)\ddot{y}_t + \alpha\ddot{y}_{t+\gamma\Delta t}\right], \\ \dot{y}_{t+\gamma\Delta t} &= \dot{y}_t + \gamma\Delta t\left[(1-\delta)\,\ddot{y}_t + \delta\ddot{y}_{t+\gamma\Delta t}\right]. \end{aligned} \tag{5.31}$$

Then, solve

$$\mathrm{M}\ddot{y}_{t+\gamma\Delta t} + \mathrm{C}\dot{y}_{t+\gamma\Delta t} + \mathrm{K}\dot{y}_{t+\gamma\Delta t} = \boldsymbol{F}(t+\gamma\Delta t), \tag{5.32}$$

To obtain $\ddot{y}_{t+\gamma\Delta t}$ and substitute this in equation (5.31) to obtain $y_{t+\gamma\Delta t}$ and $\dot{y}_{t+\gamma\Delta t}$.

Step 2: (Euler 3-point backward rule)
With $y_{t+\gamma\Delta t}$, $\dot{y}_{t+\gamma\Delta t}$ and $\ddot{y}_{t+\gamma\Delta t}$, compute

$$\begin{aligned} y_{t+\Delta t} &= c_1 y_t + c_2 y_{t+\gamma\Delta t} + c_3 y_{t+\Delta t}, \\ \dot{y}_{t+\Delta t} &= c_1\dot{y}_t + c_2\dot{y}_{t+\gamma\Delta t} + c_3\dot{y}_{t+\Delta t}, \end{aligned} \tag{5.33}$$

Where,

$$c_1 = \frac{1-\gamma}{\gamma\Delta t} \quad c_2 = \frac{-1}{(1-\gamma)\gamma\Delta t} \quad c_3 = \frac{2-\gamma}{(1-\gamma)\Delta t}.$$

Then, solve

$$\mathrm{M}\ddot{y}_{t+\Delta t} + \mathrm{C}\dot{y}_{t+\Delta t} + \mathrm{K}\dot{y}_{t+\Delta t} = \boldsymbol{F}(t+\Delta t), \tag{5.34}$$

To obtain $\ddot{y}_{t+\Delta t}$ and substitute this in equation (5.33) to obtain $y_{t+\Delta t}$ and $\dot{y}_{t+\Delta t}$.

The Bathe method is of second order, since both the Newmark method and the Euler 3-point backward rule are of second order. Furthermore, the method is unconditionally stable, even in case of non-linear equations with large time steps. The latter is a clear advantage compared to the trapezoidal method [140].

In [142], the Bathe method is investigated for linear analyses. In this paper, the method was investigated for $\gamma > 1$. As found in the paper, this choice of γ implies large amplitude decays. Furthermore, they investigated the use of $\alpha = 1$, $\delta = 3/4$ and $\gamma = 0.5$ for the first time step, in order to prevent an overshoot in the acceleration of one degree of freedom in their test case. However, they recommend to not use these coefficients in the complete simulation, as the method becomes first order accurate and loses its unconditional stability.

[2] Note: in [132, 140, 141, 142] the trapezoidal method is used as a first step. Basically, this is the Newmark method for $\alpha = \frac{1}{4}$ and $\delta = \frac{1}{2}$. Furthermore, in [140, 141, 142], $\gamma = \frac{1}{2}$ is adopted.

5.2.5 Temporal Discretisation of Non-Linear Equations of Motion

In the discussion of the various temporal discretisation methods in the previous subsections, the stiffness matrix K was assumed to be constant. As discussed in section 5.1.3, the discretisation of the non-linear Euler-Bernoulli beam equations, however, requires iterative solution procedures. Since explicit time integration methods use only previous solutions in the solution procedure, the system matrix only depends on the previous solution and hence no iterative solution procedure is required for these methods. For the implicit methods, however, a non-linear system of equations needs to be solved and hence iterative methods are required here.

[131], amongst others, discusses treatment of a non-linear system for use of the time integration methods. The method that is discussed uses for the equation of motion:

$$\mathrm{M}\boldsymbol{x}_{t+\Delta t}^{\cdot\cdot} + \mathrm{C}\boldsymbol{x}_{t+\Delta t}^{\cdot} + \mathrm{D}(\boldsymbol{x}_{t+\Delta t}) = \boldsymbol{F}(t+\Delta t)$$

Since the stiffness matrix can be linearised in time, it can be written as:

$$\mathrm{D}(\boldsymbol{x}_{t+\Delta t}) \approx \mathrm{D}(\boldsymbol{x}_t) + \mathrm{J}_D(\boldsymbol{x}_t)\delta\boldsymbol{x}$$

Where $\delta\boldsymbol{x} = \boldsymbol{x}_{t+\Delta t} - \boldsymbol{x}$. Substituting this in the non-linear equation of motion gives:

$$\mathrm{M}\boldsymbol{x}_{t+\Delta t}^{\cdot\cdot} + \mathrm{C}\boldsymbol{x}_{t+\Delta t}^{\cdot} + \mathrm{J}_D(\boldsymbol{x}_t)\delta\boldsymbol{x} = \boldsymbol{F}(t+\Delta t) - \mathrm{D}(\boldsymbol{x}_{t+\Delta t})$$

This can iteratively be solved using

$$\mathrm{M}\boldsymbol{x}_{t+\Delta t}^{i\,\cdot\cdot} + \mathrm{C}\boldsymbol{x}_{t+\Delta t}^{i\,\cdot} + \mathrm{J}_D(\boldsymbol{x}_{t+\Delta t})\Delta\boldsymbol{x} = \boldsymbol{F}(t+\Delta t) - \mathrm{D}(\boldsymbol{x}_{t+\Delta t}^{i-1})$$

And $\delta\boldsymbol{x}_{t+\Delta t}^{i} = \delta\boldsymbol{x}_{t+\Delta t}^{i-1} + \Delta\boldsymbol{x}^{i}$.

Alternatively, Picard iterations can be used for each time step. Using this solution strategy, iterations are also performed per time step and if the solution on time t converged, the temporal solution procedure is continued to the next time step.

5.3 Benchmarks

5.3.1 Spatial Convergence

For verification of the implemented beam model, a pinned-pinned beam subject to a uniform load of $1\ N/m$ is modelled using the linear and nonlinear beam models. The bending stiffness is chosen to be unity, i.e. $EI = 1$. Furthermore, axial stiffness has been set to a unitary value for the nonlinear beam as well, i.e. $EA = 1$. For the linear beam, analytical solutions are available and for the nonlinear model, the method of manufactured solution is used. Here, the analytical solution for the linear beam is utilised as vertical displacements, while horizontal displacements are set to zero. Thus, for the pinned-pinned case:

$$\begin{aligned} u_m(x) &= 0 \\ w_m(x) &= \frac{qx}{24EI}\left(L^3 - 2Lx^2 + x^3\right) \end{aligned}$$

Substituting these manufactured solutions in the system of equations for the nonlinear beam gives the forcings that need to be applied to simulate the manufactured solutions. For the pinned-pinned case:

$$\begin{aligned} f(x) &= \frac{EAq^2(4x^3 - 6Lx^2 + L^3)x(x-L)}{48EI^2} \\ g(x) &= \frac{(xEA(L-x)(L-2x)^2(L^2+2Lx-2x^2)^2q^2 + 768EI^3)q}{768EI^3} \end{aligned}$$

Consequently, the convergence of the Isogeometric linear and nonlinear beam models with respect to the analytical and manufactured can be calculated to verify the computation as well as the code. The results for the convergence analysis are depicted in figure 5.1, where the error ε is plotted for different step sizes h. The error is defined by (unless stated otherwise):

$$\varepsilon = \sqrt{\int_{\Omega} (u_{\text{num}} - u_{\text{an}})^2}$$

Where u_{num} and u_{an} are the numerical and analytical/manufactured solutions, respectively. For the nonlinear beam, the errors for the solution in horizontal and vertical direction are separated. Furthermore, the order of the B-splines is different for the bases of the solution in these directions. The order of the B-splines that represent the vertical solution is varied between 2 and 4 keeping the horzontal basis of second order. Furthermore, for the verical solution, the order is varied between 1 and 2, keeping the vertical basis 4th order. Both variations are because the requirements of the spaces of the basis functions. For the horizontal displacement errors, the following observations are made:

- For both the linear and the non-linear beam, second-order convergence is observed for second-order B-spline basis functions. Generally, however, a third-order convergence is expected from theoretical results for IGA. Furthermore, 'wiggles' are observed for finer meshes for both beam models.
- For both beam models, fourth-order convergence is observed for third-order basis funtions, which is in line with theoretical results in IGA. Furthermore, no wiggles are present for finer meshes.
- Lastly, errors of order $\mathcal{O}\left(10^{-15}\right)$ are observed for fourth-order basis functions. These errors are assumed to be determined by machine precision and hence it can be concluded that they represent the analytical/manufactured solution exactly. This is in line with the fact that the analytical and manufactures solutions are fourth-order polynomial functions and hence can be represented exactly by fourth-order piecewise polynomial basis functions.
- A first-order basis in the horizontal direction of the nonlinear beam gives a constant error which is orders higher than machine precision whereas second order basis functions give machine precision errors. Hence, it can be concluded that the solution in the horizontal direction is of second order to keep the displacements zero.

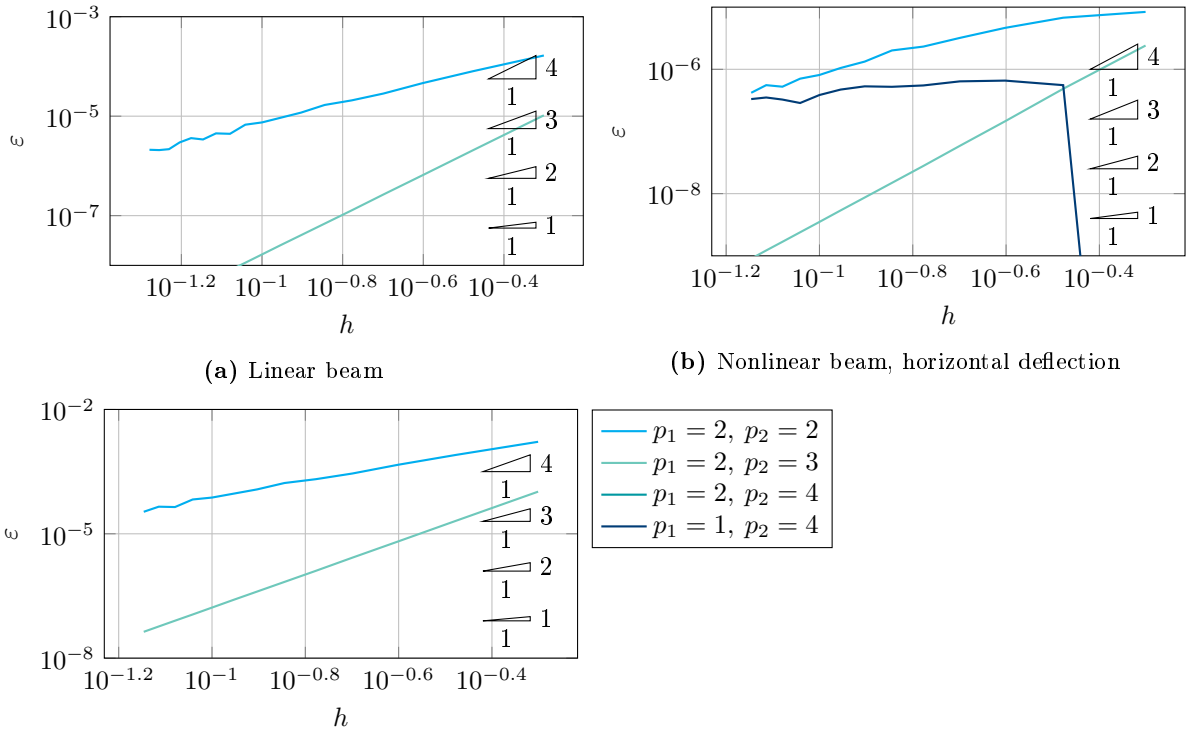

(a) Linear beam

(b) Nonlinear beam, horizontal deflection

(c) Nonlinear beam, vertical deflection

Figure 5.1: Spatial convergence of linear beam (top left), and the horizontal and vertical deflections for the nonlinear beam (top right, bottom) for different orders of the knot vector of the knot vectors for the vertical deflection (Ξ_2, p_2) and the horizontal deflection (Ξ_1, p_1). h is the step size in the knot vectors, i.e. unique knot values are $\Xi_i = \{0, h, 2h, \ldots, 1\}$. Furthermore, $EI = 1\ Nm^2$, $EA = 1\ N$, $q = 1\ N/m$, $L = 1\ m$.

Table 5.2: Order of time integration methods, according to [133, 95]

Method	Order
Implicit/Explicit Euler	1
Bathe, Newmark, Trapezium	2
ERK 3, ESDIRK 3	3
ERK 4, ESDIRK 4, Runge-Kutta 4	4

5.3.2 Temporal Convergence

For verification of the dynamic beam models, the method of manufactured solutions is used for both the linear and the nonlinear model. The reason for using a manufactured solution for the linear model instead of a analytical solution for a vibrating string is that the sine-shaped analytical solution needs to be represented by more B-spline basis functions compared to a polynomial solution. Consequently, this means that the error that is made by constructing an initial condition is orders higher than machine precision and hence it will easily dominate the time discretisation error. Hence, to validate the time integration method, it is more convenient to use a manufactured solution that is polynomial, such that the spatial discretisation error (and hence the error of the initial condition) is of the order of the machine precision. The manufactured solution for the beam models is given by (solution $u(x)$ only for non-linear beam):

$$\begin{aligned} u(x) &= 0 \\ w(x) &= \frac{x}{24}\left(1 - 2x^2 + x^3\right)\cos(\omega\pi t) \end{aligned}$$

Which shows that for $t = 0$ the manufactured solution (thus the initial condition) is equal to a pinned-pinned beam with a unitary distributed load. Substituting this in the (non)linear system of equations gives the following right-hand sides:

Linear beam:

$$f(x) = -\frac{1}{24}\left[\rho A x \pi^2 \omega^2 (x-1)(x^2 - x - 1) - 24EI)\right]\cos(\omega\pi t)$$

Nonlinear beam:

$$\begin{aligned} f(x) &= -\frac{EA}{48EI^2}\cos(\omega\pi t)^2(4x^3 - 6x^2 + 1)x(x-1) \\ g(x) &= -\frac{\frac{1}{2}x(x^2 - x - 1/2)^2 EA\left(x - \frac{1}{2}\right)^2(x-1)\cos^2(\omega\pi t)}{24EI^3} \\ &\quad + \frac{\left(\rho A\pi^2\omega^2 x^4 - 2\rho A\pi^2\omega^2 x^3 + \rho A\pi^2\omega^2 x - 24EI\right)\cos(\omega\pi t)}{24EI} \end{aligned}$$

From literature, orders of convergence for various time integration methods can be found, which are summarised in table 5.2. Using these orders of convergence, the discretisation errors for both space and time can be made of same order by the fact that:

$$\mathcal{O}(\varepsilon) = \mathcal{O}\left(\Delta\xi^{p+1}\right) + \mathcal{O}\left(\Delta t^q\right), \tag{5.35}$$

Where Δt is the time step, $\Delta\xi$ is the knot spacing, p is the order of the B-splines or NURBS and q is the expected order of the time integration method. To make the total error of the method purely depending on the mesh size, the time step can be scaled according to:

$$\Delta t = (\Delta\xi)^{\frac{p+1}{q}} \tag{5.36}$$

Alternatively, $\Delta\xi$ can be chosen sufficiently large so that the discretisation error is smaller than the temporal discretisation error in the considered domain for Δt. The results for the linear and non-linear dynamic beams are given in figure 5.2. The following is observed:

- All time integration methods converge in the expected orders from table 5.2 for the linear beam.
- For the non-linear beam, some exceptions are observed for the theoretic oders of convergence. Namely,
  1. In figure 5.2b, i.e. the convergence plot for the error of the horizontal displacements, the Implicit Euler method converges second order for large time steps, makes a peak around $\Delta t \sim \mathcal{O}\left(5 \cdot 10^{-4}\right)$ and converges after this peak with its expected order of convergence, i.e. first order.
  2. Also in figure 5.2b, the Bathe method shows the same behaviour but the peak depth is less and occurs around $\Delta t \sim \mathcal{O}\left(2 \cdot 10^{-3}\right)$ after which it converges with first order, while second order was expected.
- The explicit character of the Explicit Euler method, the Runge-Kutta 4 method, the ERK 3 method and the Wilson-θ method can be seen in case of the linear beam. For the nonlinear beam, the time step is chosen sufficiently small such that the eigenvalues of the system are located within the stability region for all methods and for the range of considered time steps.

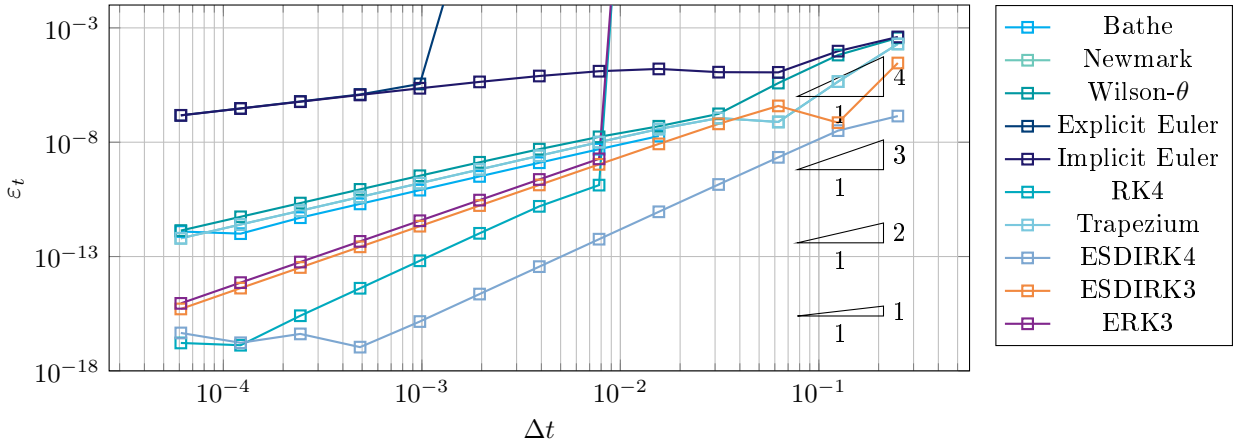

(a) Linear Beam

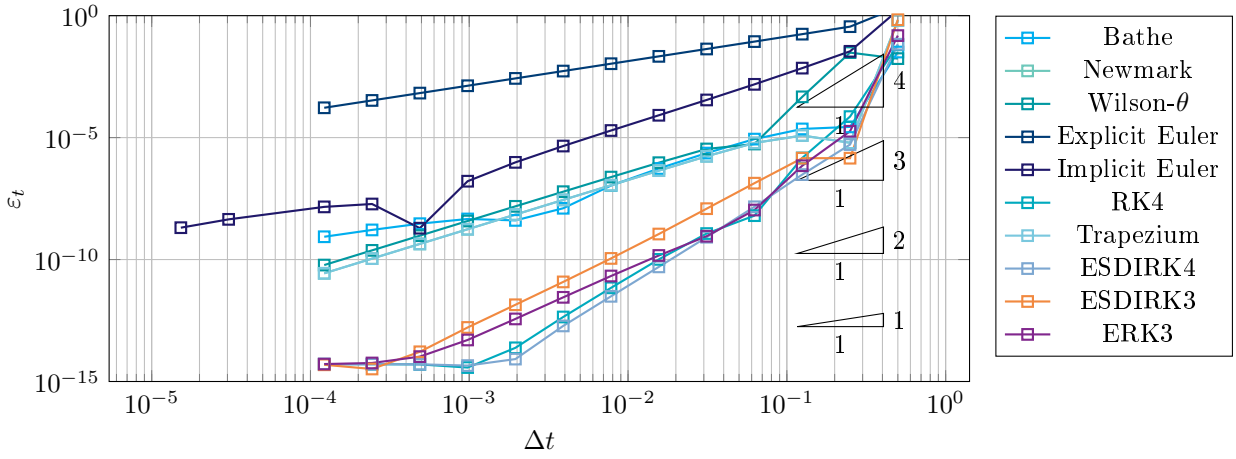

(b) Nonlinear beam, horizontal deflections

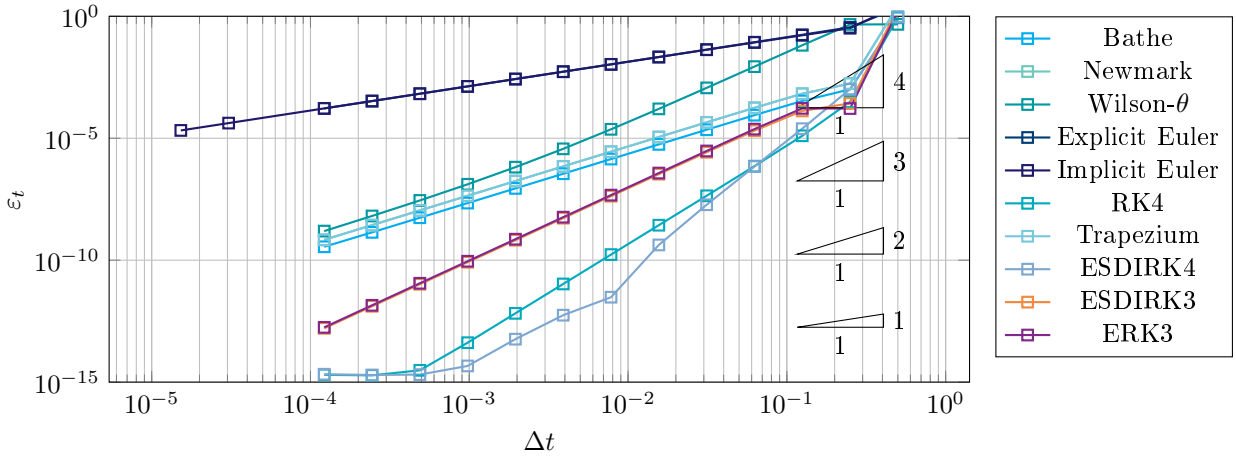

(c) Nonlinear beam, horizontal deflections.

Figure 5.2: Convergence plots with the L_2-error ε against the time step Δt for different time integration methods. The linear beam (top) is considered in free vibration with $EI = 1\,Nm^2$, $\rho A = 1\,kg/m$ and $t = 1\,s$. For the non-linear beam, $EI = 1\,Nm^2$, $EA = 1\,N$, $\rho A = 10^3\,kg/m$ and $t = 2\,s$ and the frequency parameter for the manufactured solution is $\omega = 4$. For the linear and non-linear models, the unique knot vector is $\Xi = \{0, 0.5, 1\}$ and the orders of the basis functions are 4 for the vertical deflection and 2 for the horizontal deflection solutions.

5.3.3 Spectral Properties

One of the advantages of IGA over ordinary finite elements that was published first by Cottrell et al.[144] in 2006 is its superior accuracy in the prediction of eigenfrequencies and mode shapes. Later Weeger et al.[69] published similar results for linear and non-linear beams in 2013. Where finite element methods show so-called *optical branches* in the frequency spectrum when $n/N > 0.5$, i.e. for upper-half part of the discrete eigenfrequency spectrum, IGA does not show these branches. This leads to a more accurate representation of the eigenvalues. In this section, an eigenvalue spectrum similar to that of Cottrell et al. and Weeger et al. will be built for comparison purposes for the linear beam only.

Basically, the eigenfrequency calculations follows naturally from the dynamic beam model, as it is defined by the eigenvalues of the following system:

$$(-\boldsymbol{\omega}^2 M + K)\Psi = \lambda\Psi$$

Here, $\boldsymbol{\omega}$ is a vector containing the first n eigenvalues of the discrete system and Ψ is a matrix containing n eigenvectors of the system. In IGA, these eigenvectors can be transformed to mode shapes using the basis functions. Both matrices M and K are in $\mathbb{R}^{n\times n}$.

In figure 5.3a, the ratio $\omega_h/\omega - 1$ is plotted on the vertical axis, where $\omega_{h,i}$ are numerically obtained eigenfrequencies and ω_i are the analytical eigenfrequencies which are $(i\pi)^2$ for a pinned-pinned beam. On the horizontal axis, the eigenfrequency number i over the number of degrees of freedom n is plotted. Although the resolution is rather low, i.e. n is small, the same height of the curves is obtained as in [144, 69]. According to this paper, it should indeed not depend on the number of discrete frequencies. For illustration purposes, the first five mode shapes of the pinned-pinned beam are presented in figure 5.3b.

Furthermore, another result published in [144] is the convergence of the first three eigenfrequencies with respect to the grid size, i.e. the knot vector refinements. Figure 5.4 presents the convergence of the first three eigenfrequencies for different orders of B-splines. Analoguous to the observations in [144] the frequencies indeed converge in order $2(p-1)$ for a pinned-pinned beam.

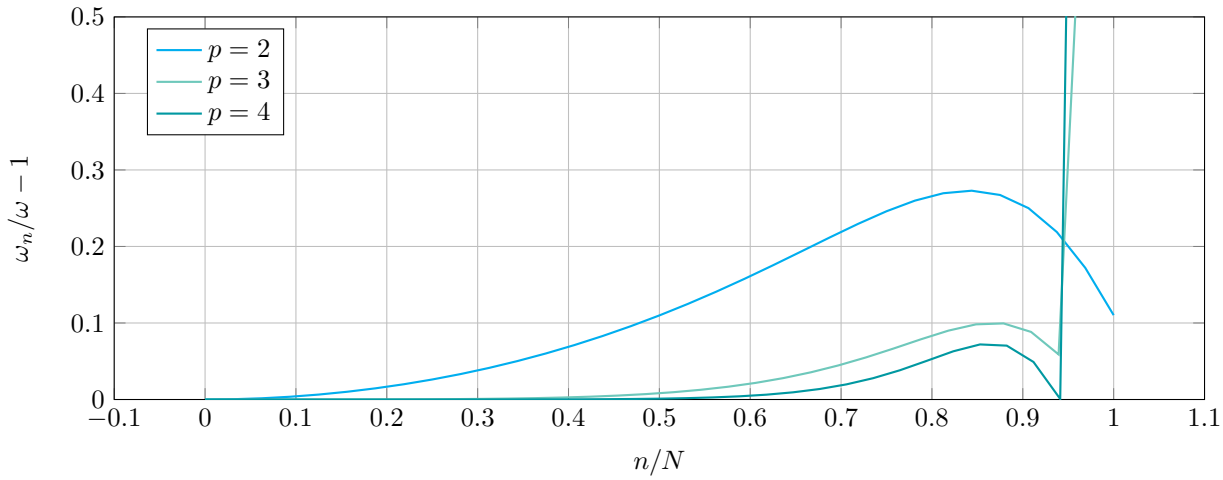

(a) Eigenfrequency ratio $\frac{\omega_n}{\omega} - 1$.

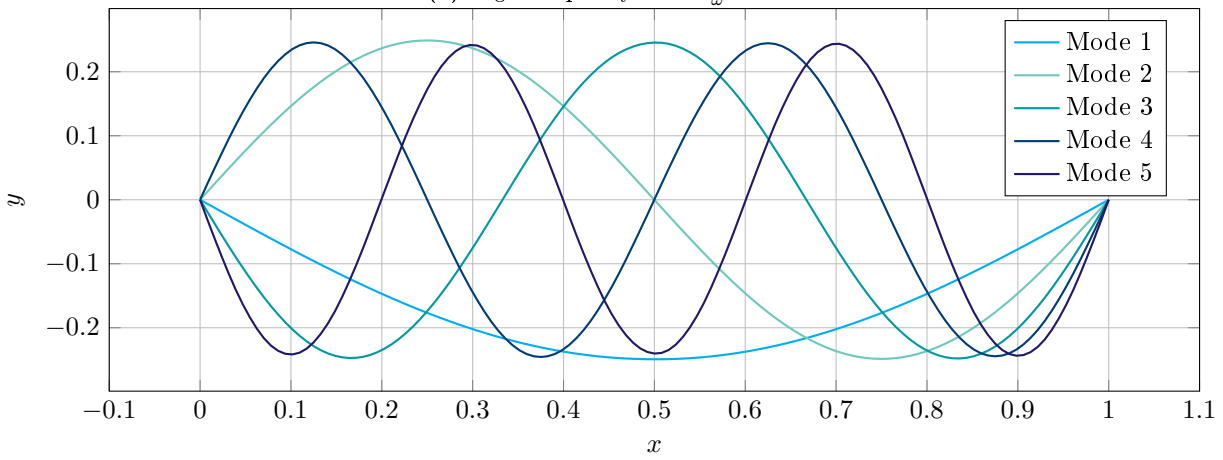

(b) First five mode shapes.

Figure 5.3: Numerical eigenfrequency ω_n over analytical eigenfrequency ω for mode n (top) and first five numerical mode shapes (bottom). The (unique) knot vector is $\Xi = \left\{0, \frac{1}{16}, \frac{2}{16}, \ldots, 1\right\}$ and the order is $p = 2/dots4$.

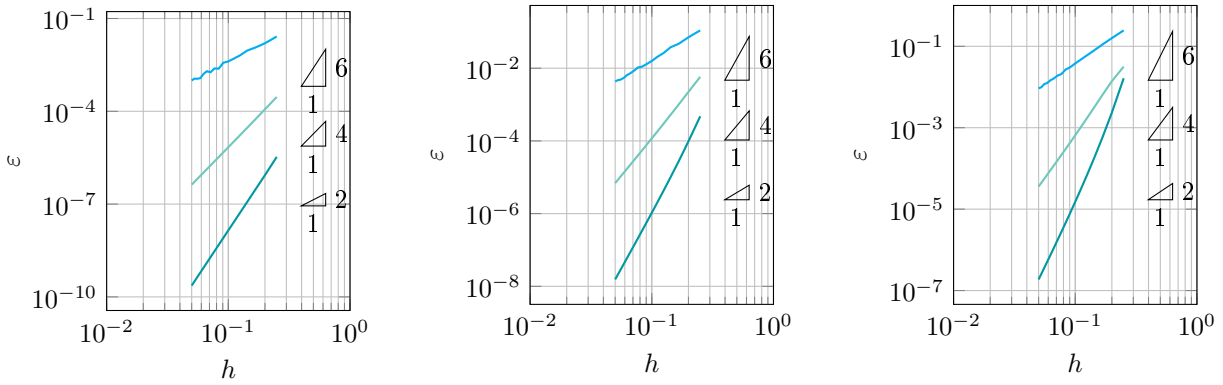

(a) ω_1 **(b)** ω_2 **(c)** ω_3

Figure 5.4: Convergence of the first three eigenfrequencies $\omega_1, \omega_2, \omega_3$ for mesh size or knot span h. The error ε is an L_2 error between the numerical eigenfrequency ω_i and the analytical eigenfrequency $\omega = (i\pi)^2$. Orders of the knot vectors range from 2 to 4.

Table 5.3: Deflection (down, left) $[m]$ of the tip of the quarter circular (radius 1) arch subject to a moment $M = -1\,Nm$, or a vertical/horizontal force $F = -1\,N$ on the end point. The cross-section is considered rectangular with a height of $0.01\,m$ a width of $0.2\,m$ and a Young's modulus of $1\,GPa$. The basis functions are B-splines with a (unique) knot vector $\Xi = \{0, 0.5, 1\}$ and an order of 4.

	Numerical		Numerical with analytical Jacobian		Analytical	
Case	Vertical	Horizontal	Vertical	Horizontal	Vertical	Horizontal
Moment	0.0591	0.0335	0.0598	0.0343	0.0600	0.0342
Vertical Force	0.0458	0.0291	0.0469	0.0301	0.0471	0.0300
Horizontal Force	0.0291	0.0206	0.0301	0.0213	0.0300	0.0214

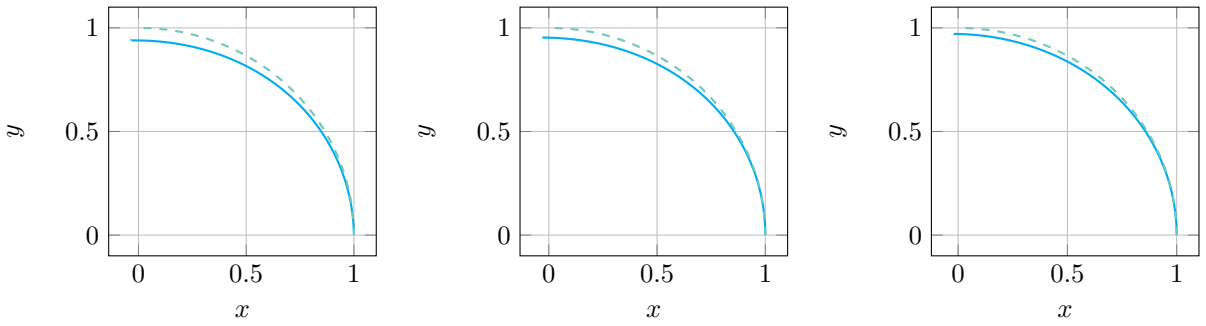

(a) Moment **(b)** Vertical Force **(c)** Horizontal Force

Figure 5.5: Deformed shape of the quarter circular arch (radius 1) subject to a moment $M = -1\,Nm$, or a vertical/horizontal force $F = -1\,N$ on the end point. The cross-section is considered rectangular with a height of $0.01\,m$ a width of $0.2\,m$ and a Young's modulus of $1\,GPa$. The basis functions are B-splines with a (unique) knot vector $\Xi = \{0, 0.5, 1\}$ and an order of 4.

5.3.4 Curvilinear Models

The curvilinear beam model, which was described in section 5.3.4, has been verified with the data from Cazzani et al.[67, 68] and Almstedt and Safari Hesari[121]. In all models, the curvilinear operators have been calculated numerically, despite they could be calculated analytically for the specific cases. The results are presented in figure 5.5 and table 5.3. The following can be observed:

- Generally, the results match well with the analytical solution for this knot vector and order.
- When evaluating the Jacobian numerically, the error is larger. Since the Jacobian is decomposed by basis functions (see section 5.3.4), a constant Jacobian (which is the case for this geometry) is approximated by B-splines which are generally non-constant. This implies that errors are made when evaluating the Jacobian. Increasing the order or increasing the number of knots and control points increases the number of basis functions, allowing for a more accurate description of a constant Jacobian with a zero-derivative.

Furthermore, figure 5.6 depicts convergence results for the three load cases of the quarter circluar arch. In this case, the curvilinear operators are calculated analytically to be sure that the error arises from discretisation only. If the operators are calculated numerically, functions that are constant over the geometry (such as the radius of curvature) are approximated by higher order B-splines and hence not constant. It can be observed that in all three cases, the observed order of convergence is $2p$ for B-splines with order p.

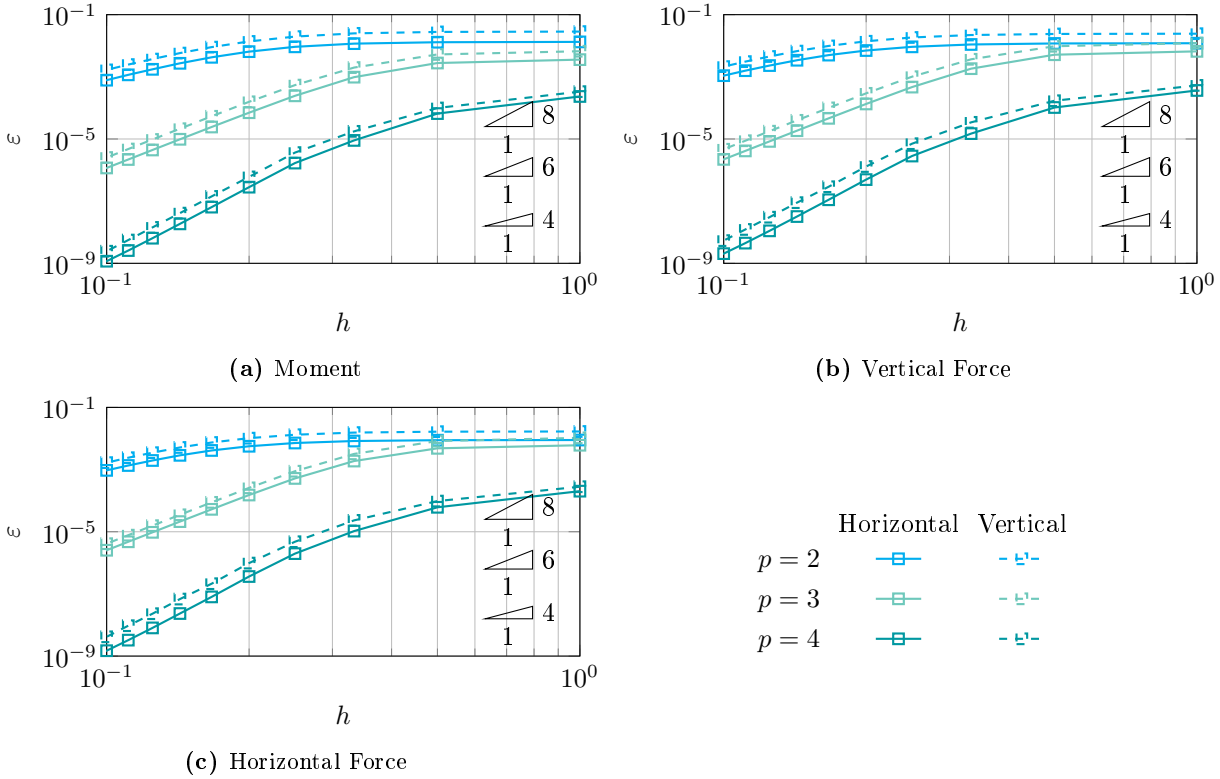

(a) Moment

(b) Vertical Force

(c) Horizontal Force

Figure 5.6: Convergence plots for a quarter circular arch with radius 1 with B-splines of orders 2 up to 4 and knot vectors $\Xi = \{0, 1/k, \ldots, (k-1)/k, 1\}$, $k = 2 \ldots 8$. The arch is subject to a moment $M = -1 Nm$, or a vertical/horizontal force $F = -1\ N$ on the end point. The cross-section is considered rectangular with a height of $0.01\,m$ a width of $0.2\,m$ and a Young's modulus of $1\,GPa$

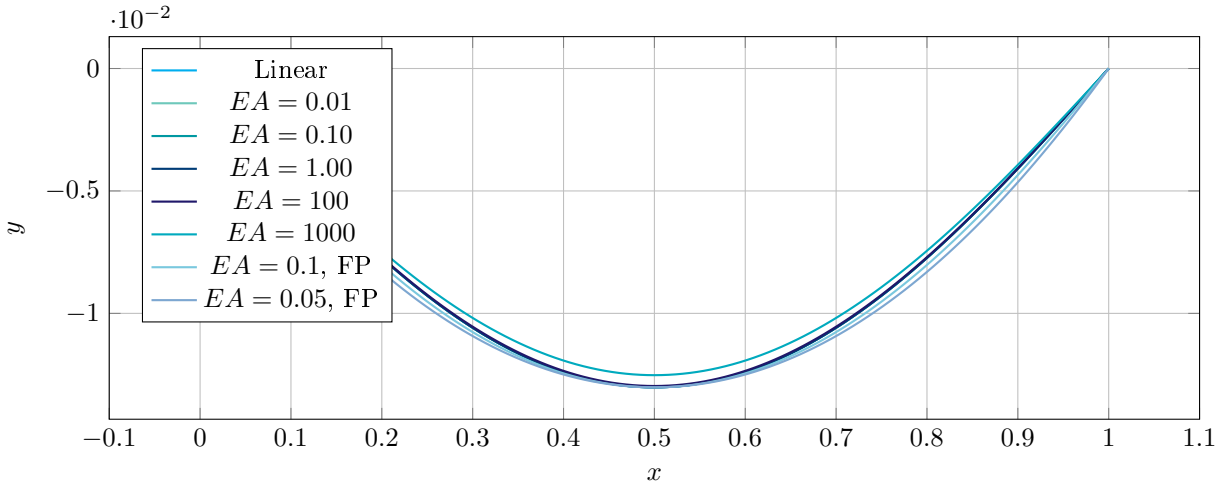

Figure 5.7: Following Pressure

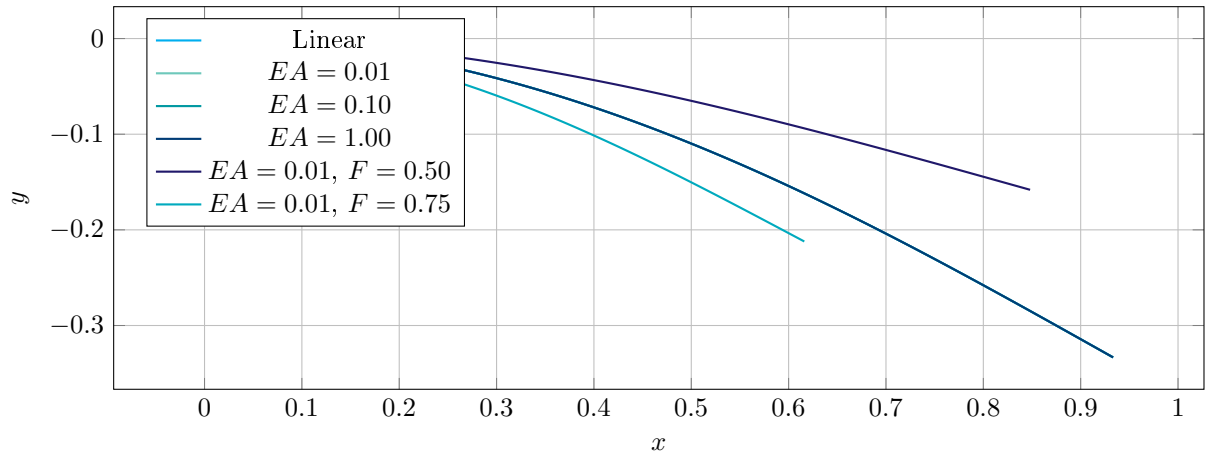

Figure 5.8: Following Force

5.3.5 Effects of Following Force and Following Pressure

The last case study that is performed for the beam model specifically is regarding the effects of the following force and the following pressure. For both situations, no manufactured solutions can be constructed, since the force and pressure are the only unknowns for the system and can hence not be specified based on two equations. In figures 5.7 and 5.8, the results of the nonlinear beam given a following force or pressure acting on the beam are given. As seen in these figures, a following pressure causes the beam to be more evenly curved and the following force causes shortening of the beam, because the force has a nonzero horizontal projection.

Bibliography

[1] Robert A Adams and John JF Fournier. *Sobolev spaces*, volume 140. Elsevier, 2003.

[2] COP21 UNFCCC. Paris agreement. *FCCCC/CP/2015/L. 9/Rev. 1*, 2015.

[3] Latvia & the European Commission et al. Intended nationally determined contribution of the eu and its member states, 2015.

[4] Xuefei Wang, Xiangwu Zeng, Jiale Li, Xu Yang, and Haijun Wang. A review on recent advancements of substructures for offshore wind turbines. *Energy Conversion and Management*, 158:103–119, feb 2018. ISSN 0196-8904. doi: 10.1016/J.ENCONMAN.2017.12.061. URL https://www.sciencedirect.com/science/article/pii/S019689041731213X.

[5] Global Wind Energy Council. Global wind energy report 2016. Anual Report 10, Global Wind Energy Council, apr 2017.

[6] Z. Gao, H B Bingham, D Ingram, A Kolios, D Karmakar, T Utsunomiya, I Catipovic, G Colicchio, J Miguel Rodrigues, F Adam, D G Karr, C Fang, H.K. Shin, J Slätte, C Ji, W Sheng, P Liu, and L Stoev. Committee V.4 report: Offshore Renewable Energy. In M. L. Kaminski and P Rigo, editors, *Progress in Marine Science and Technology: Proceedings of the 20th International Ship and Offshore Structures Congress*, volume II, pages 193–277. IOS Press, 2018. doi: 10.3233/978-1-61499-864-8-193.

[7] Liliana Rusu and Florin Onea. Assessment of the performances of various wave energy converters along the European continental coasts. *Energy*, 82:889–904, mar 2015. ISSN 03605442. doi: 10.1016/j.energy.2015.01.099. URL https://www.sciencedirect.com/science/article/pii/S0360544215001231.

[8] Eugen Rusu and Florin Onea. A review of the technologies for wave energy extraction. *Clean Energy*, 2(1):10–19, 2018.

[9] Mohd Nasir Ayob, Valeria Castellucci, and Rafael Waters. Wave energy potential and 1–50 TWh scenarios for the Nordic synchronous grid. *Renewable Energy*, 2017. ISSN 18790682. doi: 10.1016/j.renene.2016.09.004.

[10] Rodrigo C Lisboa, Paulo R F Teixeira, and Conceição Juana Fortes. Numerical evaluation of wave energy potential in the south of Brazil. *Energy*, 121:176–184, 2017. ISSN 0360-5442. doi: https://doi.org/10.1016/j.energy.2017.01.001. URL http://www.sciencedirect.com/science/article/pii/S0360544217300014.

[11] Christina Kalogeri, George Galanis, Christos Spyrou, Dimitris Diamantis, Foteini Baladima, Marika Koukoula, and George Kallos. Assessing the European offshore wind and wave energy resource for combined exploitation. *Renewable Energy*, 2017. ISSN 18790682. doi: 10.1016/j.renene.2016.08.010.

[12] H. Bahaidarah, Abdul Subhan, P. Gandhidasan, and S. Rehman. Performance evaluation of a PV (photovoltaic) module by back surface water cooling for hot climatic conditions. *Energy*, 2013. ISSN 03605442. doi: 10.1016/j.energy.2013.07.050.

[13] A. Akbarzadeh and T. Wadowski. Heat pipe-based cooling systems for photovoltaic cells under concentrated solar radiation. *Applied Thermal Engineering*, 16(1):81–87, jan 1996. ISSN 13594311. doi: 10.1016/1359-4311(95)00012-3. URL https://www.sciencedirect.com/science/article/pii/1359431195000123.

[14] Alok Sahu, Neha Yadav, and K. Sudhakar. Floating photovoltaic power plant: A review. *Renewable and Sustainable Energy Reviews*, 66:815–824, dec 2016. ISSN 1364-0321. doi: 10.1016/J.RSER.2016.08.051. URL https://www-sciencedirect-com.tudelft.idm.oclc.org/science/article/pii/S1364032116304841?{_}rdoc=1{&}{_}fmt=high{&}{_}origin=gateway{&}{_}docanchor={&}md5=b8429449ccfc9c30159a5f9aeaa92ffb{&}ccp=y.

[15] EMODnet Bathymetry Consortium et al. Emodnet digital bathymetry (dtm). *EMODnet Bathymetry. doi*, 10, 2016.

[16] R Meerkötter, G Gesell, V Grewe, C König, S Lohmann, and H Mannstein. A high resolution European cloud climatology from 15 years of NOAA/AVHRR data. In *Proc. 2004 EUMETSAT Meteorological Conference, Prague, Czech Republic*, volume 31. Citeseer, 2004.

[17] Mario Marcello Miglietta, Thomas Huld, and Fabio Monforti-Ferrario. Local Complementarity of Wind and Solar Energy Resources over Europe: An Assessment Study from a Meteorological Perspective. *Journal of Applied Meteorology and Climatology*, 2017. ISSN 1558-8424. doi: 10.1175/JAMC-D-16-0031.1.

[18] Masashi Kashiwagi. A time-domain mode-expansion method for calculating transient elastic responses of a pontoon-type VLFS. *Journal of Marine Science and Technology*, 5(2):89–100, dec 2000. ISSN 0948-4280. doi: 10.1007/PL00010631. URL http://link.springer.com/10.1007/PL00010631.

[19] Olaf Waals. Life@sea: future use of our oceans. Presented at The Floating Future Seminar 2018, Wageningen, The Netherlands, March 2018. URL http://www.marin.nl/web/Events/Events-archive/Events-2018/Seminar-The-Floating-Future.htm.

[20] Masashi Kashiwagi. Research On Hydroelastic Responses of VLFS" Recent Progress And Future Work. jan 1999. URL https://www.onepetro.org/conference-paper/ISOPE-I-99-003.

[21] Masashi Kashiwagi. A B-spline Galerkin scheme for calculating the hydroelastic response of a very large floating structure in waves. *Journal of Marine Science and Technology*, 3(1):37–49, mar 1998. ISSN 0948-4280. doi: 10.1007/BF01239805. URL http://link.springer.com/10.1007/BF01239805.

[22] Masashi Kashiwagi. Transient responses of a VLFS during landing and take-off of an airplane. *Journal of Marine Science and Technology*, 9(1):14–23, may 2004. ISSN 0948-4280. doi: 10.1007/s00773-003-0168-0. URL http://link.springer.com/10.1007/s00773-003-0168-0.

[23] Alexey Andrianov. Hydroelastic analysis of very large floating structures. *Doctorale thesis, Delft University of Technology*, 2005.

[24] Miguel Lamas-Pardo, Gregorio Iglesias, and Luis Carral. A review of Very Large Floating Structures (VLFS) for coastal and offshore uses. *Ocean Engineering*, 109:677–690, nov 2015. ISSN 0029-8018. doi: 10.1016/J.OCEANENG.2015.09.012. URL https://www.sciencedirect.com/science/article/pii/S0029801815004783.

[25] Th. P. Gerostathis, K. A. Belibassakis, and G. A. Athanassoulis. 3D hydroelastic analysis of very large floating bodies over variable bathymetry regions. *Journal of Ocean Engineering and Marine Energy*, 2(2):159–175, may 2016. ISSN 2198-6444. doi: 10.1007/s40722-016-0046-6. URL http://link.springer.com/10.1007/s40722-016-0046-6.

[26] C M Wang and Z Y Tay. Hydroelastic analysis and response of pontoon-type very large floating structures. In *Fluid structure interaction II*, pages 103–130. Springer, 2011.

[27] Wei Wei, Shixiao Fu, Torgeir Moan, Chunhui Song, and Tongxin Ren. A time-domain method for hydroelasticity of very large floating structures in inhomogeneous sea conditions. *Marine Structures*, 57:180–192, jan 2018. ISSN 09518339. doi: 10.1016/j.marstruc.2017.10.008. URL https://www.sciencedirect.com/science/article/pii/S0951833917301156.

[28] Muhammad Riyansyah, C M Wang, and Y S Choo. Connection design for two-floating beam system for minimum hydroelastic response. *Marine Structures*, 23(1):67–87, 2010. ISSN 0951-8339. doi: https://doi.org/10.1016/j.marstruc.2010.01.001. URL http://www.sciencedirect.com/science/article/pii/S095183391000002X.

[29] T I Khabakhpasheva and A A Korobkin. Hydroelastic behaviour of compound floating plate in waves. *Journal of Engineering Mathematics*, 44(1):21–40, sep 2002. ISSN 1573-2703. doi: 10.1023/A:1020592414338. URL https://doi.org/10.1023/A:1020592414338.

[30] Takuji Hamamoto. Stochastic fluid—structure interaction of large circular floating islands during wind waves and seaquakes. *Probabilistic Engineering Mechanics*, 10(4):209–224, jan 1995. ISSN 0266-8920. doi: 10.1016/0266-8920(95)00017-8. URL https://www.sciencedirect.com/science/article/pii/0266892095000178?via{%}3Dihub.

[31] Don O. Brush, Bo O. Almroth, and J. W. Hutchinson. Buckling of Bars, Plates, and Shells. *Journal of Applied Mechanics*, 1975. ISSN 00218936. doi: 10.1115/1.3423755.

[32] Owen F. Hughes, Jeom Kee. Paik, and Dominique. Béghin. *Ship structural analysis and design*. Society of Naval Architects and Marine Engineers, 2010. ISBN 0939773821.

[33] Bo Li, Yan-Ping Cao, Xi-Qiao Feng, and Huajian Gao. Mechanics of morphological instabilities and surface wrinkling in soft materials: a review. *Soft Matter*, 8(21):5728, may 2012. ISSN 1744-683X. doi: 10.1039/c2sm00011c. URL http://xlink.rsc.org/?DOI=c2sm00011c.

[34] Marco Rivetti. Non-symmetric localized fold of a floating sheet. *Comptes Rendus Mécanique*, 341(3):333–338, mar 2013. ISSN 1631-0721. doi: 10.1016/J.CRME.2013.01.005. URL https://www.sciencedirect.com/science/article/pii/S1631072113000211.

[35] Marco Rivetti and Sébastien Neukirch. The mode branching route to localization of the finite-length floating elastica. *Journal of the Mechanics and Physics of Solids*, 69:143–155, sep 2014. ISSN 0022-5096. doi: 10.1016/J.JMPS.2014.05.004. URL https://www.sciencedirect.com/science/article/pii/S0022509614000878.

[36] Haim Diamant and Thomas A. Witten. Compression Induced Folding of a Sheet: An Integrable System. *Physical Review Letters*, 107(16):164302, oct 2011. ISSN 0031-9007. doi: 10.1103/PhysRevLett.107.164302. URL https://link.aps.org/doi/10.1103/PhysRevLett.107.164302.

[37] Etienne Jambon-Puillet, Dominic Vella, and Suzie Protière. The compression of a heavy floating elastic film. *Soft Matter*, 12(46):9289–9296, nov 2016. ISSN 1744-683X. doi: 10.1039/C6SM00945J. URL http://xlink.rsc.org/?DOI=C6SM00945J.

[38] E. Cerda and L. Mahadevan. Geometry and Physics of Wrinkling. *Physical Review Letters*, 2003. ISSN 10797114. doi: 10.1103/PhysRevLett.90.074302.

[39] Luka Pocivavsek, Robert Dellsy, Andrew Kern, Sebastián Johnson, Binhua Lin, Ka Yee C. Lee, and Enrique Cerda. Stress and fold localization in thin elastic membranes. *Science*, 2008. ISSN 00368075. doi: 10.1126/science.1154069.

[40] Enrique Cerda, Sahraoui Chaieb, Francisco Melo, and L. Mahadevan. Conical dislocations in crumpling. *Nature*, 401(6748):46–49, sep 1999. ISSN 0028-0836. doi: 10.1038/43395. URL http://www.nature.com/articles/43395.

[41] E. Cerda, K. Ravi-Chandar, and L. Mahadevan. Wrinkling of an elastic sheet under tension. *Nature*, 419(6907):579–580, oct 2002. ISSN 0028-0836. doi: 10.1038/419579b. URL http://www.nature.com/articles/419579b.

[42] B. Audoly. Localized buckling of a floating elastica. *Physical Review E*, 84(1):011605, jul 2011. ISSN 1539-3755. doi: 10.1103/PhysRevE.84.011605. URL https://link.aps.org/doi/10.1103/PhysRevE.84.011605.

[43] Yan-Ping Cao, Xiu-Peng Zheng, Fei Jia, and Xi-Qiao Feng. Wrinkling and creasing of a compressed elastoplastic film resting on a soft substrate. *Computational Materials Science*, 57: 111–117, may 2012. ISSN 0927-0256. doi: 10.1016/J.COMMATSCI.2011.02.038. URL https://www.sciencedirect.com/science/article/pii/S0927025611001376.

[44] Dominic Vella, Amin Ajdari, Ashkan Vaziri, and Arezki Boudaoud. Wrinkling of pressurized elastic shells. *Physical Review Letters*, 2011. ISSN 00319007. doi: 10.1103/PhysRevLett.107.174301.

[45] Matteo Taffetani and Dominic Vella. Regimes of wrinkling in pressurized elastic shells. *Philosophical transactions. Series A, Mathematical, physical, and engineering sciences*, 375(2093):20160330, may 2017. ISSN 1364-503X. doi: 10.1098/rsta.2016.0330. URL http://www.ncbi.nlm.nih.gov/pubmed/28373387http://www.pubmedcentral.nih.gov/articlerender.fcgi?artid=PMC5379047.

[46] You-Jun Ning, Zheng-Cai Zhang, Bin Gu, Alamusi, and Fei Jia. Surface instability and wrinkling pattern evolution on a fluid-supported inhomogeneous film. *The European Physical Journal Plus*, 132(4):170, apr 2017. ISSN 2190-5444. doi: 10.1140/epjp/i2017-11448-2. URL http://link.springer.com/10.1140/epjp/i2017-11448-2.

[47] Arthur A. Evans, Saverio E. Spagnolie, Denis Bartolo, and Eric Lauga. Elastocapillary self-folding: buckling, wrinkling, and collapse of floating filaments. *Soft Matter*, 9(5):1711–1720, jan 2013. ISSN 1744-683X. doi: 10.1039/C2SM27089G. URL http://xlink.rsc.org/?DOI=C2SM27089G.

[48] Till Jakob Wenzel Wagner. *Elastocapillarity: Adhesion and large deformations of thin sheets*. PhD thesis, University of Cambridge, 2013.

[49] Till J. W. Wagner and Dominic Vella. Floating carpets and the delamination of elastic sheets. *Physical Review Letters*, 107(4):044301, jul 2011. ISSN 00319007. doi: 10.1103/PhysRevLett.107.044301. URL https://link.aps.org/doi/10.1103/PhysRevLett.107.044301.

[50] B.K. Hadi. Wrinkling of sandwich column: comparison between finite element analysis and analytical solutions. *Composite Structures*, 53(4):477–482, sep 2001. ISSN 0263-8223. doi: 10.1016/S0263-8223(01)00060-5. URL https://www.sciencedirect.com/science/article/pii/S0263822301000605.

[51] T.J.R. Hughes, J.A. Cottrell, and Y. Bazilevs. Isogeometric analysis: CAD, finite elements, NURBS, exact geometry and mesh refinement. *Computer Methods in Applied Mechanics and Engineering*, 194(39-41):4135–4195, oct 2005. ISSN 0045-7825. doi: 10.1016/J.CMA.2004.10.008. URL https://www.sciencedirect.com/science/article/pii/S0045782504005171{#}fig1.

[52] J.A. Cottrell, T.J.R. Hughes, and A. Reali. Studies of refinement and continuity in isogeometric structural analysis. *Computer Methods in Applied Mechanics and Engineering*, 196(41-44):4160–4183, sep 2007. ISSN 0045-7825. doi: 10.1016/J.CMA.2007.04.007. URL https://www.sciencedirect.com/science/article/pii/S0045782507001703?via{%}3Dihub.

[53] J. Austin Cottrell, Thomas J.R. Hughes, and Yuri Bazilevs. *Isogeometric Analysis: Toward Integration of CAD and FEA*. 2009. ISBN 9780470748732. doi: 10.1002/9780470749081.

[54] Vinh Phu Nguyen, Cosmin Anitescu, Stéphane P.A. Bordas, and Timon Rabczuk. Isogeometric analysis: An overview and computer implementation aspects. *Mathematics and Computers in Simulation*, 117:89–116, nov 2015. ISSN 0378-4754. doi: 10.1016/J.MATCOM.2015.05.008. URL https://www-sciencedirect-com.tudelft.idm.oclc.org/science/article/pii/S0378475415001214?{_}rdoc=1{&}{_}fmt=high{&}{_}origin=gateway{&}{_}docanchor={&}md5=b8429449ccfc9c30159a5f9aeaa92ffb.

[55] J. Kiendl, K.-U. Bletzinger, J. Linhard, and R. Wüchner. Isogeometric shell analysis with Kirchhoff–Love elements. *Computer Methods in Applied Mechanics and Engineering*, 198(49-52):3902–3914, nov 2009. ISSN 0045-7825. doi: 10.1016/J.CMA.2009.08.013. URL https://www-sciencedirect-com.tudelft.idm.oclc.org/science/article/pii/S0045782509002680?{_}rdoc=1{&}{_}fmt=high{&}{_}origin=gateway{&}{_}docanchor={&}md5=b8429449ccfc9c30159a5f9aeaa92ffb.

[56] J. Kiendl, Y. Bazilevs, M.-C. Hsu, R. Wüchner, and K.-U. Bletzinger. The bending strip method for isogeometric analysis of Kirchhoff–Love shell structures comprised of multiple patches. *Computer Methods in Applied Mechanics and Engineering*, 199(37-40):2403–2416, aug 2010. ISSN 0045-7825. doi: 10.1016/J.CMA.2010.03.029. URL https://www.sciencedirect.com/science/article/pii/S0045782510001064?via{%}3Dihub.

[57] Josef Kiendl, Ming-Chen Hsu, Michael C.H. Wu, and Alessandro Reali. Isogeometric Kirchhoff–Love shell formulations for general hyperelastic materials. *Computer Methods in Applied Mechanics and Engineering*, 291:280–303, jul 2015. ISSN 0045-7825. doi: 10.1016/J.CMA.2015.03.010. URL https://www-sciencedirect-com.tudelft.idm.oclc.org/science/article/pii/S0045782515001127?{_}rdoc=1{&}{_}fmt=high{&}{_}origin=gateway{&}{_}docanchor={&}md5=b8429449ccfc9c30159a5f9aeaa92ffb.

[58] Farshad Roohbakhshan and Roger A. Sauer. Efficient isogeometric thin shell formulations for soft biological materials. *Biomechanics and Modeling in Mechanobiology*, 16(5):1569–1597, oct 2017. ISSN 1617-7959. doi: 10.1007/s10237-017-0906-6. URL http://link.springer.com/10.1007/s10237-017-0906-6.

[59] Jia Lu and Chao Zheng. Dynamic cloth simulation by isogeometric analysis. *Computer Methods in Applied Mechanics and Engineering*, 268:475–493, jan 2014. ISSN 0045-7825. doi: 10.1016/J.CMA.2013.09.016. URL https://www.sciencedirect.com/science/article/pii/S0045782513002430{#}f0070.

[60] D.J. Benson, Y. Bazilevs, M.C. Hsu, and T.J.R. Hughes. Isogeometric shell analysis: The Reissner–Mindlin shell. *Computer Methods in Applied Mechanics and Engineering*, 199(5-8):276–289, jan 2010. ISSN 0045-7825. doi: 10.1016/J.CMA.2009.05.011. URL https://www.sciencedirect.com/science/article/pii/S0045782509001820.

[61] L. Beirão da Veiga, A. Buffa, C. Lovadina, M. Martinelli, and G. Sangalli. An isogeometric method for the Reissner–Mindlin plate bending problem. *Computer Methods in Applied Mechanics and Engineering*, 209-212:45–53, feb 2012. ISSN 0045-7825. doi: 10.1016/J.CMA.2011.10.009. URL https://www.sciencedirect.com/science/article/pii/S0045782511003215?via{%}3Dihub.

[62] J. N. Reddy. *Theory and Analysis of Elastic Plates and Shells, Second Edition*. CRC Press, nov 2006. ISBN 9780849384165. doi: 10.1201/9780849384165. URL https://www.taylorfrancis.com/books/9780849384165.

[63] Son Thai, Nam Il Kim, and Jaehong Lee. Isogeometric cable elements based on B-spline curves. *Meccanica*, 52(4-5):1219–1237, 2017. ISSN 15729648. doi: 10.1007/

s11012-016-0454-7. URL https://link-springer-com.tudelft.idm.oclc.org/content/pdf/10.1007{%}2Fs11012-016-0454-7.pdf.

[64] S.B. Raknes, X. Deng, Y. Bazilevs, D.J. Benson, K.M. Mathisen, and T. Kvamsdal. Isogeometric rotation-free bending-stabilized cables: Statics, dynamics, bending strips and coupling with shells. *Computer Methods in Applied Mechanics and Engineering*, 263:127–143, aug 2013. ISSN 00457825. doi: 10.1016/j.cma.2013.05.005. URL http://linkinghub.elsevier.com/retrieve/pii/S0045782513001229.

[65] Sang Jin Lee and Kyoung Sub Park. Vibrations of Timoshenko beams with isogeometric approach. *Applied Mathematical Modelling*, 37(22):9174–9190, nov 2013. ISSN 0307-904X. doi: 10.1016/J.APM.2013.04.034. URL https://www.sciencedirect.com/science/article/pii/S0307904X13002874.

[66] Anh-Tuan Luu, Nam-Il Kim, and Jaehong Lee. Isogeometric vibration analysis of free-form Timoshenko curved beams. *Meccanica*, 50(1):169–187, jan 2015. ISSN 0025-6455. doi: 10.1007/s11012-014-0062-3. URL http://link.springer.com/10.1007/s11012-014-0062-3.

[67] Antonio Cazzani, Marcello Malagù, and Emilio Turco. Isogeometric analysis of plane-curved beams. *Mathematics and Mechanics of Solids*, 21(5):562–577, 2016. doi: 10.1177/1081286514531265. URL http://journals.sagepub.com/doi/pdf/10.1177/1081286514531265.

[68] Antonio Cazzani, Marcello Malagù, Emilio Turco, and Flavio Stochino. Constitutive models for strongly curved beams in the frame of isogeometric analysis. *Mathematics and Mechanics of Solids*, 21(2):182–209, 2016. doi: 10.1177/1081286515577043. URL http://journals.sagepub.com/doi/pdf/10.1177/1081286515577043.

[69] Oliver Weeger, Utz Wever, and Bernd Simeon. Isogeometric analysis of nonlinear Euler-Bernoulli beam vibrations. *Nonlinear Dynamics*, 2013. ISSN 0924090X. doi: 10.1007/s11071-013-0755-5.

[70] Radek Kolman, Sergey Sorokin, Bohumír Bastl, Ján Kopačka, and Jiří Plešek. Isogeometric analysis of free vibration of simple shaped elastic samples. *The Journal of the Acoustical Society of America*, 137(4):2089–2100, apr 2015. ISSN 0001-4966. doi: 10.1121/1.4916199. URL http://asa.scitation.org/doi/10.1121/1.4916199.

[71] X.C. Qin, C.Y. Dong, F. Wang, and X.Y. Qu. Static and dynamic analyses of isogeometric curvilinearly stiffened plates. *Applied Mathematical Modelling*, 45:336–364, may 2017. ISSN 0307-904X. doi: 10.1016/J.APM.2016.12.035. URL https://www.sciencedirect.com/science/article/pii/S0307904X17300124.

[72] T. J R Hughes, A. Reali, and G. Sangalli. Duality and unified analysis of discrete approximations in structural dynamics and wave propagation: Comparison of p-method finite elements with k-method NURBS. *Computer Methods in Applied Mechanics and Engineering*, 197(49-50):4104–4124, sep 2008. ISSN 00457825. doi: 10.1016/j.cma.2008.04.006. URL https://www-sciencedirect-com.tudelft.idm.oclc.org/science/article/pii/S0045782508001618.

[73] F. Auricchio, M. Conti, M. Ferraro, S. Morganti, A. Reali, and R. L. Taylor. Innovative and efficient stent flexibility simulations based on isogeometric analysis. *Computer Methods in Applied Mechanics and Engineering*, 295:347–361, oct 2015. ISSN 00457825. doi: 10.1016/j.cma.2015.07.011. URL https://www-sciencedirect-com.tudelft.idm.oclc.org/science/article/pii/S0045782515002236.

[74] S. Morganti, F. Auricchio, D. J. Benson, F. I. Gambarin, S. Hartmann, T. J.R. Hughes, and A. Reali. Patient-specific isogeometric structural analysis of aortic valve closure. *Computer Methods in Applied Mechanics and Engineering*, 284:508–520, feb 2015. ISSN 00457825. doi: 10.1016/j.cma.2014.10.010. URL https://www-sciencedirect-com.tudelft.idm.oclc.org/science/article/pii/S0045782514003806.

[75] Y. Bazilevs, V. M. Calo, J. A. Cottrell, J. A. Evans, T. J.R. Hughes, S. Lipton, M. A. Scott, and T. W. Sederberg. Isogeometric analysis using T-splines. *Computer Methods in Applied Mechanics and Engineering*, 2010. ISSN 00457825. doi: 10.1016/j.cma.2009.02.036. URL https://www.sciencedirect.com/science/article/pii/S0045782509000875.

[76] Thomas W. Sederberg, Jianmin Zheng, Almaz Bakenov, and Ahmad Nasri. T-splines and T-NURCCs. *ACM Transactions on Graphics*, 22(3):477, 2003. ISSN 07300301. doi: 10.1145/882262.882295. URL http://portal.acm.org/citation.cfm?doid=1201775.882295http://portal.acm.org/citation.cfm?doid=882262.882295.

[77] Michael R. Dörfel, Bert Jüttler, and Bernd Simeon. Adaptive isogeometric analysis by local h-refinement with T-splines. *Computer Methods in Applied Mechanics and Engineering*, 199 (5-8):264–275, jan 2010. ISSN 0045-7825. doi: 10.1016/J.CMA.2008.07.012. URL https://www.sciencedirect.com/science/article/pii/S0045782508002569?via{%}3Dihub.

[78] Tae-Kyoung Uhm and Sung-Kie Youn. T-spline finite element method for the analysis of shell structures. *International Journal for Numerical Methods in Engineering*, 80(4):507–536, oct 2009. ISSN 00295981. doi: 10.1002/nme.2648. URL http://doi.wiley.com/10.1002/nme.2648.

[79] Ming Chen Hsu, David Kamensky, Fei Xu, Josef Kiendl, Chenglong Wang, Michael C.H. Wu, Joshua Mineroff, Alessandro Reali, Yuri Bazilevs, and Michael S. Sacks. Dynamic and fluid–structure interaction simulations of bioprosthetic heart valves using parametric design with T-splines and Fung-type material models. *Computational Mechanics*, 55(6):1211–1225, jun 2015. ISSN 01787675. doi: 10.1007/s00466-015-1166-x. URL http://link.springer.com/10.1007/s00466-015-1166-x.

[80] K.V. Kostas, A.I. Ginnis, C.G. Politis, and P.D. Kaklis. Ship-hull shape optimization with a T-spline based BEM–isogeometric solver. *Computer Methods in Applied Mechanics and Engineering*, 284:611–622, feb 2015. ISSN 0045-7825. doi: 10.1016/J.CMA.2014.10.030. URL https://www.sciencedirect.com/science/article/pii/S0045782514004009?via{%}3Dihub.

[81] Manfred Bischoff, E. Ramm, and J. Irslinger. Models and Finite Elements for Thin-Walled Structures. In *Encyclopedia of Computational Mechanics Second Edition*, pages 1–86. John Wiley & Sons, Ltd, Chichester, UK, dec 2017. doi: 10.1002/9781119176817.ecm2026. URL http://doi.wiley.com/10.1002/9781119176817.ecm2026.

[82] T. J R Hughes, A. Reali, and G. Sangalli. Efficient quadrature for NURBS-based isogeometric analysis. *Computer Methods in Applied Mechanics and Engineering*, 2010. ISSN 00457825. doi: 10.1016/j.cma.2008.12.004.

[83] F. Auricchio, F. Calabrò, T. J.R. Hughes, A. Reali, and G. Sangalli. A simple algorithm for obtaining nearly optimal quadrature rules for NURBS-based isogeometric analysis. *Computer Methods in Applied Mechanics and Engineering*, 2012. ISSN 00457825. doi: 10.1016/j.cma.2012.04.014.

[84] Nathan Collier, David Pardo, Lisandro Dalcin, Maciej Paszynski, and V.M. Calo. The cost of continuity: A study of the performance of isogeometric finite elements using direct solvers. *Computer Methods in Applied Mechanics and Engineering*, 213-216:353–361, mar 2012. ISSN 0045-7825. doi: 10.1016/J.CMA.2011.11.002. URL https://www.sciencedirect.com/science/article/pii/S0045782511003392?via{%}3Dihub.

[85] Nathan Collier, Lisandro Dalcin, David Pardo, and V. M. Calo. The Cost of Continuity: Performance of Iterative Solvers on Isogeometric Finite Elements. *SIAM Journal on Scientific Computing*, 35(2):A767–A784, jan 2013. ISSN 1064-8275. doi: 10.1137/120881038. URL http://epubs.siam.org/doi/10.1137/120881038.

[86] Daniel Garcia, David Pardo, Lisandro Dalcin, Maciej Paszyński, Nathan Collier, and Victor M. Calo. The value of continuity: Refined isogeometric analysis and fast direct solvers. *Computer Methods in Applied Mechanics and Engineering*, 316:586–605, apr 2017. ISSN 00457825.

doi: 10.1016/j.cma.2016.08.017. URL https://www.sciencedirect.com/science/article/pii/S0045782516309586.

[87] Th von Karman. The impact on seaplane floats during landing, 1929. URL https://authors.library.caltech.edu/47898/http://authors.library.caltech.edu/47898/{%}5Cnhttp://naca.central.cranfield.ac.uk/report.php?NID=766.

[88] Herbrt Wagner. Über Stoß- und Gleitvorgänge an der Oberfläche von Flüssigkeiten. *ZAMM - Zeitschrift für Angewandte Mathematik und Mechanik*, 12(4):193–215, jan 1932. ISSN 15214001. doi: 10.1002/zamm.19320120402. URL http://doi.wiley.com/10.1002/zamm.19320120402.

[89] Adel Shams and Maurizio Porfiri. Treatment of hydroelastic impact of flexible wedges. *Journal of Fluids and Structures*, 57:229–246, aug 2015. ISSN 0889-9746. doi: 10.1016/J.JFLUIDSTRUCTS.2015.06.017. URL https://www.sciencedirect.com/science/article/pii/S0889974615001565?via{%}3Dihub.

[90] Adel Shams, Valentina Lopresto, and Maurizio Porfiri. Modeling fluid-structure interactions during impact loading of water-backed panels. *Composite Structures*, 171:576–590, jul 2017. ISSN 0263-8223. doi: 10.1016/J.COMPSTRUCT.2017.02.098. URL https://www-sciencedirect-com.tudelft.idm.oclc.org/science/article/pii/S0263822316327428?{_}rdoc=1{&}{_}fmt=high{&}{_}origin=gateway{&}{_}docanchor={&}md5=b8429449ccfc9c30159a5f9aeaa92ffb{#}f0045.

[91] Ida M. Strand and Odd M. Faltinsen. Linear sloshing in a 2D rectangular tank with a flexible sidewall. *Journal of Fluids and Structures*, 73:70–81, aug 2017. ISSN 10958622. doi: 10.1016/j.jfluidstructs.2017.06.005. URL https://www-sciencedirect-com.tudelft.idm.oclc.org/science/article/pii/S0889974617300038?{_}rdoc=1{&}{_}fmt=high{&}{_}origin=gateway{&}{_}docanchor={&}md5=b8429449ccfc9c30159a5f9aeaa92ffb.

[92] Kenji Takizawa, Tayfun E. Tezduyar, Joseph Boben, Nikolay Kostov, Cody Boswell, and Austin Buscher. Fluid-structure interaction modeling of clusters of spacecraft parachutes with modified geometric porosity. *Computational Mechanics*, 2013. ISSN 01787675. doi: 10.1007/s00466-013-0880-5.

[93] Pieter Maljaars, Laurette Bronswijk, Jaap Windt, Nicola Grasso, and Mirek Kaminski. Experimental Validation of Fluid–Structure Interaction Computations of Flexible Composite Propellers in Open Water Conditions Using BEM-FEM and RANS-FEM Methods. *Journal of Marine Science and Engineering*, 6(2):51, 2018.

[94] Joris Degroote, Peter Bruggeman, Robby Haelterman, and Jan Vierendeels. Stability of a coupling technique for partitioned solvers in FSI applications. *Computers & Structures*, 86(23-24):2224–2234, dec 2008. ISSN 0045-7949. doi: 10.1016/J.COMPSTRUC.2008.05.005. URL https://www.sciencedirect.com/science/article/pii/S0045794908001466{#}bib22.

[95] A.H. van Zuijlen. *Fluid-structure interaction simulations: Efficient higher order time integration of partitioned systems*. PhD thesis, 2006. URL https://repository.tudelft.nl/islandora/object/uuid:fd466357-7890-45bd-b199-3df64df2e6d7?collection=research.

[96] Björn Hübner, Elmar Walhorn, and Dieter Dinkler. A monolithic approach to fluid–structure interaction using space–time finite elements. *Computer Methods in Applied Mechanics and Engineering*, 193(23-26):2087–2104, jun 2004. ISSN 0045-7825. doi: 10.1016/J.CMA.2004.01.024. URL https://www.sciencedirect.com/science/article/pii/S0045782504000696.

[97] A. de Boer, A. H. van Zuijlen, and H. Bijl. Review of coupling methods for non-matching meshes. *Computer Methods in Applied Mechanics and Engineering*, 196(8):1515–1525, jan 2007. ISSN 00457825. doi: 10.1016/j.cma.2006.03.017. URL https://www.sciencedirect.com/science/article/pii/S0045782506002817.

[98] Norbert Hosters, Jan Helmig, Atanas Stavrev, Marek Behr, and Stefanie Elgeti. Fluid–structure interaction with NURBS-based coupling. *Computer Methods in Applied Mechanics and Engineering*, 332:520–539, apr 2018. ISSN 00457825. doi: 10.1016/j.cma.2018.01.003. URL https://www.sciencedirect.com/science/article/pii/S0045782518300057.

[99] R. Mittal, H. Dong, M. Bozkurttas, F. M. Najjar, A. Vargas, and A. von Loebbecke. A versatile sharp interface immersed boundary method for incompressible flows with complex boundaries. *Journal of Computational Physics*, 2008. ISSN 00219991. doi: 10.1016/j.jcp.2008.01.028.

[100] A. de Boer, A. H. van Zuijlen, and H. Bijl. Radial basis functions for interface interpolation and mesh deformation. In *Lecture Notes in Computational Science and Engineering*, volume 71, pages 143–178. Springer, Berlin, Heidelberg, 2010. ISBN 9783642033438. doi: 10.1007/978-3-642-03344-5_6. URL http://link.springer.com/10.1007/978-3-642-03344-5{_}6.

[101] K. Stein, T. Tezduyar, and R. Benney. Mesh Moving Techniques for Fluid-Structure Interactions With Large Displacements. *Journal of Applied Mechanics*, 2003. ISSN 00218936. doi: 10.1115/1.1530635.

[102] Alexander Shamanskiy, Michael Gfrerer, and Bernd Simeon. Isogeometric Parametrization Inspired by Large Elastic Deformation. oct 2018. URL http://arxiv.org/abs/1810.12425.

[103] S. Lipton, J. A. Evans, Y. Bazilevs, T. Elguedj, and T. J.R. Hughes. Robustness of isogeometric structural discretizations under severe mesh distortion. *Computer Methods in Applied Mechanics and Engineering*, 199(5-8):357–373, jan 2010. ISSN 00457825. doi: 10.1016/j.cma.2009.01.022. URL https://www-sciencedirect-com.tudelft.idm.oclc.org/science/article/pii/S0045782509000346.

[104] J. N. Reddy. *An Introduction to Nonlinear Finite Element Analysis, 2nd Edn.* Oxford University Press, oct 2014. ISBN 9780199641758. doi: 10.1093/acprof:oso/9780199641758.001.0001. URL http://www.oxfordscholarship.com/view/10.1093/acprof:oso/9780199641758.001.0001/acprof-9780199641758.

[105] Martin H. (Martin Howard) Sadd. *Elasticity : theory, applications, and numerics.* Elsevier/Academic Press, 2009. ISBN 0080922414. URL https://books.google.nl/books?id=Kl7wLSF4730C{&}dq=elasticity+theory+applications+sadd{&}lr={&}source=gbs{_}navlinks{_}s.

[106] Pijush K Kundu, IM Cohen, and HH Hu. Fluid mechanics. 2004. *Elsevier Academic Press, San Diego). Two-and three-dimensional self-sustained flow oscillations*, 307:471–476, 2008.

[107] Y. Bazilevs, V. M. Calo, T. J. R. Hughes, and Y. Zhang. Isogeometric fluid-structure interaction: Theory, algorithms, and computations. *Computational Mechanics*, 43(1):3–37, dec 2008. ISSN 01787675. doi: 10.1007/s00466-008-0315-x. URL http://link.springer.com/10.1007/s00466-008-0315-x.

[108] Knut Nordanger, Adil Rasheed, Knut Morten Okstad, Arne Morten Kvarving, Runar Holdahl, and Trond Kvamsdal. Numerical benchmarking of fluid–structure interaction: An isogeometric finite element approach. *Ocean Engineering*, 124:324–339, sep 2016. ISSN 0029-8018. doi: 10.1016/J.OCEANENG.2016.07.018. URL https://www.sciencedirect.com/science/article/pii/S0029801816302591.

[109] Peter Nørtoft Nielsen, Allan Roulund Gersborg, Jens Gravesen, and Niels Leergaard Pedersen. Discretizations in isogeometric analysis of Navier–Stokes flow. *Computer Methods in Applied Mechanics and Engineering*, 200(45-46):3242–3253, oct 2011. ISSN 0045-7825. doi: 10.1016/J.CMA.2011.06.007. URL https://www.sciencedirect.com/science/article/pii/S0045782511002258.

[110] Michael Eckert. *The dawn of fluid dynamics: a discipline between science and technology.* John Wiley & Sons, 2007.

[111] G. K Batchelor. An Introduction to Fluid Dynamics, 1967. ISSN 00319228.

[112] Harold Rupert Vallentine. *Applied Hydrodynamics.* Butterworth, 1 edition, 1967.

[113] James Stewart. *Calculus Early Transcendentals.* 2010. ISBN 978-0-495-01166-8. doi: 978-0-495-01166-8.

[114] JD Anderson Jr. Some reflections on the history of fluid dynamics. In R.W. Johnson, editor, *The Handbook of Fluid Dynamics*, chapter 2, pages 26–36. CRC Press, Boca Raton, Fla, USA, 1998.

[115] Bert Jüttler, Ulrich Langer, Angelos Mantzaflaris, Stephen E. Moore, and Walter Zulehner. Geometry + Simulation Modules: Implementing Isogeometric Analysis. *PAMM*, 14(1):961–962, dec 2014. ISSN 16177061. doi: 10.1002/pamm.201410461. URL http://doi.wiley.com/10.1002/pamm.201410461.

[116] Carl De Boor. On calculating with B-splines. *Journal of Approximation theory*, 6(1):50–62, 1972.

[117] Maurice G Cox. The numerical evaluation of B-splines. *IMA Journal of Applied Mathematics*, 10 (2):134–149, 1972.

[118] Leslie Piegl and Wayne Tiller. A Menagerie of Rational B-Spline Circles. *IEEE Computer Graphics and Applications*, 1989. ISSN 02721716. doi: 10.1109/38.35537.

[119] C. W. Lim, C. M. Wang, and S. Kitipornchai. Timoshenko curved beam bending solutions in terms of Euler-Bernoulli solutions. *Archive of Applied Mechanics (Ingenieur Archiv)*, 67(3):179–190, feb 1997. ISSN 0939-1533. doi: 10.1007/s004190050110. URL http://link.springer.com/10.1007/s004190050110.

[120] Mohamad S. Qatu. Theories and analyses of thin and moderately thick laminated composite curved beams. *International Journal of Solids and Structures*, 30(20):2743–2756, jan 1993. ISSN 0020-7683. doi: 10.1016/0020-7683(93)90152-W. URL https://www.sciencedirect.com/science/article/pii/002076839390152W.

[121] Sara Almstedt and Puria Safari Hesari. Isogeometric analysis of curved beams and thin shells. Master's thesis, 2017.

[122] A Segal and Fred Vermolen. *Numerical methods in scientific computing.* VSSD, 2008.

[123] Peter Wriggers. *Nonlinear finite element methods.* 2008. ISBN 9783540710004. doi: 10.1007/978-3-540-71001-1.

[124] René de Borst, Mike A. Crisfield, Joris J.C. Remmers, and Clemens V. Verhoosel. *Non-Linear Finite Element Analysis of Solids and Structures: Second Edition.* 2012. ISBN 9780470666449. doi: 10.1002/9781118375938.

[125] Dominik Schillinger, Shaikh J. Hossain, and Thomas J.R. Hughes. Reduced Bézier element quadrature rules for quadratic and cubic splines in isogeometric analysis. *Computer Methods in Applied Mechanics and Engineering*, 277:1–45, aug 2014. ISSN 0045-7825. doi: 10.1016/J.CMA.2014.04.008. URL https://www.sciencedirect.com/science/article/pii/S0045782514001339.

[126] Lam H. Nguyen and Dominik Schillinger. A collocated isogeometric finite element method based on Gauss–Lobatto Lagrange extraction of splines. *Computer Methods in Applied Mechanics and Engineering*, 316:720–740, apr 2017. ISSN 0045-7825. doi: 10.1016/J.CMA.2016.09.036. URL https://www.sciencedirect.com/science/article/pii/S0045782516312312{#}br000165.

[127] Milton Abramowitz, Irene A. Stegun, and David Miller. Handbook of Mathematical Functions With Formulas, Graphs and Mathematical Tables (National Bureau of Standards Applied Mathematics Series No. 55). *Journal of Applied Mechanics*, 1965. ISSN 00218936. doi: 10.1115/1.3625776.

[128] Cornelis Vuik, P Van Beek, F Vermolen, and J Van Kan. *Numerical Methods for Ordinary differential equations*. VSSD, 2007.

[129] Y. M. Xie. An assessment of time integration schemes for non-linear dynamic equations. *Journal of Sound and Vibration*, 1996. ISSN 0022460X. doi: 10.1006/jsvi.1996.0190.

[130] M A Dokainish and K Subbaraj. A survey of direct time-integration methods in computational structural dynamics—I. Explicit methods. *Computers & Structures*, 32(6):1371–1386, 1989. ISSN 0045-7949. doi: https://doi.org/10.1016/0045-7949(89)90314-3. URL http://www.sciencedirect.com/science/article/pii/0045794989903143.

[131] K. Subbaraj and M. A. Dokainish. A survey of direct time-integration methods in computational structural dynamics-II. Implicit methods. *Computers and Structures*, 1989. ISSN 00457949. doi: 10.1016/0045-7949(89)90315-5.

[132] Klaus-Jürgen Bathe and Mirza M. Irfan Baig. On a composite implicit time integration procedure for nonlinear dynamics. *Computers & Structures*, 83(31-32):2513–2524, dec 2005. ISSN 0045-7949. doi: 10.1016/J.COMPSTRUC.2005.08.001. URL https://www.sciencedirect.com/science/article/pii/S0045794905002920.

[133] J. C. Butcher. *Numerical Methods for Ordinary Differential Equations*. 2016. ISBN 9781119121534. doi: 10.1002/9781119121534.

[134] Ernst Hairer, Syvert P. Nørsett, and Gerhard Wanner. *Solving Ordinary Differential Equations I. Nonstiff Problems*, volume 8. Springer-Verlag Berlin Heidelberg, 2 edition, 1993. ISBN 978-3-540-56670-0. doi: 10.1007/978-3-540-78862-1.

[135] J. C. Butcher. On Runge-Kutta processes of high order. *Journal of the Australian Mathematical Society*, 1964. ISSN 14468107. doi: 10.1017/S1446788700023387.

[136] Wilhelm Kutta. Beitrag zur näherungweisen Integration totaler Differentialgleichungen. 1901.

[137] Alex Kanevsky, Mark H. Carpenter, David Gottlieb, and Jan S. Hesthaven. Application of implicit–explicit high order Runge–Kutta methods to discontinuous-Galerkin schemes. *Journal of Computational Physics*, 225(2):1753–1781, aug 2007. ISSN 0021-9991. doi: 10.1016/J.JCP.2007.02.021. URL https://www.sciencedirect.com/science/article/pii/S0021999107000861.

[138] N.M. Newmark. A Method of Computation for Structural Dynamics. *J. Engng. Mech.*, 1959. ISSN 0044-7951. doi: 0.1016/j.compgeo.2015.08.008.

[139] E. L. Wilson, I. Farhoomand, and K. J. Bathe. Nonlinear Dynamic Analysis of Complex Structures. *Earthquake Engineering and Structural Dynamics*, 1(3):241–252, 1973. ISSN 00988847. doi: 10.1191/030913201680191745. URL http://www.scopus.com/inward/record.url?eid=2-s2.0-0015556840{&}partnerID=tZOtx3y1.

[140] Klaus-Jürgen Bathe. Conserving energy and momentum in nonlinear dynamics: A simple implicit time integration scheme. *Computers & Structures*, 85(7-8):437–445, apr 2007. ISSN 0045-7949. doi: 10.1016/J.COMPSTRUC.2006.09.004. URL https://www.sciencedirect.com/science/article/pii/S0045794906003099{#}bib1.

[141] K. J. Bathe. On reliable finite element methods for extreme loading conditions. In *NATO Security through Science Series C: Environmental Security*, 2007. ISBN 1402056540. doi: 10.1007/978-1-4020-5656-7_3.

[142] Klaus-Jürgen Bathe and Gunwoo Noh. Insight into an implicit time integration scheme for structural dynamics. *Computers & Structures*, 98-99:1–6, may 2012. ISSN 0045-7949. doi: 10.1016/J.COMPSTRUC.2012.01.009. URL https://www.sciencedirect.com/science/article/pii/S0045794912000107.

[143] Gunwoo Noh and Klaus-Jürgen Bathe. Further insights into an implicit time integration scheme for structural dynamics. *Computers & Structures*, 202:15–24, jun 2018. ISSN 0045-7949. doi: 10.1016/J.COMPSTRUC.2018.02.007. URL https://www.sciencedirect.com/science/article/pii/S0045794917315663.

[144] J.A. Cottrell, A. Reali, and Y. Bazilevs. Isogeometric analysis of structural vibrations. *Computer Methods in Applied Mechanics and Engineering*, 195(41-43):5257–5296, aug 2006. ISSN 0045-7825. doi: 10.1016/J.CMA.2005.09.027. URL https://www.sciencedirect.com/science/article/pii/S0045782505005451.

[145] Ivo Babuska and J. Tinsley Oden. Verification and validation in computational engineering and science: Basic concepts. *Computer Methods in Applied Mechanics and Engineering*, 2004. ISSN 00457825. doi: 10.1016/j.cma.2004.03.002.

[146] Ben H. Thacker, Scott W. Doebling, Francois M. Hemez, Mark C. Anderson, Jason E. Pepin, and Edward a. Rodriguez. Concepts of Model Verification and Validation. *Concepts of Model Verification and Validation*, 2004. doi: 10.2172/835920.

[147] Ted Belytschko, Henryk Stolarski, Wing Kam Liu, Nicholas Carpenter, and Jame S.J. Ong. Stress projection for membrane and shear locking in shell finite elements. *Computer Methods in Applied Mechanics and Engineering*, 1985. ISSN 00457825. doi: 10.1016/0045-7825(85)90035-0.

[148] Stefan Turek and Jaroslav Hron. Proposal for numerical benchmarking of fluid-structure interaction between an elastic object and laminar incompressible flow. In *Fluid-structure interaction*, pages 371–385. Springer, 2006.

[149] Patrick J. Roache. Code Verification by the Method of Manufactured Solutions. *Journal of Fluids Engineering*, 2002. ISSN 00982202. doi: 10.1115/1.1436090.

[150] R.C. Hibbeler. *Mechanics of Materials*. Pearson, 2011. ISBN 9780136022305. doi: 10.1017/CBO9781107415324.004.

[151] Li-Qun Chen and Hu Ding. Two nonlinear models of a transversely vibrating string. *Archive of Applied Mechanics*, 78(5):321–328, may 2008. ISSN 0939-1533. doi: 10.1007/s00419-007-0164-7. URL http://link.springer.com/10.1007/s00419-007-0164-7.

[152] G. C. Tsiatas and J. T. Katsikadelis. Large deflection analysis of elastic space membranes. *International Journal for Numerical Methods in Engineering*, 65(2):264–294, jan 2006. ISSN 0029-5981. doi: 10.1002/nme.1499. URL http://doi.wiley.com/10.1002/nme.1499.

[153] Javier Bonet and Richard D. Wood. *Nonlinear continuum mechanics for finite element analysis*. Cambridge University Press, 1997. ISBN 052157272X. URL https://books.google.nl/books?id=ORmLdrq1fI8C{&}dq=Nonlinear+continuum+mechanics+for+finite+element+analysis{&}lr={&}source=gbs{_}navlinks{_}s.

[154] Vladimir G Ivancevic and Tijana T Ivancevic. *Applied differential geometry: a modern introduction*. World Scientific, 2007.

A | Structural Derivations

A.1 Von Kármán Strains

If the strains of a material volume in normal directions are small, i.e.

$$\frac{\partial u}{\partial x}, \frac{\partial v}{\partial y}, \frac{\partial w}{\partial z} \sim \mathcal{O}(\varepsilon),$$

And if furthermore the in-plane shear effects are also small, i.e.

$$\frac{\partial u}{\partial y}, \frac{\partial v}{\partial x} \sim \mathcal{O}(\varepsilon),$$

Then all terms with $\mathcal{O}(\varepsilon^2)$ vanish from the formulations. Furthermore, for moderate rotations, the following terms have a non-negligible contribution compared to $\mathcal{O}(\varepsilon)$:

$$\left(\frac{\partial w}{\partial x}\right)^2, \left(\frac{\partial w}{\partial x}\right)^2, \left(\frac{\partial w}{\partial x}\frac{\partial w}{\partial y}\right).$$

These order have the following consequences for the Green strain tensor:

$$\varepsilon_{11} = \frac{\partial u}{\partial x} + \frac{1}{2}\left[\cancel{\left(\frac{\partial u}{\partial x}\right)^2}^{\mathcal{O}(\varepsilon^2)} + \cancel{\left(\frac{\partial v}{\partial x}\right)^2}^{\mathcal{O}(\varepsilon^2)} + \left(\frac{\partial w}{\partial x}\right)^2\right] \approx \frac{\partial u}{\partial x} + \frac{1}{2}\left(\frac{\partial w}{\partial x}\right)^2 + \mathcal{O}(\varepsilon^2)$$

$$\varepsilon_{12} = \frac{1}{2}\left[\frac{\partial u}{\partial y} + \frac{\partial v}{\partial x} + \cancel{\frac{\partial u}{\partial x}\frac{\partial u}{\partial y}}^{\mathcal{O}(\varepsilon^2)} + \cancel{\frac{\partial v}{\partial x}\frac{\partial v}{\partial y}}^{\mathcal{O}(\varepsilon^2)} + \frac{\partial w}{\partial x}\frac{\partial w}{\partial y}\right] \approx \frac{1}{2}\left[\frac{\partial u}{\partial y} + \frac{\partial v}{\partial x} + \frac{\partial w}{\partial x}\frac{\partial w}{\partial y}\right] + \mathcal{O}(\varepsilon^2)$$

$$\varepsilon_{13} = \frac{1}{2}\left[\frac{\partial u}{\partial z} + \frac{\partial w}{\partial x} + \cancel{\frac{\partial u}{\partial x}\frac{\partial u}{\partial z}}^{\mathcal{O}(\varepsilon)} + \cancel{\frac{\partial v}{\partial x}\frac{\partial v}{\partial z}}^{\mathcal{O}(\varepsilon)} + \cancel{\frac{\partial w}{\partial x}\frac{\partial w}{\partial z}}^{\mathcal{O}(\varepsilon)}\right]^{\mathcal{O}(\varepsilon)} \approx \frac{1}{2}\left[\frac{\partial u}{\partial z} + \frac{\partial w}{\partial x}\right] + \mathcal{O}(\varepsilon)$$

$$\varepsilon_{22} = \frac{\partial v}{\partial y} + \frac{1}{2}\left[\cancel{\left(\frac{\partial u}{\partial y}\right)^2}^{\mathcal{O}(\varepsilon^2)} + \cancel{\left(\frac{\partial v}{\partial y}\right)^2}^{\mathcal{O}(\varepsilon^2)} + \left(\frac{\partial w}{\partial y}\right)^2\right] \approx \frac{\partial v}{\partial y} + \frac{1}{2}\left(\frac{\partial w}{\partial y}\right)^2 + \mathcal{O}(\varepsilon^2)$$

$$\varepsilon_{23} = \frac{1}{2}\left[\frac{\partial v}{\partial z} + \frac{\partial w}{\partial y} + \cancel{\frac{\partial u}{\partial y}\frac{\partial u}{\partial z}}^{\mathcal{O}(\varepsilon)} + \cancel{\frac{\partial v}{\partial y}\frac{\partial v}{\partial z}}^{\mathcal{O}(\varepsilon)} + \cancel{\frac{\partial w}{\partial y}\frac{\partial w}{\partial z}}^{\mathcal{O}(\varepsilon)}\right]^{\mathcal{O}(\varepsilon)} \approx \frac{1}{2}\left[\frac{\partial v}{\partial z} + \frac{\partial w}{\partial y}\right] + \mathcal{O}(\varepsilon)$$

$$\varepsilon_{33} = \frac{\partial w}{\partial z} + \frac{1}{2}\left[\cancel{\left(\frac{\partial u}{\partial z}\right)^2}^{\mathcal{O}(\varepsilon^2)} + \cancel{\left(\frac{\partial v}{\partial z}\right)^2}^{\mathcal{O}(\varepsilon^2)} + \cancel{\left(\frac{\partial w}{\partial z}\right)^2}^{\mathcal{O}(\varepsilon^2)}\right]^{\mathcal{O}(\varepsilon^2)} \approx \frac{\partial w}{\partial z} + \mathcal{O}(\varepsilon^2)$$

Plugging in the expressions for u, v, w and performing some mathematical operations yields the Von Kármán strains:

$$\begin{aligned}
\varepsilon_{11} &= \frac{\partial u_0}{\partial x} - z\frac{\partial^2 w_0}{\partial x^2} + \boxed{\frac{1}{2}\left(\frac{\partial w_0}{\partial x}\right)^2} \\
\varepsilon_{12} &= \frac{1}{2}\left[\frac{\partial u_0}{\partial y} - z\frac{\partial^2 w_0}{\partial x \partial y} + \frac{\partial v_0}{\partial x} - z\frac{\partial^2 w_0}{\partial x \partial y} + \frac{\partial w_0}{\partial x}\frac{\partial w_0}{\partial y}\right] = \frac{1}{2}\left[\frac{\partial u_0}{\partial y} + \frac{\partial v_0}{\partial x} - 2z\frac{\partial^2 w_0}{\partial x \partial y} + \boxed{\frac{\partial w_0}{\partial x}\frac{\partial w_0}{\partial y}}\right] \\
\varepsilon_{13} &= \frac{1}{2}\left[-z\frac{\partial}{\partial z}\left(\frac{\partial w_0}{\partial x}\right) - \frac{\partial w_0}{\partial x} + \frac{\partial w_0}{\partial x}\right] = \frac{1}{2}\left[-z\frac{\partial}{\partial x}\left(\cancel{\frac{\partial w_0}{\partial z}}^{0}\right) - \frac{\partial w_0}{\partial x} + \frac{\partial w_0}{\partial x}\right] = 0 \\
\varepsilon_{22} &= \frac{\partial v_0}{\partial y} - z\frac{\partial^2 w_0}{\partial y^2} + \boxed{\frac{1}{2}\left(\frac{\partial w_0}{\partial y}\right)^2} \\
\varepsilon_{23} &= \frac{1}{2}\left[-z\frac{\partial}{\partial z}\left(\frac{\partial w_0}{\partial y}\right) - \frac{\partial w_0}{\partial y} + \frac{\partial w_0}{\partial y}\right] = \frac{1}{2}\left[-z\frac{\partial}{\partial y}\left(\cancel{\frac{\partial w_0}{\partial z}}^{0}\right) - \frac{\partial w_0}{\partial y} + \frac{\partial w_0}{\partial y}\right] = 0 \\
\varepsilon_{33} &= \frac{\partial w_0}{\partial z} = 0
\end{aligned} \tag{A.1}$$

Note that the derivatives of u_0 and v_0 with respect to z are zero as these are the in-plane mid-plane displacements. Furthermore, the $\boxed{\text{boxed}}$ terms are the non-linear strain contributions. Now, the Green strain tensor $\underline{\underline{\boldsymbol{E}}}^G$ can be simplified to the Von Kármán strain tensor $\underline{\underline{\boldsymbol{E}}}^K$ (in the latter $\underline{\underline{\boldsymbol{E}}}$). Thus, let the strain and curvature tensors ($\underline{\underline{\boldsymbol{\varepsilon}}}$ and $\underline{\underline{\boldsymbol{\kappa}}}$, respectively) be defined by:

$$\begin{aligned}
\varepsilon_{\alpha\beta} &= \frac{\partial u^0_\alpha}{\partial x_\beta} + \frac{\partial u^0_\beta}{\partial x_\alpha} + \frac{\partial u^0_\alpha}{\partial x_\beta}\frac{\partial u^0_\beta}{\partial x_\alpha} && = \frac{1}{2}\left(\nabla \boldsymbol{u} + (\nabla \boldsymbol{u})^T + (\nabla \boldsymbol{u})(\nabla \boldsymbol{u})^T\right) \quad \text{with } \boldsymbol{u}^T = [u^0_1, u^0_2] \\
\kappa_{\alpha\beta} &= \frac{\partial^2 u^0_3}{\partial x_\alpha \partial x_\beta} && = \nabla(\nabla u^0_3)
\end{aligned}$$

Here, $u^0_i(\boldsymbol{x}^0)$ denotes the deformation of the mid-plane. Furthermore, the gradient operators only work on the xy-plane, i.e. $\nabla(\cdot) = \left[\frac{\partial \cdot}{\partial x}, \frac{\partial \cdot}{\partial x}\right]^T$. Then,

$$\underline{\underline{\boldsymbol{E}}}^K = \underline{\underline{\boldsymbol{\varepsilon}}} + x^0_3 \underline{\underline{\boldsymbol{\kappa}}}$$

Or,

$$\begin{bmatrix} E_{11} & E_{12} \\ E_{21} & E_{22} \end{bmatrix} = \begin{bmatrix} \varepsilon_{11} & \varepsilon_{12} \\ \varepsilon_{21} & \varepsilon_{22} \end{bmatrix} + x^0_3 \begin{bmatrix} \kappa_{11} & \kappa_{12} \\ \kappa_{21} & \kappa_{22} \end{bmatrix}$$

A.2 Derivation of the Euler-Bernoulli Beam Equations

For the derivation of the Euler-Bernoulli beam equation, only the xz-plane is considered and hence all derivatives with respect to y are equal to zero. This implies that the Von Kármán strains from equation (A.1) simplify to:

$$\varepsilon_{11} = \frac{\partial u_0}{\partial x} - z\frac{\partial^2 w_0}{\partial x^2} + \frac{1}{2}\left(\frac{\partial w_0}{\partial x}\right)^2$$

Furthermore, the virtual strains become:

$$\delta\varepsilon_{11} = \frac{\partial \delta u_0}{\partial x} - z\frac{\partial^2 \delta w_0}{\partial x^2} + \frac{\partial w_0}{\partial x}\frac{\partial \delta w_0}{\partial x}$$

From this expression, we see that the internal virtual work of the beam becomes:

$$\begin{aligned}
\delta W_I &= \int_\Omega \sigma : \delta\varepsilon \, \mathrm{d}\Omega, \\
&= \int_\Omega \sigma_{11}\delta\varepsilon_{11} \, \mathrm{d}\Omega, \\
&= \int_\Omega \sigma_{11}\left(\frac{\partial \delta u_0}{\partial x} - z\frac{\partial^2 \delta w_0}{\partial x^2} + \frac{\partial w_0}{\partial x}\frac{\partial \delta w_0}{\partial x}\right) \mathrm{d}\Omega, \\
&= \int_0^L \int_{-\frac{b}{2}}^{\frac{b}{2}} N_{11}\frac{\partial \delta u_0}{\partial x} - M_{11}\frac{\partial^2 \delta w_0}{\partial x^2} + N_{11}\frac{\partial w_0}{\partial x}\frac{\partial \delta w_0}{\partial x} \, \mathrm{d}x\mathrm{d}y. \qquad \text{(A.2)}
\end{aligned}$$

Here, N_{11} and M_{11} are defined as the zeroth and first moment of the stress over the height of the profile, i.e.

$$\begin{aligned}
N_{11} &= \int_{-\frac{h}{2}}^{\frac{h}{2}} \sigma_{11} \, \mathrm{d}z, \\
M_{11} &= \int_{-\frac{h}{2}}^{\frac{h}{2}} z\sigma_{11} \, \mathrm{d}z.
\end{aligned}$$

In fact, they represent the axial force and the bending moment at any point in the xy-plane. In order to derive the governing PDEs for the Euler-Bernoulli beam with small deformations, the integral form of the internal work needs to be written as a product of δu_0 and δw_0. Hence, using partial integration on equation (A.2) results in:

$$
\begin{aligned}
(\dots) &= \int_0^L \int_{-\frac{b}{2}}^{\frac{b}{2}} \frac{\partial}{\partial x}\left(N_{11}\delta u_0\right) - \frac{\partial N_{11}}{\partial x}\delta u_0 - \left[\frac{\partial}{\partial x}\left(M_{11}\frac{\partial \delta w_0}{\partial x}\right) - \frac{\partial M_{11}}{\partial x}\frac{\partial \delta w_0}{\partial x}\right] + \frac{\partial}{\partial x}\left(N_{11}\frac{\partial w_0}{\partial x}\delta w_0\right) + \\
&\quad - \frac{\partial N_{11}}{\partial x}\frac{\partial w_0}{\partial x}\delta w_0 - N_{11}\frac{\partial^2 w_0}{\partial x^2}\delta w_0 \,\mathrm{d}x\mathrm{d}y, \\
&= \int_0^L \int_{-\frac{b}{2}}^{\frac{b}{2}} -\frac{\partial N_{11}}{\partial x}\delta u_0 + \left[\frac{\partial}{\partial x}\left(\frac{\partial M_{11}}{\partial x}\delta w_0\right) - \frac{\partial^2 M_{11}}{\partial x^2}\delta w_0\right] - \frac{\partial N_{11}}{\partial x}\frac{\partial w_0}{\partial x}\delta w_0 - N_{11}\frac{\partial^2 w_0}{\partial x^2}\delta w_0 \,\mathrm{d}x\mathrm{d}y \\
&\quad + \left[\int_{-\frac{b}{2}}^{\frac{b}{2}} N_{11}\delta u_0 - M_{11}\frac{\partial \delta w_0}{\partial x} + N_{11}\frac{\partial w_0}{\partial x}\delta w_0 \,\mathrm{d}y\right]_0^L, \\
&= \int_0^L \int_{-\frac{b}{2}}^{\frac{b}{2}} -\frac{\partial N_{11}}{\partial x}\delta u_0 - \frac{\partial^2 M_{11}}{\partial x^2}\delta w_0 - \frac{\partial N_{11}}{\partial x}\frac{\partial w_0}{\partial x}\delta w_0 - N_{11}\frac{\partial^2 w_0}{\partial x^2}\delta w_0 \,\mathrm{d}x\mathrm{d}y \\
&\quad + \left[\int_{-\frac{b}{2}}^{\frac{b}{2}} N_{11}\delta u_0 - M_{11}\frac{\partial \delta w_0}{\partial x} + \frac{\partial M_{11}}{\partial x}\delta w_0 + N_{11}\frac{\partial w_0}{\partial x}\delta w_0 \,\mathrm{d}y\right]_0^L, \\
&= b\int_0^L -\frac{\partial N_{11}}{\partial x}\delta u_0 - \frac{\partial^2 M_{11}}{\partial x^2}\delta w_0 - \frac{\partial N_{11}}{\partial x}\frac{\partial w_0}{\partial x}\delta w_0 - N_{11}\frac{\partial^2 w_0}{\partial x^2}\delta w_0 \,\mathrm{d}x \\
&\quad + b\left[N_{11}\delta u_0 - M_{11}\frac{\partial \delta w_0}{\partial x} + \frac{\partial M_{11}}{\partial x}\delta w_0 + N_{11}\frac{\partial w_0}{\partial x}\delta w_0\right]_0^L,
\end{aligned}
$$

Where the last equality holds because N_{11} and M_{11} are assumed to be not depending on the y-direction. Likewise, δu_0 and δw_0 do not depend on the y-direction. Now, the virtual work of the external forces can be determined. Suppose the beam is subject to a transversal pressure on the top ($p_t(x)$) and on the bottom ($p_b(x)$) and a longitudinal traction force on the top ($t_t(x)$) and on the bottom ($t_b(x)$), as well. Furthermore, a hydrostatic foundation is applied on the beam, denoted by $-\rho g w$. Then, the virtual work of these loads becomes:

$$
\begin{aligned}
\delta W_E &= -b\int_0^L p_t \delta w\left(x, y, \frac{h}{2}\right) + p_b \delta w\left(x, y, -\frac{h}{2}\right) \\
&\quad + t_t \delta u\left(x, y, \frac{h}{2}\right) + t_b \delta u\left(x, y, \frac{h}{2}\right) - \rho g w \delta w(x, y, 0)\,\mathrm{d}x \\
&= -b\int_0^L p_t \delta w_0 + p_b \delta w_0 \\
&\quad + t_t\left(\delta u_0 - \frac{h}{2}\frac{\partial \delta w_0}{\partial x}\right) + t_b\left(\delta u_0 + \frac{h}{2}\frac{\partial \delta w_0}{\partial x}\right) - b\rho g w_0 \delta w_0 \,\mathrm{d}x \\
&= -b\int_0^L \left(p_t + p_b - \frac{h}{2}\frac{\partial t_t}{\partial x} + \frac{h}{2}\frac{\partial t_b}{\partial x}\right)\delta w_0 + \left(t_t + t_b\right)\delta u_0 - b\rho g w_0 \delta w_0 \,\mathrm{d}x \\
&\quad - \left[\left(-\frac{h}{2}q_t + \frac{h}{2}q_b\right)\delta w_0\right]_0^L
\end{aligned}
$$

Lastly, in order to get the dynamic equation of the Euler beam, the kinetic energy should also be involved. This reads,

$$\delta K = b \int_0^L \rho \left(\dot{u}\delta\dot{u} + \dot{w}\delta\dot{w} \right) \, \mathrm{d}x$$

In order to obtain the equations of motion, Hamilton's principle from equation (3.10) is used. It is assumed that the virtual displacements are equal on time instances t_1 and t_2. Firstly, the integral of the kinetic energy δK over time becomes:

$$\begin{aligned}
\int_{t_1}^{t_2} \delta K \, \mathrm{d}t &= b \int_{t_1}^{t_2} \int_{-\frac{h}{2}}^{\frac{h}{2}} \int_0^L \rho \left[\dot{u}\delta\dot{u} + \dot{w}\delta\dot{w} \right] \mathrm{d}x\mathrm{d}z\mathrm{d}t \\
&= b \int_{t_1}^{t_2} \int_{-\frac{h}{2}}^{\frac{h}{2}} \int_0^L \rho \left[\left(\dot{u}_0 - z\frac{\partial \dot{w}_0}{\partial x} \right) \left(\delta\dot{u}_0 - z\frac{\partial \delta\dot{w}_0}{\partial x} \right) + \dot{w}_0\delta\dot{w}_0 \right] \mathrm{d}x\mathrm{d}z\mathrm{d}t \\
&= b \int_{t_1}^{t_2} \int_{-\frac{h}{2}}^{\frac{h}{2}} \int_0^L \rho \left[\left(\dot{u}_0\delta\dot{u}_0 - z\frac{\partial \dot{w}_0}{\partial x}\delta\dot{u}_0 - z\dot{u}_0\frac{\partial \delta\dot{w}_0}{\partial x} - z^2\frac{\partial \dot{w}_0}{\partial x}\frac{\partial \delta\dot{w}_0}{\partial x} \right) + \dot{w}_0\delta\dot{w}_0 \right] \mathrm{d}x\mathrm{d}z\mathrm{d}t \\
&= b \int_{t_1}^{t_2} \int_0^L \rho \left[\left(h\dot{u}_0\delta\dot{u}_0 - \frac{h^3}{12}\frac{\partial \dot{w}_0}{\partial x}\frac{\partial \delta\dot{w}_0}{\partial x} \right) + h\dot{w}_0\delta\dot{w}_0 \right] \mathrm{d}x\mathrm{d}t \\
&= -b \int_{t_1}^{t_2} \int_0^L \rho \left[\left(h\ddot{u}_0\delta u_0 - \frac{h^3}{12}\frac{\partial \ddot{w}_0}{\partial x}\frac{\partial \delta w_0}{\partial x} \right) + h\ddot{w}_0\delta w_0 \right] \mathrm{d}x\mathrm{d}t \\
&\quad + b \left[\int_0^L \rho \left(\dot{u}\delta u + \dot{w}\delta w - \frac{h^3}{12}\frac{\partial \dot{w}_0}{\partial x}\frac{\partial \delta w_0}{\partial x} \right) \right]_{t=t_1}^{t_2} \mathrm{d}x \qquad \text{(the } \dot{u}\delta u + \dot{w}\delta w \text{ part} \to 0\text{)} \\
&= -\int_{t_1}^{t_2} \left\{ \int_0^L \rho \left[\left(A\ddot{u}_0\delta u_0 - I\frac{\partial^2 \ddot{w}_0}{\partial x^2}\delta w_0 \right) + A\ddot{w}_0\delta w_0 \right] \mathrm{d}x + \rho \left[I\frac{\partial \ddot{w}_0}{\partial x}\delta w_0 \right]_0^L \right\} \mathrm{d}t
\end{aligned}$$

In the last equality, $A = bh$ and $I = bh^3/12$ and in the fore-last equality the initial and final conditions of the virtual displacements are set to zero. Now, Hamilton's principle becomes:

$$\begin{aligned}
\int_{t_1}^{t_2} \delta K - (\delta W_E + \delta W_I) \, \mathrm{d}t = \int_{t_1}^{t_2} \Bigg\{ & \int_0^L -\rho \left[A\ddot{u}_0\delta u_0 - I\frac{\partial^2 \ddot{w}_0}{\partial x^2}\delta w_0 + A\ddot{w}_0\delta w_0 \right] + b\frac{\partial N_{11}}{\partial x}\delta u_0 + b\frac{\partial^2 M_{11}}{\partial x^2}\delta w_0 \\
& + b\frac{\partial N_{11}}{\partial x}\frac{\partial w_0}{\partial x}\delta w_0 + bN_{11}\frac{\partial^2 w_0}{\partial x^2}\delta w_0 + b\left(p_t + p_b - \frac{h}{2}\frac{\partial t_t}{\partial x} + \frac{h}{2}\frac{\partial t_b}{\partial x} \right)\delta w_0 \\
& + b\left(t_t + t_b \right)\delta u_0 - b\rho g w_0 \delta w_0 \, \mathrm{d}x \\
& + \rho \left[I\frac{\partial \ddot{w}_0}{\partial x}\delta w_0 \right]_0^L - \left[bN_{11}\delta u_0 - bM_{11}\frac{\partial \delta w_0}{\partial x} + b\frac{\partial M_{11}}{\partial x}\delta w_0 \right]_0^L \Bigg\} \, \mathrm{d}t \\
= 0 &
\end{aligned}$$

From this principle, the equations of motion follow by collecting the terms multiplied by δu_0 and δw_0 separately from the domain integral.

$$\begin{aligned}
b\frac{\partial N_{11}}{\partial x} - \rho A\ddot{u}_0 + b(t_t + t_b) &= 0 \\
b\frac{\partial^2 M_{11}}{\partial x^2} + b\frac{\partial N_{11}}{\partial x}\frac{\partial w_0}{\partial x} + bN_{11}\frac{\partial^2 w_0}{\partial x^2} &= -\rho I\frac{\partial^2 \ddot{w}_0}{\partial x^2} + \rho A\ddot{w}_0 - b\left(p_t + p_b - \frac{h}{2}\frac{\partial t_t}{\partial x} + \frac{h}{2}\frac{\partial t_b}{\partial x} \right) + b\rho g w_0
\end{aligned} \tag{A.3}$$

Or, combining derivatives:

$$\begin{aligned} b\frac{\partial N_{11}}{\partial x} - \rho A\ddot{u}_0 + b(t_t + t_b) &= 0 \\ b\frac{\partial^2 M_{11}}{\partial x^2} + b\frac{\partial}{\partial x}\left(N_{11}\frac{\partial w_0}{\partial x}\right) &= -\rho I\frac{\partial^2 \ddot{w}_0}{\partial x^2} + \rho A\ddot{w}_0 - b\left(p_t + p_b - \frac{h}{2}\frac{\partial t_t}{\partial x} + \frac{h}{2}\frac{\partial t_b}{\partial x}\right) + b\rho g w_0 \end{aligned} \tag{A.4}$$

Furthermore, N_{11} and M_{11} are defined by:

$$\begin{aligned} N_{11} &= \int_{-\frac{h}{2}}^{\frac{h}{2}} E\left(\frac{\partial u_0}{\partial x} - z\frac{\partial^2 w_0}{\partial x^2} + \frac{1}{2}\left(\frac{\partial w_0}{\partial x}\right)^2\right) \mathrm{d}x = Eh\left(\frac{\partial u_0}{\partial x} + \frac{1}{2}\left(\frac{\partial w_0}{\partial x}\right)^2\right) \\ M_{11} &= \int_{-\frac{h}{2}}^{\frac{h}{2}} Ez\left(\frac{\partial u_0}{\partial x} - z\frac{\partial^2 w_0}{\partial x^2} + \frac{1}{2}\left(\frac{\partial w_0}{\partial x}\right)^2\right) \mathrm{d}x = -\frac{Eh^3}{12}\frac{\partial^2 w_0}{\partial x^2} \end{aligned}$$

As a result, the equations of motion become:

$$\begin{aligned} -EA\left(\frac{\partial^2 u_0}{\partial x^2} + \frac{\partial w_0}{\partial x}\frac{\partial^2 w_0}{\partial x^2}\right) + \rho A\ddot{u}_0 &= b(t_t + t_b) \\ -EA\left[\frac{\partial w_0}{\partial x}\left(\frac{\partial^2 u_0}{\partial x^2} + \frac{\partial w_0}{\partial x}\frac{\partial^2 w_0}{\partial x^2}\right) + \frac{\partial^2 w_0}{\partial x^2}\left(\frac{\partial u_0}{\partial x} + \frac{1}{2}\left(\frac{\partial w_0}{\partial x}\right)^2\right)\right] + EI\frac{\partial^4 w_0}{\partial x^4} & \\ -\rho I\frac{\partial^2 \ddot{w}_0}{\partial x^2} + \rho A\ddot{w}_0 &= b\left(p_t + p_b - \frac{h}{2}\frac{\partial t_t}{\partial x} + \frac{h}{2}\frac{\partial t_b}{\partial x}\right) - b\rho g w_0 \end{aligned}$$

Or, again, when combining derivatives:

$$\begin{aligned} -EA\left(\frac{\partial^2 u_0}{\partial x^2} + \frac{\partial w_0}{\partial x}\frac{\partial^2 w_0}{\partial x^2}\right) + \rho A\ddot{u}_0 &= b(t_t + t_b) \\ -EA\frac{\partial}{\partial x}\left[\left(\frac{\partial u_0}{\partial x} + \frac{1}{2}\left(\frac{\partial w_0}{\partial x}\right)^2\right)\frac{\partial w_0}{\partial x}\right] + EI\frac{\partial^4 w_0}{\partial x^4} & \\ -\rho I\frac{\partial^2 \ddot{w}_0}{\partial x^2} + \rho A\ddot{w}_0 &= b\left(p_t + p_b - \frac{h}{2}\frac{\partial t_t}{\partial x} + \frac{h}{2}\frac{\partial t_b}{\partial x}\right) - b\rho g w_0 \end{aligned} \tag{A.5}$$

Neglecting the rotary inertia term $\rho I\frac{\partial^2 \ddot{w}_0}{\partial x^2}$ and hydrostatic pressure $b\rho g w_0$, letting $p = b(p_t + p_b)$ and $t = b(t_t + t_b)$, this simplifies to:

$$\begin{aligned} -EA\left(\frac{\partial^2 u_0}{\partial x^2} + \frac{\partial w_0}{\partial x}\frac{\partial^2 w_0}{\partial x^2}\right) + \rho A\ddot{u}_0 &= t \\ -EA\frac{\partial}{\partial x}\left[\left(\frac{\partial u_0}{\partial x} + \frac{1}{2}\left(\frac{\partial w_0}{\partial x}\right)^2\right)\frac{\partial w_0}{\partial x}\right] + EI\frac{\partial^4 w_0}{\partial x^4} + \rho A\ddot{w}_0 &= p \end{aligned} \tag{A.6}$$

This is a result which can also be derived from the derivations by Reddy[104]. It represents the behaviour of the non-linear Euler-Bernoulli beam including membrane deformations, i.e. stretching. When horizontal deformations are neglected, the following result is obtained:

$$-EA\frac{3}{2}\frac{\partial^2 w_0}{\partial x^2}\left(\frac{\partial w_0}{\partial x}\right)^2 + EI\frac{\partial^4 w_0}{\partial x^4} + \rho A\ddot{w}_0 = p. \tag{A.7}$$

From all of the above and in particular equation (A.6), it is clear that neglecting membrane stresses, and hydrostatic pressure the first equation vanishes and that the second equation simplifies to the ordinary differential equation

$$EI\frac{\partial^4 w_0}{\partial x^4} + \rho A\ddot{w}_0 = p \tag{A.8}$$

Which is known from many elementary textbooks (Hibbeler [150] amongst others) as the Euler-Bernoulli beam equation.

A.2.1 Weak forms

To derive the finite element method for the Euler-Bernoulli beam, the weak form resulting from the governing equations in equations (A.6) to (A.8) should be derived. When deriving the governing equations using the virtual work principle, one could also use the integral form of the energy balance as weak form, while incorporating the boundary conditions using partial integration. Especially when the governing equation cannot be found easily using Hamilton's principle, this method is favourable. In case of the present equations, the weak form will however be derived based on the PDEs.

Firstly, starting at the most simple PDE, namely equation (A.8), the weak form is obtained by multiplication of the equation with a test function φ for the vertical deflection of the mid-plane w_0 and application of partial integration twice on the remaining terms, the following is obtained:

$$\begin{cases} \text{Find } w_0 \in \Sigma(\Omega) = H^2(\Omega),\ \Omega = (x_1, x_2) \in \mathbb{R}^1 \text{ s.t.} \\ \\ \displaystyle\int_{x_1}^{x_2} -\varphi\rho A\ddot{w}_0 + EI\frac{\mathrm{d}^2\varphi}{\mathrm{d}x^2}\frac{\mathrm{d}^2 w_0}{\mathrm{d}x^2}\,\mathrm{d}x + \left[EI\varphi\frac{\mathrm{d}^3 w_0}{\mathrm{d}x^3} - EI\frac{\mathrm{d}\varphi}{\mathrm{d}x}\frac{\mathrm{d}^2 w_0}{\mathrm{d}x^2}\right]_{x_1}^{x_2} = \int_{x_1}^{x_2}\varphi p\,\mathrm{d}x \\ \\ \forall\varphi \in \Sigma(\Omega) \end{cases} \tag{A.9}$$

Secondly, equation (A.7) contains the extra non-linear term proportional to $\frac{\partial^2 w_0}{\partial x^2}\left(\frac{\partial w_0}{\partial x}\right)^2$ due to membrane stiffening which cannot fully be partially integrated. However, the requirement on the derivatives of w_0 in this term can be reduced to first order. Note that this is a formality in principle, since the bending contributions still requires second order derivatives. The process is as follows:

$$\begin{aligned} \int_{x_1}^{x_2} -\varphi\frac{3}{2}EA\frac{\mathrm{d}^2 w_0}{\mathrm{d}x^2}\left(\frac{\mathrm{d}w_0}{\mathrm{d}x}\right)^2\,\mathrm{d}x &= \int_{x_1}^{x_2} -\frac{1}{2}EA\left[\frac{\mathrm{d}}{\mathrm{d}x}\left(\varphi\left(\frac{\mathrm{d}w_0}{\mathrm{d}x}\right)^3\right) - \frac{\mathrm{d}\varphi}{\mathrm{d}x}\left(\frac{\mathrm{d}w_0}{\mathrm{d}x}\right)^3\right]\mathrm{d}x \\ &= \int_{x_1}^{x_2}\frac{1}{2}EA\frac{\mathrm{d}\varphi}{\mathrm{d}x}\left(\frac{\mathrm{d}w_0}{\mathrm{d}x}\right)^3\mathrm{d}x - \left[\frac{1}{2}EA\varphi\left(\frac{\mathrm{d}w_0}{\mathrm{d}x}\right)^3\right]_{x_1}^{x_2}, \end{aligned}$$

Which results in the following weak form for equation (A.7):

$$\begin{cases} \text{Find } w_0 \in \Sigma(\Omega) = H^2(\Omega),\ \Omega = (x_1, x_2) \in \mathbb{R}^1 \text{ s.t.} \\ \\ \displaystyle\int_{x_1}^{x_2} -\varphi\rho A\ddot{w}_0 + \frac{1}{2}EA\frac{\mathrm{d}\varphi}{\mathrm{d}x}\left(\frac{\mathrm{d}w_0}{\mathrm{d}x}\right)^3 + EI\frac{\mathrm{d}^2\varphi}{\mathrm{d}x^2}\frac{\mathrm{d}^2 w_0}{\mathrm{d}x^2}\,\mathrm{d}x + \\ \displaystyle\quad + \left[EI\varphi\frac{\mathrm{d}^3 w_0}{\mathrm{d}x^3} - EI\frac{\mathrm{d}\varphi}{\mathrm{d}x}\frac{\mathrm{d}^2 w_0}{\mathrm{d}x^2} - \frac{1}{2}EA\varphi\left(\frac{\mathrm{d}w_0}{\mathrm{d}x}\right)^3\right]_{x_1}^{x_2} = \int_{x_1}^{x_2}\varphi p\,\mathrm{d}x \\ \\ \forall\varphi \in \Sigma(\Omega) \end{cases} \tag{A.10}$$

Lastly, the full set of equations from equation (A.6) requires two basis functions in the weak formulation, because there are two governing equations. For the first equation, which represents horizontal equilibrium, the test function ψ is used and for the second equation the test function φ is still used. For the first equation, multiplication with ψ, integrating over $\Omega = (x_1, x_2)$ and application of partial

integration gives:

$$\begin{aligned}\int_{x_1}^{x_2} -\psi EA\frac{\mathrm{d}}{\mathrm{d}x}\left(\frac{\mathrm{d}u_0}{\mathrm{d}x}+\frac{1}{2}\left(\frac{\mathrm{d}w_0}{\mathrm{d}x}\right)^2\right)\,\mathrm{d}x &= \int_{x_1}^{x_2} -EA\frac{\mathrm{d}}{\mathrm{d}x}\left[\psi\left(\frac{\mathrm{d}u_0}{\mathrm{d}x}+\frac{1}{2}\left(\frac{\mathrm{d}w_0}{\mathrm{d}x}\right)^2\right)\right]+\\ &\quad + EA\frac{\mathrm{d}\psi}{\mathrm{d}x}\left(\frac{\mathrm{d}u_0}{\mathrm{d}x}+\frac{1}{2}\left(\frac{\mathrm{d}w_0}{\mathrm{d}x}\right)^2\right)\,\mathrm{d}x\\ &= -\left[EA\psi\left(\frac{\mathrm{d}u_0}{\mathrm{d}x}+\frac{1}{2}\left(\frac{\mathrm{d}w_0}{\mathrm{d}x}\right)^2\right)\right]_{x_1}^{x_2}+\\ &\quad + \int_{x_1}^{x_2} EA\frac{\mathrm{d}\psi}{\mathrm{d}x}\left(\frac{\mathrm{d}u_0}{\mathrm{d}x}+\frac{1}{2}\left(\frac{\mathrm{d}w_0}{\mathrm{d}x}\right)^2\right)\,\mathrm{d}x\\ &= \int_{x_1}^{x_2} \psi\rho A\ddot{u}_0+\psi t\,\mathrm{d}x\end{aligned}$$

Furthermore, the extra term in the second equation is due to the membrane stretching due to the horizontal displacement. Multiplication with the test function φ and using partial integration for this term gives:

$$\begin{aligned}-\int_{x_1}^{x_2} EA\varphi\frac{\mathrm{d}}{\mathrm{d}x}\left[\frac{\mathrm{d}w_0}{\mathrm{d}x}\left(\frac{\mathrm{d}u_0}{\mathrm{d}x}+\frac{1}{2}\left(\frac{\mathrm{d}w_0}{\mathrm{d}x}\right)^2\right)\right]\,\mathrm{d}x &= \int_{x_1}^{x_2} EA\left\{-\frac{\mathrm{d}}{\mathrm{d}x}\left[\varphi\frac{\mathrm{d}w_0}{\mathrm{d}x}\left(\frac{\mathrm{d}u_0}{\mathrm{d}x}+\frac{1}{2}\left(\frac{\mathrm{d}w_0}{\mathrm{d}x}\right)^2\right)\right]+\right.\\ &\quad \left.+\frac{\mathrm{d}\varphi}{\mathrm{d}x}\left[\frac{\mathrm{d}w_0}{\mathrm{d}x}\left(\frac{\mathrm{d}u_0}{\mathrm{d}x}+\frac{1}{2}\left(\frac{\mathrm{d}w_0}{\mathrm{d}x}\right)^2\right)\right]\right\}\,\mathrm{d}x\\ &= -EA\left[\varphi\frac{\mathrm{d}w_0}{\mathrm{d}x}\left(\frac{\mathrm{d}u_0}{\mathrm{d}x}+\frac{1}{2}\left(\frac{\mathrm{d}w_0}{\mathrm{d}x}\right)^2\right)\right]_{x_1}^{x_2}+\\ &\quad + \int_{x_1}^{x_2} EA\frac{\mathrm{d}\varphi}{\mathrm{d}x}\left[\frac{\mathrm{d}w_0}{\mathrm{d}x}\left(\frac{\mathrm{d}u_0}{\mathrm{d}x}+\frac{1}{2}\left(\frac{\mathrm{d}w_0}{\mathrm{d}x}\right)^2\right)\right]\,\mathrm{d}x\end{aligned}$$

Thus, the final weak form for the PDEs in equation (A.6) become:

$$\begin{cases}\text{Find } u_0\in H^1(\Omega),\ w_0\in H^2(\Omega),\ \Omega=(x_1,x_2)\in\mathbb{R}^1 \text{ s.t.}\\[2ex]
\displaystyle\int_{x_1}^{x_2} EA\frac{\mathrm{d}\psi}{\mathrm{d}x}\left(\frac{\mathrm{d}u_0}{\mathrm{d}x}+\frac{1}{2}\left(\frac{\mathrm{d}w_0}{\mathrm{d}x}\right)^2\right)+\psi\rho A\ddot{u}_0\,\mathrm{d}x - EA\left[\psi\left(\frac{\mathrm{d}u_0}{\mathrm{d}x}+\frac{1}{2}\left(\frac{\mathrm{d}w_0}{\mathrm{d}x}\right)^2\right)\right]_{x_1}^{x_2} = \int_{x_1}^{x_2}\psi t\,\mathrm{d}x\\[2ex]
\displaystyle\int_{x_1}^{x_2}\varphi\rho A\ddot{w}_0+EA\frac{\mathrm{d}\varphi}{\mathrm{d}x}\left[\frac{\mathrm{d}w_0}{\mathrm{d}x}\left(\frac{\mathrm{d}u_0}{\mathrm{d}x}+\frac{1}{2}\left(\frac{\mathrm{d}w_0}{\mathrm{d}x}\right)^2\right)\right]+EI\frac{\mathrm{d}^2\varphi}{\mathrm{d}x^2}\frac{\mathrm{d}^2w_0}{\mathrm{d}x^2}\,\mathrm{d}x+\\
\quad\displaystyle+\left[-EA\left\{\varphi\frac{\mathrm{d}w_0}{\mathrm{d}x}\left(\frac{\mathrm{d}u_0}{\mathrm{d}x}+\frac{1}{2}\left(\frac{\mathrm{d}w_0}{\mathrm{d}x}\right)^2\right)\right\}+EI\left\{\varphi\frac{\mathrm{d}^3w_0}{\mathrm{d}x^3}-\frac{\mathrm{d}\varphi}{\mathrm{d}x}\frac{\mathrm{d}^2w_0}{\mathrm{d}x^2}\right\}\right]_{x_1}^{x_2} = \int_{x_1}^{x_2}\varphi p\,\mathrm{d}x\\[2ex]
\forall\varphi\in\Sigma(\Omega)\end{cases}\tag{A.11}$$

Lastly, the right hand side of the weak form is determined by a given traction $f(x)$ and a given *vertical* pressure $p(x)$. However, if there is a pressure acting on the beam, this always acts in normal direction. Hence, a pressure acting on the beam is:

$$p\boldsymbol{n} = p\begin{bmatrix}n_x\\ n_y\end{bmatrix},$$

Where $\boldsymbol{n}$ is the normal vector of the beam with components n_x and n_y. Obviously, the normal vector of the beam is not known until the solution of the system is known. However, we know that the (unit) normal vector along an arbitrary curve is given by:

$$\boldsymbol{n} = \frac{1}{\sqrt{\left(1+\frac{\mathrm{d}u_0}{\mathrm{d}x}\right)^2+\left(\frac{\mathrm{d}w_0}{\mathrm{d}x}\right)^2}}\begin{bmatrix}-\frac{\mathrm{d}w_0}{\mathrm{d}x}\\ 1+\frac{\mathrm{d}u_0}{\mathrm{d}x}\end{bmatrix}, \tag{A.12}$$

And hence the right hand side forcing vectors in case of a following pressure $p(x)$ become:

$$\int_{x_1}^{x_2}\psi t\,\mathrm{d}x \longrightarrow -\int_{x_1}^{x_2} p(x)\psi\frac{\frac{\mathrm{d}w_0}{\mathrm{d}x}}{\sqrt{\left(1+\frac{\mathrm{d}u_0}{\mathrm{d}x}\right)^2+\left(\frac{\mathrm{d}w_0}{\mathrm{d}x}\right)^2}}\,\mathrm{d}x,$$
$$\int_{x_1}^{x_2}\varphi p\,\mathrm{d}x \longrightarrow \int_{x_1}^{x_2} p(x)\psi\frac{1+\frac{\mathrm{d}u_0}{\mathrm{d}x}}{\sqrt{\left(1+\frac{\mathrm{d}u_0}{\mathrm{d}x}\right)^2+\left(\frac{\mathrm{d}w_0}{\mathrm{d}x}\right)^2}}\,\mathrm{d}x.$$

A.3 Beam with Initial Deformation

The governing equations for a non-linear beam with initial deflections $w^*(x)$ are [31]

$$\begin{aligned} -EA\left[\frac{\mathrm{d}}{\mathrm{d}x}\left(\frac{\mathrm{d}u}{\mathrm{d}x}\right)+\frac{1}{2}\left(\frac{\mathrm{d}w}{\mathrm{d}x}\right)^2+\frac{\mathrm{d}w^*}{\mathrm{d}x}\frac{\mathrm{d}w}{\mathrm{d}x}\right]+\rho A\ddot{u} &= t\\ -EA\frac{\mathrm{d}}{\mathrm{d}x}\left[\left(\frac{\mathrm{d}u}{\mathrm{d}x}+\frac{1}{2}\left(\frac{\mathrm{d}w}{\mathrm{d}x}\right)^2+\frac{\mathrm{d}w^*}{\mathrm{d}x}\frac{\mathrm{d}w}{\mathrm{d}x}\right)\frac{\mathrm{d}w+w^*}{\mathrm{d}x}\right]+EI\frac{\mathrm{d}^4w}{\mathrm{d}x^4}+\rho A\ddot{w} &= p \end{aligned} \tag{A.13}$$

The weak form of this equation is obtained by multiplying the first equation with test fuction $\psi(x)$ and the second with $\varphi(x)$ and integrating them over the domain Ω. The derivation is similar to the one given in section A.2.1. However, some additional terms, which are $\boxed{\text{boxed}}$ in the following equations are present due to extra terms with w^*. Similar to equation (A.11), the weak form becomes:

$$\begin{cases}
\text{Find } u_0\in H^1(\Omega),\ w_0\in H^2(\Omega),\ \Omega=(x_1,x_2)\in\mathbb{R}^1 \text{ s.t.}\\[2ex]
\displaystyle\int_{x_1}^{x_2} EA\frac{\mathrm{d}\psi}{\mathrm{d}x}\left(\frac{\mathrm{d}u_0}{\mathrm{d}x}+\frac{1}{2}\left(\frac{\mathrm{d}w_0}{\mathrm{d}x}\right)^2+\boxed{\frac{\mathrm{d}w}{\mathrm{d}x}\frac{\mathrm{d}w^*}{\mathrm{d}x}}\right)+\psi\rho A\ddot{u}_0\,\mathrm{d}x+\\
\displaystyle -EA\left[\psi\left(\frac{\mathrm{d}u_0}{\mathrm{d}x}+\frac{1}{2}\left(\frac{\mathrm{d}w_0}{\mathrm{d}x}\right)^2\right)+\boxed{\frac{\mathrm{d}w}{\mathrm{d}x}\frac{\mathrm{d}w^*}{\mathrm{d}x}}\right]_{x_1}^{x_2}=\int_{x_1}^{x_2}\psi t\,\mathrm{d}x\\
\displaystyle\int_{x_1}^{x_2}\varphi\rho A\ddot{w}_0+EA\frac{\mathrm{d}\varphi}{\mathrm{d}x}\left[\frac{\mathrm{d}w_0}{\mathrm{d}x}\left(\frac{\mathrm{d}u_0}{\mathrm{d}x}+\frac{1}{2}\left(\frac{\mathrm{d}w_0}{\mathrm{d}x}\right)^2+\boxed{\frac{\mathrm{d}w}{\mathrm{d}x}\frac{\mathrm{d}w^*}{\mathrm{d}x}}\right)+\boxed{\frac{\mathrm{d}w^*}{\mathrm{d}x}\left(\frac{\mathrm{d}u_0}{\mathrm{d}x}+\frac{1}{2}\left(\frac{\mathrm{d}w_0}{\mathrm{d}x}\right)^2+\frac{\mathrm{d}w}{\mathrm{d}x}\frac{\mathrm{d}w^*}{\mathrm{d}x}\right)}\right]+\\
\displaystyle+EI\frac{\mathrm{d}^2\varphi}{\mathrm{d}x^2}\frac{\mathrm{d}^2w_0}{\mathrm{d}x^2}\,\mathrm{d}x+\left[-EA\left\{\varphi\frac{\mathrm{d}w_0}{\mathrm{d}x}\left(\frac{\mathrm{d}u_0}{\mathrm{d}x}+\frac{1}{2}\left(\frac{\mathrm{d}w_0}{\mathrm{d}x}\right)^2+\boxed{\frac{\mathrm{d}w}{\mathrm{d}x}\frac{\mathrm{d}w^*}{\mathrm{d}x}}\right)+\right.\right.\\
\displaystyle\left.\left.+\boxed{\varphi\frac{\mathrm{d}w^*}{\mathrm{d}x}\left(\frac{\mathrm{d}u_0}{\mathrm{d}x}+\frac{1}{2}\left(\frac{\mathrm{d}w_0}{\mathrm{d}x}\right)^2+\frac{\mathrm{d}w}{\mathrm{d}x}\frac{\mathrm{d}w^*}{\mathrm{d}x}\right)}\right\}+EI\left\{\varphi\frac{\mathrm{d}^3w_0}{\mathrm{d}x^3}-\frac{\mathrm{d}\varphi}{\mathrm{d}x}\frac{\mathrm{d}^2w_0}{\mathrm{d}x^2}\right\}\right]_{x_1}^{x_2}=\int_{x_1}^{x_2}\varphi p\,\mathrm{d}x\\[2ex]
\forall\varphi\in\Sigma(\Omega)
\end{cases} \tag{A.14}$$

A.4 Jacobian of the Stiffness Matrix

The Jacobian of the stiffness matrix of the non-linear beam equation can be obtained using [104]

$$\mathrm{J}_G = \frac{\partial \boldsymbol{R}}{\partial \boldsymbol{\alpha}}.$$

Where $\boldsymbol{R} = \mathrm{D}(\boldsymbol{\alpha})\boldsymbol{\alpha} - \boldsymbol{F}$. Matrix D in this case is the sum of both stiffness matrices in equation (5.12) and $\boldsymbol{F}$ is the right-hand-side vector. Recall the total stiffness matrix of the non-linear beam:

$$\mathrm{D}(\boldsymbol{\alpha}) = \begin{bmatrix} \mathrm{K}_A & \mathrm{S}_{AB}(\boldsymbol{\alpha}) \\ \mathrm{S}_{BA}(\boldsymbol{\alpha}) & \mathrm{K}_B + \mathrm{S}_B(\boldsymbol{\alpha}) \end{bmatrix}$$

Where (using inner-product notation),

$$\begin{aligned}
\mathrm{K}_{A,ij} &= \int_0^1 EA \frac{\mathrm{d}\psi_i}{\mathrm{d}x} \frac{\mathrm{d}\psi_j}{\mathrm{d}x}\, \mathrm{d}x, \\
\mathrm{K}_{B,ij} &= \int_0^1 EI \frac{\mathrm{d}^2\varphi_i}{\mathrm{d}x^2} \frac{\mathrm{d}^2\varphi_j}{\mathrm{d}x^2}\, \mathrm{d}x, \\
\mathrm{S}_{AB,ij}(\boldsymbol{\alpha}) &= \int_0^1 \frac{EA}{2} \frac{\mathrm{d}\psi_i}{\mathrm{d}x} \frac{\mathrm{d}\varphi_j}{\mathrm{d}x} \left(\boldsymbol{c} \frac{\mathrm{d}\boldsymbol{\varphi}}{\mathrm{d}x} \right) \mathrm{d}x, \\
\mathrm{S}_{BA,ij}(\boldsymbol{\alpha}) &= \int_0^1 EA \frac{\mathrm{d}\varphi_i}{\mathrm{d}x} \frac{\mathrm{d}\psi_j}{\mathrm{d}x} \left(\boldsymbol{c} \frac{\mathrm{d}\boldsymbol{\varphi}}{\mathrm{d}x} \right) \mathrm{d}x, \\
\mathrm{S}_{B,ij}(\boldsymbol{\alpha}) &= \int_{x_1}^{x_2} \frac{EA}{2} \frac{\mathrm{d}\varphi_i}{\mathrm{d}x} \frac{\mathrm{d}\varphi_j}{\mathrm{d}x} \left(\boldsymbol{c} \frac{\mathrm{d}\boldsymbol{\varphi}}{\mathrm{d}x} \right)^2 \mathrm{d}x,
\end{aligned}$$

The corresponding Jacobian matrix is defined as:

$$\mathrm{J}_G = \begin{bmatrix} \mathrm{J}_A & \mathrm{J}_{AB} \\ \mathrm{J}_{BA} & \mathrm{J}_B \end{bmatrix}$$

With (see [104]),

$$\begin{aligned}
\mathrm{J}_{A,ij} &= D_{A,ij} + \frac{\partial D_{A,ij}}{\partial \boldsymbol{a}} \cdot a + \frac{\partial D_{AB,ij}}{\partial \boldsymbol{a}} \cdot \boldsymbol{c} - \frac{\partial F_i}{\partial a_j} \\
&= D_{A,ij} + 0 + 0
\end{aligned}$$

$$\begin{aligned}
\mathrm{J}_{AB,ij} &= D_{AB,ij} + \frac{\partial D_{A,ij}}{\partial \boldsymbol{c}} \cdot \boldsymbol{a} + \frac{\partial D_{AB,ij}}{\partial \boldsymbol{c}} \cdot \boldsymbol{c} - \frac{\partial \boldsymbol{F}}{\partial \boldsymbol{c}} \\
&= D_{AB,ij} + 0 + \frac{\partial}{\partial \boldsymbol{c}} \left(\int_0^1 \frac{EA}{2} \frac{\mathrm{d}\psi_i}{\mathrm{d}x} \frac{\mathrm{d}\varphi_j}{\mathrm{d}x} \left(\boldsymbol{c} \frac{\mathrm{d}\boldsymbol{\varphi}}{\mathrm{d}x} \right) \mathrm{d}x \right) \cdot \boldsymbol{c} - 0 \\
&= D_{AB,ij} + \left(\int_0^1 \frac{EA}{2} \frac{\mathrm{d}\psi_i}{\mathrm{d}x} \frac{\mathrm{d}\varphi_j}{\mathrm{d}x} \frac{\partial}{\partial \boldsymbol{c}} \left(\boldsymbol{c} \frac{\mathrm{d}\boldsymbol{\varphi}}{\mathrm{d}x} \right) \mathrm{d}x \right) \cdot \boldsymbol{c} \\
&= D_{AB,ij} + \left(\int_0^1 \frac{EA}{2} \frac{\mathrm{d}\psi_i}{\mathrm{d}x} \frac{\mathrm{d}\varphi_j}{\mathrm{d}x} \frac{\mathrm{d}\boldsymbol{\varphi}}{\mathrm{d}x} \mathrm{d}x \right) \cdot \boldsymbol{c} \\
&= D_{AB,ij} + \int_0^1 \frac{EA}{2} \frac{\mathrm{d}\psi_i}{\mathrm{d}x} \frac{\mathrm{d}\varphi_j}{\mathrm{d}x} \frac{\mathrm{d}\boldsymbol{\varphi}}{\mathrm{d}x} \cdot \boldsymbol{c}\, \mathrm{d}x \\
&= D_{AB,ij} + D_{AB,ij} = 2D_{AB,ij}
\end{aligned}$$

$$\begin{aligned}
\mathrm{J}_{BA,ij} &= D_{BA,ij} + \frac{\partial D_{BA,ij}}{\partial \boldsymbol{a}} \cdot \boldsymbol{a} + \frac{\partial D_{B,ij}}{\partial \boldsymbol{a}} \cdot \boldsymbol{c} - \frac{\partial \boldsymbol{F}}{\partial \boldsymbol{a}} \\
&= D_{BA,ij} + 0 + 0 - 0
\end{aligned}$$

$$
\begin{aligned}
\mathrm{J}_{B,ij} &= D_{B,ij} + \frac{\partial D_{BA,ij}}{\partial \boldsymbol{c}} \cdot \boldsymbol{a} + \frac{\partial D_{B,ij}}{\partial \boldsymbol{c}} \cdot \boldsymbol{c} - \frac{\partial \boldsymbol{F}}{\partial \boldsymbol{c}} \\
&= D_{B,ij} + \frac{\partial}{\partial \boldsymbol{c}} \left(\int_0^1 EA \frac{\mathrm{d}\varphi_i}{\mathrm{d}x} \frac{\mathrm{d}\psi_j}{\mathrm{d}x} \left(\boldsymbol{c} \frac{\mathrm{d}\boldsymbol{\varphi}}{\mathrm{d}x} \right) \mathrm{d}x \right) \cdot \boldsymbol{a} + \frac{\partial}{\partial \boldsymbol{c}} \left(\int_{x_1}^{x_2} \frac{EA}{2} \frac{\mathrm{d}\varphi_i}{\mathrm{d}x} \frac{\mathrm{d}\varphi_j}{\mathrm{d}x} \left(\boldsymbol{c} \frac{\mathrm{d}\boldsymbol{\varphi}}{\mathrm{d}x} \right)^2 \mathrm{d}x \right) \cdot \boldsymbol{c} - 0 \\
&= D_{B,ij} + \left(\int_0^1 EA \frac{\mathrm{d}\varphi_i}{\mathrm{d}x} \frac{\mathrm{d}\psi_j}{\mathrm{d}x} \frac{\partial}{\partial \boldsymbol{c}} \left(\boldsymbol{c} \frac{\mathrm{d}\boldsymbol{\varphi}}{\mathrm{d}x} \right) \mathrm{d}x \right) \cdot \boldsymbol{a} + \left(\int_{x_1}^{x_2} \frac{EA}{2} \frac{\mathrm{d}\varphi_i}{\mathrm{d}x} \frac{\mathrm{d}\varphi_j}{\mathrm{d}x} \frac{\partial}{\partial \boldsymbol{c}} \left(\boldsymbol{c} \frac{\mathrm{d}\boldsymbol{\varphi}}{\mathrm{d}x} \right)^2 \mathrm{d}x \right) \cdot \boldsymbol{c} \\
&= D_{B,ij} + \left(\int_0^1 EA \frac{\mathrm{d}\varphi_i}{\mathrm{d}x} \frac{\mathrm{d}\psi_j}{\mathrm{d}x} \frac{\mathrm{d}\boldsymbol{\varphi}}{\mathrm{d}x} \mathrm{d}x \right) \cdot \boldsymbol{a} + 2 \left(\int_{x_1}^{x_2} \frac{EA}{2} \frac{\mathrm{d}\varphi_i}{\mathrm{d}x} \frac{\mathrm{d}\varphi_j}{\mathrm{d}x} \left(\boldsymbol{c} \frac{\mathrm{d}\boldsymbol{\varphi}}{\mathrm{d}x} \right) \frac{\mathrm{d}\boldsymbol{\varphi}}{\mathrm{d}x} \mathrm{d}x \right) \cdot \boldsymbol{c} \\
&= D_{B,ij} + \left(\int_0^1 EA \frac{\mathrm{d}\varphi_i}{\mathrm{d}x} \frac{\mathrm{d}\boldsymbol{\psi}}{\mathrm{d}x} \frac{\mathrm{d}\varphi_j}{\mathrm{d}x} \mathrm{d}x \right) \cdot \boldsymbol{a} + 2 \int_{x_1}^{x_2} \frac{EA}{2} \frac{\mathrm{d}\varphi_i}{\mathrm{d}x} \frac{\mathrm{d}\varphi_j}{\mathrm{d}x} \left(\boldsymbol{c} \frac{\mathrm{d}\boldsymbol{\varphi}}{\mathrm{d}x} \right) \frac{\mathrm{d}\boldsymbol{\varphi}}{\mathrm{d}x} \cdot \boldsymbol{c} \, \mathrm{d}x \\
&= D_{B,ij} + \left(\int_0^1 EA \frac{\mathrm{d}\varphi_i}{\mathrm{d}x} \left(\frac{\mathrm{d}\boldsymbol{\psi}}{\mathrm{d}x} \cdot \boldsymbol{a} \right) \frac{\mathrm{d}\varphi_j}{\mathrm{d}x} \mathrm{d}x \right) + 2 \int_{x_1}^{x_2} \frac{EA}{2} \frac{\mathrm{d}\varphi_i}{\mathrm{d}x} \frac{\mathrm{d}\varphi_j}{\mathrm{d}x} \left(\boldsymbol{c} \frac{\mathrm{d}\boldsymbol{\varphi}}{\mathrm{d}x} \right)^2 \mathrm{d}x
\end{aligned}
$$

Additionally, the optionally extra terms from the contribution of the initial deformation of the beam should also be incorporated in the Jacobian matrix. Recall that the stiffness matrices due to initial deformation of the beam are (using inner-product notation instead of sum notation for the non-linear term):

$$
\begin{aligned}
\mathrm{D}^*_{AB,ij} &= \int_0^1 EA \frac{\mathrm{d}\psi_i}{\mathrm{d}x} \frac{\mathrm{d}\varphi_j}{\mathrm{d}x} \frac{\mathrm{d}w^*}{\mathrm{d}x} \mathrm{d}x, \\
\mathrm{D}^*_{BA,ij} &= \int_0^1 EA \frac{\mathrm{d}\varphi_i}{\mathrm{d}x} \frac{\mathrm{d}\psi_j}{\mathrm{d}x} \frac{\mathrm{d}w^*}{\mathrm{d}x} \mathrm{d}x, \\
\mathrm{D}^*_{B,ij} &= \int_0^1 EA \frac{\mathrm{d}\varphi_i}{\mathrm{d}x} \frac{\mathrm{d}\varphi_j}{\mathrm{d}x} \left(\frac{\mathrm{d}w^*}{\mathrm{d}x} \right)^2 \mathrm{d}x + \int_0^1 \frac{3}{2} EA \frac{\mathrm{d}\varphi_i}{\mathrm{d}x} \frac{\mathrm{d}\varphi_j}{\mathrm{d}x} \frac{\mathrm{d}w^*}{\mathrm{d}x} \left(\boldsymbol{c} \cdot \frac{\mathrm{d}\boldsymbol{\varphi}}{\mathrm{d}x} \right) \mathrm{d}x.
\end{aligned}
$$

The only term that contributes to the Jacobian matrix is the derivative of $\mathrm{D}^*_{B,ij}$ with respect to $\boldsymbol{c}$. Hence, the additional terms for the Jacobian matrix due to the initial deformations are:

$$
\begin{aligned}
\mathrm{J}^*_{A,ij} &= \mathrm{D}^*_{A,ij} \\
\mathrm{J}^*_{AB,ij} &= \mathrm{D}^*_{AB,ij} \\
\mathrm{J}^*_{BA,ij} &= \mathrm{D}^*_{BA,ij}
\end{aligned}
$$

$$
\begin{aligned}
\mathrm{J}^*_{B,ij} &= \mathrm{D}^*_{B,ij} + \frac{\partial D^*_{BA,ij}}{\partial \boldsymbol{c}} \cdot \boldsymbol{a} + \frac{\partial D^*_{B,ij}}{\partial \boldsymbol{c}} \cdot \boldsymbol{c} - \frac{\partial \boldsymbol{F}}{\partial \boldsymbol{c}} \\
&= \mathrm{D}^*_{B,ij} + 0 + \frac{\partial}{\partial \boldsymbol{c}} \left(\int_0^1 \frac{3}{2} EA \frac{\mathrm{d}\varphi_i}{\mathrm{d}x} \frac{\mathrm{d}\varphi_j}{\mathrm{d}x} \frac{\mathrm{d}w^*}{\mathrm{d}x} \left(\boldsymbol{c} \cdot \frac{\mathrm{d}\boldsymbol{\varphi}}{\mathrm{d}x} \right) \mathrm{d}x \right) \cdot \boldsymbol{c} - 0 \\
&= \mathrm{D}^*_{B,ij} + \left(\int_0^1 \frac{3}{2} EA \frac{\mathrm{d}\varphi_i}{\mathrm{d}x} \frac{\mathrm{d}\varphi_j}{\mathrm{d}x} \frac{\mathrm{d}w^*}{\mathrm{d}x} \frac{\partial}{\partial \boldsymbol{c}} \left(\boldsymbol{c} \cdot \frac{\mathrm{d}\boldsymbol{\varphi}}{\mathrm{d}x} \right) \mathrm{d}x \right) \cdot \boldsymbol{c} \\
&= \mathrm{D}^*_{B,ij} + \left(\int_0^1 \frac{3}{2} EA \frac{\mathrm{d}\varphi_i}{\mathrm{d}x} \frac{\mathrm{d}\varphi_j}{\mathrm{d}x} \frac{\mathrm{d}w^*}{\mathrm{d}x} \frac{\mathrm{d}\boldsymbol{\varphi}}{\mathrm{d}x} \mathrm{d}x \right) \cdot \boldsymbol{c} \\
&= \mathrm{D}^*_{B,ij} + \left(\int_0^1 \frac{3}{2} EA \frac{\mathrm{d}\varphi_i}{\mathrm{d}x} \frac{\mathrm{d}\varphi_j}{\mathrm{d}x} \frac{\mathrm{d}w^*}{\mathrm{d}x} \left(\frac{\mathrm{d}\boldsymbol{\varphi}}{\mathrm{d}x} \cdot \boldsymbol{c} \right) \mathrm{d}x \right)
\end{aligned}
$$

B | Some notes on Differential Geometry

This section gives a brief overview of the prerequisites of Differential Geometry for Isogeometric Analysis. This is based on the work of Ivancevic and Ivancevic[154], which are recommended for further reading on the topic. In the sequel, it is assumed that a curve $\mathcal{C}$, a surface $\mathcal{S}$ and a volume $\mathcal{V}$ are represented by NURBS or B-splines:

$$\begin{aligned}
\mathcal{C}(\xi) &= \sum_{i=1}^{n} N_i(\xi)\mathrm{B}_i, \\
\mathcal{S}(\xi) &= \sum_{i=1}^{n}\sum_{j=1}^{n} N_i(\xi)N_j(\eta)\mathrm{B}_{i,j}, \\
\mathcal{V}(\xi) &= \sum_{i=1}^{n}\sum_{j=1}^{n}\sum_{k=1}^{n} N_i(\xi)N_j(\eta)N_k(\zeta)\mathrm{B}_{i,j,k},
\end{aligned}$$

Where matrix B_i contains the coordinates (in a 1D, 2D or 3D space) of control point i, $B_{i,j}$ for control point i, j and so on.

Firstly, the process in IGA relies on a mapping from the physical domain to a parent domain. Let $\Omega \subset \mathbb{R}^p$ be the physical domain, $\hat{\Omega} \subset \mathbb{R}^q$ and let $\boldsymbol{s} : \Omega \to \hat{\Omega}$ be a mapping from the physical domain to the parent domain. The inverse mapping is then denoted by $\boldsymbol{s}^{-1} : \hat{\Omega} \to \Omega$. Furthermore, a point denoted by captials (e.g. X) is a p-dimensional point in the physical domain (e.g. $X \in \Omega \subset \mathbb{R}^p$) and a point denoted by a lower case letter (e.g. x) is a q-dimensional point in the parent domain ($x \in \hat{\Omega} \subset \mathbb{R}^q$). There are no restrictions on the dimension p and q.

Let now $f : \Omega \to \mathbb{R}$ be a function from the physical domain to $\mathbb{R}$ (w.l.o.g. 1D) which is evaluated on point X. Then the function can be evaluated from the parameter domain by the composite function $g = f \circ \boldsymbol{s} : \hat{\Omega} \to \mathbb{R}$ from the point x, since $X = \boldsymbol{s}(x)$. Here the $f \circ \boldsymbol{s} = f(\boldsymbol{s})$ Furthermore, the Jacobian matrix of the mapping is defined as:

$$\mathrm{J} = \frac{\partial \boldsymbol{s}}{\partial \boldsymbol{x}} = \frac{\partial s_i}{\partial x_j}$$

Furthermore, the fundamental (material) covariant metric tensor (in short metric tensor) $\underline{\underline{\boldsymbol{g}}}$ [154] is defined as:

$$\underline{\underline{\boldsymbol{g}}} = \mathrm{J}^T\mathrm{J} = \frac{\partial s_i}{\partial x_j}\frac{\partial s_i}{\partial x_k} \tag{B.1}$$

Which has inverse $\underline{\underline{\boldsymbol{g}}}^{-1}$. The determinant of J, which is used for changing integration domains, is denoted by:

$$\det(J) = |J| \tag{B.2}$$

However, if J is not square, which is possible when the dimensionality of the physical domain and the parent domain are not equal, it is not possible to calculate the determinant of J directly. In that case, the metric tensor is utilised:

$$\det(J) = \sqrt{\underline{\underline{\boldsymbol{g}}}} = \sqrt{\mathrm{J}^T\mathrm{J}} \tag{B.3}$$

When the dimensionality of the physical and parent domains are equal, this is equal to the determinant of J. Suppose again that we have the functions $f : \Omega \to \mathbb{R}$ and $g = f(\boldsymbol{s}) : \hat{\Omega} \to \mathbb{R}$. Then, from Calculus text books it is widely known that

$$\int_{\Omega} f(X)\,\mathrm{d}\Omega = \int_{\hat{\Omega}} f \circ \boldsymbol{s}(x) \det J\,\mathrm{d}\hat{\Omega} \tag{B.4}$$

Furthermore, as the basis of the spaces changes under the mapping, differential operators from the Euclidean space also change. For this study, the curvilinear equivalent for the gradient and the laplacian are relevant:

$$\begin{aligned} \nabla_X f &= \underline{\underline{\boldsymbol{g}}}^{-1}\nabla_x f \circ \boldsymbol{s} && \text{Curvilinear Operator,} \\ \nabla_X^2 f &= \frac{1}{\sqrt{\boldsymbol{g}}}\nabla_x\left(\sqrt{\boldsymbol{g}}\underline{\underline{\boldsymbol{g}}}^{-1}\nabla_x f \circ \boldsymbol{s}\right) && \text{Laplace-Beltrami Operator,} \end{aligned} \tag{B.5}$$

B.1 Numerical Implementation for B-splines

The differential theory as presented in the previous section needs to be implemented for B-splines in the IGA code in order to compute the deformations of initially curved beams. This section briefly elaborates on the calculation of the above quantities specifically for a curve $\mathcal{C}$ described by B-splines. Firstly, recall that this curve is defined by:

$$\mathcal{C}(\xi) = \sum_{i=1}^{n} N_i(\xi)\mathrm{B}_i \tag{B.6}$$

Hence, the curve is naturally a mapping of basis function of a parent domain $\hat{\Omega}$. Namely, the parametric domain can be indexed by the coordinate ξ and the basis function $N_i(\xi)$ can be used for analyses in this parametric domain, which is the idea behind IGA. Furthermore, the matrix B_i in fact transforms the basis function $N_i(\xi)$ to the physical space Ω. Summarizing, the mapping $\boldsymbol{s}$ for a B-spline is naturally equal to $\mathcal{C}(\xi)$, i.e. $\boldsymbol{s} = \mathcal{C} : \hat{\Omega} \to \Omega$. The only parameter that describes the curve is ξ. Hence, the dimensionality of the parametric domain is 1 and the dimensionality of the physical domain is arbitrary.

The Jacobian matrix J for a curve described by B-splines (or NURBS) consists of the derivatives of the elements of the curve with respect to the parameter ξ. Hence, for a curve in 3D:

$$\mathrm{J} = \begin{bmatrix} \frac{\partial \mathcal{C}_x}{\partial \xi} \\ \frac{\partial \mathcal{C}_y}{\partial \xi} \\ \frac{\partial \mathcal{C}_z}{\partial \xi} \end{bmatrix} = \begin{bmatrix} \sum_{i=1}^{n} \frac{\mathrm{d}N_i}{\mathrm{d}\xi}(\xi)\mathrm{B}_{x,i} \\ \sum_{i=1}^{n} \frac{\mathrm{d}N_i}{\mathrm{d}\xi}(\xi)\mathrm{B}_{y,i} \\ \sum_{i=1}^{n} \frac{\mathrm{d}N_i}{\mathrm{d}\xi}(\xi)\mathrm{B}_{y,i} \end{bmatrix}, \tag{B.7}$$

And hence the metric tensor (scalar in this case) becomes:

$$g = \mathrm{J}^T\mathrm{J} = \left(\sum_{i=1}^{n} \frac{\mathrm{d}N_i}{\mathrm{d}\xi}(\xi)\mathrm{B}_{x,i}\right)^2 + \left(\sum_{i=1}^{n} \frac{\mathrm{d}N_i}{\mathrm{d}\xi}(\xi)\mathrm{B}_{y,i}\right)^2 + \left(\sum_{i=1}^{n} \frac{\mathrm{d}N_i}{\mathrm{d}\xi}(\xi)\mathrm{B}_{z,i}\right)^2, \tag{B.8}$$

And its inverse is simply

$$g^{-1} = 1/g = \frac{1}{\left(\sum_{i=1}^{n} \frac{\mathrm{d}N_i}{\mathrm{d}\xi}(\xi)\mathrm{B}_{x,i}\right)^2 + \left(\sum_{i=1}^{n} \frac{\mathrm{d}N_i}{\mathrm{d}\xi}(\xi)\mathrm{B}_{y,i}\right)^2 + \left(\sum_{i=1}^{n} \frac{\mathrm{d}N_i}{\mathrm{d}\xi}(\xi)\mathrm{B}_{z,i}\right)^2}. \tag{B.9}$$

The differential operators over the curve $\mathcal{C}$ are calculated using the metric tensor and its inverse. Let $f : \mathcal{C} \to \mathbb{R}$ be a function defined on the curve. Then, the gradient in the Euclidean space becomes:

$$\nabla_X f = \frac{1}{g}\frac{\mathrm{d}}{\mathrm{d}\xi}(f \circ \boldsymbol{s}), \tag{B.10}$$

And the Laplace-Beltrami operator in Euclidean space can be simplified to:

$$\nabla_X^2 f = \frac{1}{\sqrt{g}}\frac{\mathrm{d}}{\mathrm{d}\xi}\left(\sqrt{g}\frac{1}{g}\frac{\mathrm{d}}{\mathrm{d}\xi}(f \circ \boldsymbol{s})\right), \tag{B.11}$$

$$= \frac{1}{\sqrt{g}}\left[\frac{1}{2g\sqrt{g}}\frac{\mathrm{d}g}{\mathrm{d}\xi}\frac{\mathrm{d}}{\mathrm{d}\xi}(f \circ \boldsymbol{s}) - \frac{\sqrt{g}}{g^2}\frac{\mathrm{d}g}{\mathrm{d}\xi}\frac{\mathrm{d}}{\mathrm{d}\xi}(f \circ \boldsymbol{s}) + \frac{1}{\sqrt{g}}\frac{\mathrm{d}^2}{\mathrm{d}\xi^2}(f \circ \boldsymbol{s})\right]. \tag{B.12}$$

Here, the last step is performed for implementation in a code and results from basic mathematical differentiation rules. Note that this requires additionally the derivative of g with respect to ξ. This is:

$$\frac{\mathrm{d}g}{\mathrm{d}\xi} = \mathrm{d}\mathrm{J}^T\mathrm{J} + \mathrm{J}^T\mathrm{d}\mathrm{J} \tag{B.13}$$

Where dJ is:

$$\mathrm{d}\mathrm{J} = \begin{bmatrix} \frac{\partial^2 \mathcal{C}_x}{\partial \xi^2} \\ \frac{\partial^2 \mathcal{C}_y}{\partial \xi^2} \\ \frac{\partial^2 \mathcal{C}_z}{\partial \xi^2} \end{bmatrix} = \begin{bmatrix} \sum_{i=1}^{n} \frac{\mathrm{d}^2 N_i}{\mathrm{d}\xi^2}(\xi)\mathrm{B}_{x,i} \\ \sum_{i=1}^{n} \frac{\mathrm{d}^2 N_i}{\mathrm{d}\xi^2}(\xi)\mathrm{B}_{y,i} \\ \sum_{i=1}^{n} \frac{\mathrm{d}^2 N_i}{\mathrm{d}\xi^2}(\xi)\mathrm{B}_{y,i} \end{bmatrix}, \tag{B.14}$$